Dissertation
submitted to the
Combined Faculties for the Natural Sciencies and for Mathematics
of the Ruperto-Carola University of Heidelberg, Germany
for the degree of
Doctor of Natural Sciencies

presented by
Lic. Física Antonio Javier González Martínez
born in Valencia

Oral examination: 29 June 2005

Quantum interference in the dielectronic recombination of heavy highly charged ions

Referees: Prof. Dr. Joachim Ullrich
Prof. Dr. Dirk Schwalm

Zusammenfassung:

Die Photorekombination hochgeladener Quecksilberionen wurde mittels einer Elektronenstrahlionenfalle (electron beam ion trap) experimentell untersucht. Ein Elektronenstrahl variabler Energie überstrich den Bereich $45 - 54$ keV, in dem die KLL Resonanzen der $Hg^{75+...78+}$-Ionen liegen. Zum Nachweis der Photorekombination diente die dabei erzeugte Strahlung. Dies ermöglichte es, die Anregungsenergien dieser Resonanzen zustandsselektiv mit Meßfehlern kleiner als $\pm$ 5 eV zu bestimmen. Diese Genauigkeit gestattete es zum ersten Mal, zwischen verschiedenen *ab initio* Berechnungen für eine Anzahl von Konfigurationen zu unterscheiden, wobei sich einige signifikante Abweichungen zeigten. QED-Beiträge und Kerngrößeneffekte von jeweils in etwa 160 eV und 50 eV mußten dabei berücksichtigt werden.

Die hohe experimentelle Auflösung erlaubte es zudem, bei einzelnen, zustandsselektierten Resonanzen die Linienprofile genau aufzuzeichnen. Diese wiesen eindeutig durch Quanteninterferenz zwischen radiativer und dielektronischer Rekombination verursachte Asymmetrien auf. Zum ersten Mal konnte so bei hochgeladenen Ionen die diese Asymmetrie charakterisierenden Fano-Parameter mit Meßfehlern von nur 6% bestimmt werden.

Abstract:

The photorecombination of highly charged mercury ions was studied experimentally by means of an electron beam ion trap. The KLL resonances of $Hg^{75+...78+}$ ions were scanned with an electron beam of variable energy ($45 - 54$ keV). The photorecombination process was monitored by recording the emitted radiation. By these means, the excitation energies of state-selected resonances were determined with uncertainties as low as $\pm$ 5 eV. Such accuracy made it possible for the first time to distinguish among different *ab initio* calculations for the various configurations, revealing some significant discrepancies. These predictions included QED and finite nuclear size effects as large as 160 eV and 50 eV, respectively.

The high experimental resolution allowed one to measure precisely the line profiles of state-selected resonances in individual charge states, which showed clear asymmetries arising from quantum interference between radiative and dielectronic recombination. For the first time in highly charged ions, the Fano parameters characterizing the asymmetry could be determined with relative uncertainties as low as 6%.

You see, wire telegraph is a kind of a very, very long cat. You pull his tail in New York and his head is meowing in Los Angeles. Do you understand this? And radio operates exactly the same way: you send signals here, they receive them there. The only difference is that there is no cat.

Albert Einstein

Contents

Introduction

The discovery and subsequent explanation of the photoelectric effect hundred years ago by Albert Einstein is considered one of the initial milestones in the development of quantum mechanics. Nowadays, the availability of more and more powerful light sources of lasers, synchrotrons and free-electron lasers, capable of delivering photons of almost any desired energy, has made it possible to study photoionization of single atoms both for inner and outer shells, and contributed greatly to our current understanding not only of atoms, but moreover of molecules, clusters, surfaces and solids.

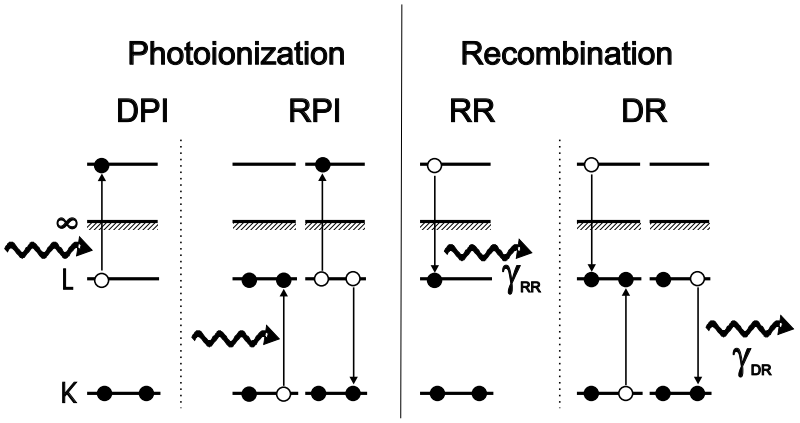

Figure 1: Two different pathways for photoionization are shown on the left side of the figure, namely direct photoionization (DPI) and resonant photoionization (RPI). The picture on the right side illustrates the time-reversed radiative recombination (RR) and dielectronic recombination (DR) processes, respectively.

The time-reversed process of photoionization, illustrated in the right hand side of Fig. 1, is photorecombination, which is as important in the physical world as its counterpart. The most common photorecombination phenomenon is the capture of a free electron by an ion under emission of a photon, dubbed radiative, or direct recombination. A slightly more complex recombination process is the capture of a

free electron with the cooperation of another electron in a bound state. Thereby the bound electron resonantly absorbs all the available energy, *i.e.*, the kinetic energy of the incoming electron and the binding energy of its final state, and undergoes a transition between two electronic states. Both, the initial ground state of the ion in the charge state q as well as the excited intermediate state of charge $q-1$ are discrete. If the intermediate state stabilizes through photon emission, one calls this phenomenon dielectronic recombination.

The central goal of this work is to study the interplay of these two mechanisms in very heavy, highly charged ions, and to extract precision data on their electronic structure for comparison with theory, making use of their collision energy dependence.

Photons emitted by electrons recombining with ions play a central role in the energy transport and in the ionization balance of plasmas. In particular, photorecombination and photoionization are very important in high temperature plasmas. Examples for high temperature plasmas on earth are found in fusion devices such as tokamaks or in the foci of powerful pulsed lasers. Knowledge of the cross sections of these interactions between ions, electrons and photons and their scaling laws are essential to model the charge state evolution of the different plasma constituents and the energy balance. Moreover, high temperatures are common in vast regions of our universe, as for example in the coronae of stars and active galactic nuclei (AGN). Here, atoms loose a large number of electrons and become highly charged ions (HCI). Their study has developed rapidly in recent years, and recombination processes of electrons with HCI have again attracted particularly strong interest.

Due to the tremendous energy concentration needed to produce HCI, these ions are extremely rare on earth. However, they can now be routinely produced in laboratories using tokamaks, heavy-ion accelerators, lasers, and ion sources such as EBIS (electron beam ion sources), ECR (electron cyclotron resonance ion source) and EBIT (electron beam ion trap), which will be explained later in this work.

In summary, the specific radiative and collisional properties of these ions are of enormous practical relevance in fields such as thermonuclear-fusion research, in the development of x-ray lasers, for spectral diagnostics in astrophysics or even for medical sciences, as in the ion irradiation tumor therapy [Sch00]. Although their difficult production still restricts a widespread use, applications of HCI experienced considerable growth in the last years and, for example, new projects have been suggested for utilizing HCI for nano-structuring and micro-analysis of surfaces.

On the other hand, highly charged ions are of generic importance in fundamental research to advance our understanding of the electronic structure of bound systems

for mainly two reasons. First, many phenomena which are normally weak in neutrals atoms quickly grow as a function of the ion charge state Z, and are thus magnified. For example, the magnetic dipole (M1) transition probability ($2\,^3\mathrm{S}_1 \rightarrow 1\,^1\mathrm{S}_0$) scales with Z^{10}. Second, HCI can be prepared as relatively simple systems, with a well-defined number of typically few electrons or even as hydrogen like systems up to U^{91+}. These ions have the least complex electronic structure, and can be studied theoretically with very high accuracy. Calculations for few-electron systems, are far more difficult and less reliable, but a strong theoretical development is taking place currently. HCI, offering the possibility to increase the number electron systematically in a controlled way experimentally complement these efforts in a ideal way.

Despite of their structural simplicity, some aspects of the physics of HCI are not easy to treat theoretically, and are not yet completely understood. This is, *e.g.*, the case for the quantum electro-dynamical (QED) contributions to the binding energy, which become strongly enhanced for the heaviest HCI due to the Z^4 scaling of the leading terms of the radiative corrections. Quantum electrodynamics is, for these reasons, essential to describe the electronic structure of HCI. The interaction of the electron with its own radiation field in the presence of the deep nuclear Coulomb potential affects the electronic energies at the 10^{-3} level, roughly a factor of thousand larger than in atomic hydrogen. In addition, the usual perturbative approach breaks down under these circumstances, and new mathematical techniques have to be applied. Here, HCI provide the unique opportunity to study QED, the most precise and most accurately tested theory among the field-theoretical approaches representing the foundations of our physical understanding, in the non-perturbative regime. Whereas a relative accuracy of 10^{-14} has been achieved in the calculation of the $1s-2s$ transition energy in atomic hydrogen, limited by the knowledge of the proton structure, the theoretical uncertainty in the precision of the $1s-2p$ transition energy in hydrogen-like uranium is accurate on the order of 10^{-5}, limited by the uncalculated higher-order Feynman diagrams as well as by nuclear excitations.

Another intriguing aspect is the tremendous increase of the electron-nucleus interaction due to the Z^{-1} scaling of the electron distance to the nucleus in H-like ions and the resulting Z^{-3} scaling of the electronic density. This phenomenon is not unique in HCI, since any $1s$ electron in a neutral, heavy element is also subject to the same exposure to unshielded nuclear fields. However, the large number of accompanying electrons makes the disentanglement of effects due to the electron-nucleus overlap, so-called nuclear size effects, far more difficult both experimentally and theoretically. Examples of the size of these effects are energy changes in the order of 10% for the hyperfine splitting of the $1s$ electrons for ions belonging to

the upper third of the periodic table, induced by the finite extension of the nuclear charge, and even still 2% shifts due to the nuclear magnetization distribution. We will see in the present work how levels can change by as much as 50 eV due to such interactions.

In general, a photorecombination experiment can be used to study QED and nuclear size effects provided that the accuracy in the determination of the collision energy is sufficiently high. This means that beams of ions or electrons or both have to be prepared and brought to overlap with well defined relative velocities, and that the photorecombination yield has to be detected.

Some twenty years ago, to prepare extremely highly charged ions required large facilities with a series of accelerators providing ion energies at least of 100 MeV/u. High ion velocities allow to strip the electrons off while passing through foil or gas targets. Experiments were difficult, since the ion velocity is poorly defined after stripping, and expensive, since most of the ions are lost in single pass experiments. More specifically, difficulties arise due to the large ion velocity ($> 0.5\ c$) implying considerable corrections to spectroscopic measurements due to the Doppler shift, or are related to the satellite electrons attached to the ions during its passage through foils. More recently it became possible to keep the ions for long periods of time orbiting in storage rings and cool the beams by merging them with a very cold electron beam. These recycled ion beams at well defined velocities, along with the merged electron beam in the cooler, enabled a new class of precision recombination experiments. In the merging region, the relative (center-of-mass) velocity of the ion-electron system can be made very small, well defined, and very low energy collisions can be studied. Thus, a large number of dielectronic recombination cross sections at low collision energies have been measured in several rings, as the CRYING in Stockholm, the ESR at GSI and the ASTRID in Aarhus. At the TSR in Heidelberg, for example, recombination of O^{7+} has been studied [KBB 90] by observing the O^{6+} recombined ions. The relative energy resolution obtained was as low as 0.4%, and cross sections achieved levels of uncertainty of 25%. More recently, the new electron target installed at the TSR storage ring has shown the capability of reducing the transverse and longitudinal temperatures at zero relative velocities to 0.5 meV and 20 μeV [OSL 05], respectively, allowing for an unsurpassed spectroscopic resolution for future recombination or dissociation experiments.

In order to access dielectronic recombination in the innermost shells of highly charged ions, however, large relative energies between electron and ion beams are necessary, and could not be realized at that time in storage rings. Thus, the most accurate innershell recombination studies were performed exploring the so-called resonant transfer and excitation (RTE) of relativistic U^{90+} ions in a hydrogen gas

target [GBB 90]. In this type of experiment the capture of an electron from the neutral target excites simultaneously the projectile in a single collision, *i.e.* the "electron beam" is represented by the bound target electrons, with the disadvantage of a large uncertainty in its velocity due to the Compton profile of the bound electrons. In order to reduce the width of the Compton profile, another experiment based on the RTE technique used the channeling of helium-like Ti^{20+} [BKR 90] ions through crystal targets, and achieved a resolution of about 1.5%. Here, the binding energy of the electrons along the central lattice channels can be very low, the electrons behave nearly as free and the relative collision energy is better defined.

The possibilities offered by electron beam driven ion sources and traps were recognized in the early 1980s, and experiments devised to explore electron-ion interactions at electron energies in the range of a few hundred eV up to 70 keV were soon after successfully demonstrated. The first results reported in the dielectronic recombination by means of an EBIT (LLNL) with Ne-like Ba^{46+} [MLK 88] were based on ideas already tested before in measurements carried out in an EBIS with Ar^{13+} ions [BCA 84]. Later, the cross sections of He-like Ni^{26+} [KML 89] were measured relatively to radiative recombination, showing a good agreement with theoretical predictions. In EBIS, experiments delivered the ratio between dielectronic and radiative recombination cross sections at relative energies of about 2 keV [ABC 90]. In these machines, as in the cooler of storage rings, the determination of resonance energies is mainly limited by the electron beam energy spread as well as by the uncertainty in determining the exact electron energy. Nevertheless, precise measurements of the most energetic deep dielectronic resonances seemed to become possible. In 1995, the dielectronic recombination of $U^{87+...90+}$ was studied by Knapp [KBC 95] at the LLNL EBIT. Resonant features at nearly 70 keV were observed, with clear indications of quantum interference between different channels of photorecombination introduced above. As will be explained later in more detail, the Z^2 dependence of the direct radiative recombination process enhances the possibility of observing quantum interference between this and the indirect DR process at a given resonance electron energy. That work has been, for nearly ten years, the clear experimental signature of this interesting phenomenon in HCI, but, at the same time, since many resonances from different charge states were blended, has been heavily disputed in the scientific community.

At the inception of the present work, one of the motivations was to be able to possibly verify the existence of these quantum interferences, and, if present, to decisively improve those results, by fully exploiting the new experimental capabilities which had become available at the Heidelberg EBIT, located at the Max-Planck-Institut für Kernphysik. The present work concentrates on the study of the photorecombi-

nation processes with highly charged $_{36}Kr^{34+}$ and $_{80}Hg^{78+...75+}$ ions. In particular, we have performed accurate studies of dielectronic recombination resonances in the KLL region, obtaining resonance energies around 50 keV with unprecedentedly low uncertainties of ± 5 eV. The absolute energy scale established in the experiment is the same for all the the five different charge states. The measured resonance energies include quantum electrodynamic contributions for the $1s$ electron (in mercury ions) of about 160 eV and finite nuclear size effects of 50 eV. Thus, our measurements can be used to test the most accurate theoretical calculations over a wide range of electronic configurations. Although those results represent a novelty by themselves, the central achievement of this work is the first characterization of the quantum interference in the photorecombination of HCI for several state-selected resonances in individual charge states through their Fano parameters.

This thesis is structured in the following manner; Chapter 1 contains a review of the relevant atomic theory and the different perturbative methods used there, as well as a detailed description of the dielectronic and radiative recombination processes, including quantum interference. Chapter 2 is dedicated to the description of the present experimental setup at the Heidelberg EBIT, its operational parameters, photon detectors, electronics and data acquisition system as well as of a test experiment on DR measurements of He-like krypton. Chapter 3 is dedicated to the results on the photorecombination and quantum interference of highly charged mercury ions.

Chapter 1

Theory

This work is dedicated to the experimental investigation of the photorecombination processes, in which a free electron is captured into a bound state of a (heavy) highly charged ion, under emission of a photon. The two main processes are called radiative recombination (RR) and dielectronic recombination (DR). The RR occurs when the electron is directly captured into a vacant state of an ion releasing the available energy through photon emission. In the DR process, the capture of the free electron resonantly excites an electron already bound to the ion into an intermediate excited state. Later, this state relaxes to a lower lying state either by emitting a photon or by an Auger process. Radiative and dielectronic recombination, therefore, are the time-reversed photoionization and Auger process, respectively. Photoionization results in the ejection of a bound electron into the continuum with a kinetic energy equal to the photon energy reduced by the ionization potential. In the Auger process, an inner shell vacancy (in many cases produced by photoionization) is filled by another electron from a higher shell. The released energy is transfered to a second electron, the so-called Auger electron, which escapes carrying the excess energy in a radiationless process.

Ab initio calculations of DR and RR are difficult to perform, since the initial state contains two charged particles, with one electron in the continuum and a complex many-electron ion. Thus, many different approximations are necessary to derive cross sections, resonance energies as well as general scaling laws. Quantitatively accurate data are needed to test the validity of these approximations and to guide the development of theory in this field.

Since these processes strongly depend on the electronic structure of the ion, a better understanding requires the correct description of its electronic structure. In the following, a brief review of the relevant atomic theory for one- and few-electron

ionic systems will be given.

1.1 Atomic structure of highly charged ions

The discovery of nuclear scattering by Rutherford [Rut11] led to the development of the Bohr [Boh13] atomic model, later improved by Sommerfeld [SU26], both of which were essential for the development of quantum mechanics. For a bound system, the time-independent Schrödinger equation [Sch26a, Sch26b] describes the quantum states of an atom or ion. Within this theory, all states with identical principal quantum number n are degenerate. Later, the relativistic Dirac theory [Dir28] showed that the atomic energy levels are split as a function of the total angular momentum J and the nuclear charge Z. The discovery of the Lamb shift [LR47] between the $2s_{1/2}$ and $2p_{1/2}$ states, which have the same energy in the Dirac theory, triggered the development of quantum electrodynamics (QED). The interaction of a bound electron with its radiation field is responsible for the observed $2s_{1/2} - 2p_{1/2}$ splitting. The largest contribution to this shift is due to the self energy of the electron, which arises through the emission and reabsorption of virtual photons by the electron. Additional contributions due to the finite size of the nucleus, in particular for heavy ions, are also observed. Section 1.1.3 is dedicated to give an overview on the QED and nuclear size corrections.

1.1.1 One-electron systems

The Schrödinger equation $H\psi = E\psi$ for an electron in the Coulomb field of an infinitely heavy ion is an eigenvalue equation for the electronic wave function

$$\left(-\frac{\Delta}{2m_e} - \frac{Z\alpha}{r}\right)\psi_{nlm}(\mathbf{r}) \;=\; E_n\psi_{nlm}(\mathbf{r})\,, \tag{1.1}$$

where m_e is the electron mass, Z the nuclear charge, $\alpha \approx 1/137$ the dimensionless fine structure constant defined as $\alpha = e^2/\hbar c$ and r the relative electron-nucleus distance. ψ_{nlm} is the wave function, with principal quantum number n, orbital angular momentum and magnetic quantum numbers, l and m, respectively. For a one electron system, the wave function ψ_{nlm} can be separated as the product of a radial and an angular component

$$\psi_{nlm} = R_{nl}(r)Y_{lm}\left(\frac{\mathbf{r}}{r}\right)\,, \tag{1.2}$$

where R_{nl} is the radial function and Y_{lm} is a spherical harmonic. The energy levels of a one-electron atom in a state with principal quantum number n are given by:

$$E_n = -\frac{m_e (Z\alpha)^2}{2n^2} , \quad n = 1, 2, 3 \ldots . \tag{1.3}$$

For convenience, we use here the atomic unit system, $m_e = \hbar = e = 1$. Possible values for the angular momentum are $l = 0, 1, ..., n-1$. The magnetic quantum number m can take the values $m = 0, \pm 1, ..., \pm l$. Here, all states with different orbital angular momentum l but with the same principal quantum number n have the same energy.

Taking into account the finite nuclear mass, a more accurate description of the hydrogen spectrum is given by substituting the electron mass m_e by the reduced nucleus-electron mass:

$$\mu = \frac{m_e M}{m_e + M} , \tag{1.4}$$

with M being the nuclear mass. Hydrogen-like ions can be described in a good approximation by simple modifications of Eq. (1.3) with the modified nuclear charge Z. However, in ionic systems with two or more electrons, where the electron-electron interaction comes into play, these equations do not hold anymore, and approximate solutions to the many-body problem have to be found.

Coming back to hydrogen, in order to solve the symmetry requirements of special relativity not present in the Schrödinger theory, Dirac proposed a relativistic Hamiltonian containing the momentum components of a free electron of mass m_e:

$$H_D = \vec{\alpha} \cdot \vec{p} c + \beta m_e c^2 . \tag{1.5}$$

It turns out that Eq. (1.5) must be treated as a matrix equation, which describes a particle with spin $s = 1/2$. Then the wave equation can be written as

$$i\hbar \frac{\partial \psi}{\partial t} = \left(\vec{\alpha} \cdot \vec{p} c + \beta m_e c^2 \right) \psi , \tag{1.6}$$

where $\vec{\alpha}$ (expressed in terms of the Pauli spin matrices $\hat{\sigma}_{x,y,z}$) and β are the 4×4 Dirac matrices, which fulfill the anticommutation relations $\alpha_i \alpha_k + \alpha_k \alpha_i = 2\delta_{i,k}$, $\alpha_i \beta + \beta \alpha_i = 0$ and $\beta^2 = 1$ and are given by

$$\alpha_x = \begin{pmatrix} 0 & \hat{\sigma_x} \\ \hat{\sigma_x} & 0 \end{pmatrix}, \qquad \alpha_y = \begin{pmatrix} 0 & \hat{\sigma_y} \\ \hat{\sigma_y} & 0 \end{pmatrix}, \qquad \alpha_z = \begin{pmatrix} 0 & \hat{\sigma_z} \\ \hat{\sigma_z} & 0 \end{pmatrix}, \tag{1.7}$$

and

$$\beta = \begin{pmatrix} 1 & 0 & 0 & 0 \\ 0 & 1 & 0 & 0 \\ 0 & 0 & -1 & 0 \\ 0 & 0 & 0 & -1 \end{pmatrix}. \tag{1.8}$$

However, more complicated Hamiltonians can be constructed in order to describe particles of spin $s = 1,\ 3/2$ and so on. The fact that the Dirac theory intrinsically includes spin effects leads to the conclusion that the spin itself is a relativistic effect.

By adding an attractive Coulomb potential $V(r) = -Z\alpha/r$ (radially symmetric) to the Hamiltonian in Eq. (1.5), one gets

$$H_D = \vec{\alpha} \cdot \vec{p}\, c + \beta m_e c^2 - Z\alpha/r\ . \tag{1.9}$$

Eq. (1.6) is then rewritten as

$$i\hbar \frac{\partial \psi}{\partial t} = \left(\vec{\alpha} \cdot \vec{p}\, c + \beta m_e c^2 - Z\alpha/r\right) \psi\ . \tag{1.10}$$

In Dirac theory the hydrogenic problem can be solved exactly, with energy levels given by

$$\begin{aligned} E_{n,j} &= m_e c^2 \left[1 + \frac{(Z\alpha)^2}{(n - \delta_j)^2}\right]^{-\frac{1}{2}}, \\ \delta_j &= j + \frac{1}{2} - \sqrt{(j + 1/2)^2 - (Z\alpha)^2}\,. \end{aligned} \tag{1.11}$$

The total energies given in Eq. (1.11) are expressed as a function of the quantum numbers n and the total angular momentum j, which is given by $j = |l - s|, ..., l + s$. The expansion of Eq. (1.11) in powers of $(Z\alpha)$ yields

$$E_{n,j} = m_e c^2 \left[1 - \frac{(Z\alpha)^2}{2n^2} - \frac{(Z\alpha)^4}{2n^3} \left(\frac{1}{j+1/2} - \frac{3}{4n} \right) + \cdots \right] . \tag{1.12}$$

By analyzing these equations we observe that the energy levels with the same principal quantum number n but different total angular momentum j are split into n components of the fine structure, unlike in the non-relativistic Schrödinger formulation given in Eq. (1.3). The first term of Eq. (1.12) corresponds to the electron rest energy, while the second term corresponds to the non-relativistic contribution to the energy. The next higher-order terms contain smaller relativistic corrections. We will see below that when two or more bound electrons have to be taken into account, this analytical representation breaks down.

Although H_D contains the main relativistic contributions for one-electron systems to all orders of $Z\alpha$, it has to be further supplemented to include quantum electrodynamic effects. Moreover, Eq. (1.12) assumes a point-like nucleus, and further corrections appear when the potential of an extended nucleus is considered.

1.1.2 Many-electron systems

The non-relativistic Hamiltonian for a system consisting of a nucleus of mass M surrounded by N electrons has the general form

$$\hat{H} = \sum_{i=1}^{N} \frac{\hat{p}_i^2}{2\mu} + \sum_{i=1}^{N} \hat{V}(i) + \sum_{i<j} \hat{W}(i,j) \ . \tag{1.13}$$

The Hamiltonian is expressed in terms of the center-of-mass coordinate R and the associated momentum of the i-th electron $\hat{p}_i = \frac{\hbar}{i}\nabla_i$. The first term in Eq. (1.13), corresponding to the kinetic energy, contains the reduced mass μ of an electron. The second term describes the electrostatic interaction of the electrons with the nuclear charge Z:

$$\hat{V}(i) = -\frac{Z\alpha}{r_i} , \tag{1.14}$$

and the third term describes the mutual electrostatic repulsion potential between electrons:

$$\hat{W}(i,j) = \frac{1}{|r_i - r_j|} . \tag{1.15}$$

This term becomes very important even in the case of two-electron (He-like) ions. Equation (1.13) can not, in general, be solved analytically because of the presence of the electron-electron interaction term. Nevertheless, various approximations have been applied to calculate these interactions more or less accurately.

The extension of the Dirac Hamiltonian to account for relativistic effects in a many-electron system is not straightforward at all. The relativistic correction to the non-relativistic Coulomb repulsion between two electrons is known as the Breit interaction and can be introduced into the Hamiltonian as an operator of the order $(Z\alpha)^2$. The resulting Hamiltonian is usually divided in a non-relativistic part and a relativistic part (H_{REL}):

$$H_{REL} = H_{mass} + H_{Darwin_1} + H_{SO} + H_{SOO} + H_{SS} + H_{SSC} + H_{OO}\,. \qquad (1.16)$$

H_{mass} is the relativistic mass-correction term. H_{Darwin_1} is the so-called one-body Darwin term, which has its physical origin in the rapid small-scale fluctuations (*Zitterbewegung*) causing the electron to see a smeared-out Coulomb nuclear potential. The so-called spin-orbit term H_{SO} represents the spin-orbit interaction of a given electron. For $Z > 26$, H_{SO} dominates over the Coulomb repulsion. Additional two-electron effects are classified as fine structure terms, such as spin-other-orbit (SOO) and spin-spin (SS) interactions, and non-fine structure terms, like spin-spin contact (SSC), orbit-orbit interactions (OO) [BS57].

Theoretical methods for the many-body problem

One of the most widely used methods is the Hartree-Fock approximation. It has been applied thanks to computer codes such as those developed by Cowan [Cow67, CG76] and Froese-Fischer [Fro72, Fro77]. Here, the motion of the single electron is calculated using an effective potential generated by the averaged potential caused by all the other electrons, which is assumed not to change in time. Although the correlated motion of the electrons is not taken into account, this method is quite useful and it achieves a reasonable accuracy of about 1% or even better in the determination of energy levels.

Here, the wave function Ψ is approximated by a single Slater determinant Ψ consisting of one orbital for each of the n electrons:

$$\Psi = \frac{1}{\sqrt{n!}} \begin{vmatrix} \psi_a(1) & \psi_a(2) & \dots & \psi_a(n) \\ \psi_b(1) & \psi_b(2) & \dots & \psi_b(n) \\ \dots & \dots & \dots & \dots \\ \psi_n(1) & \psi_n(2) & \dots & \psi_n(n) \end{vmatrix} . \tag{1.17}$$

Then a set of orbitals which minimizes the total energy is determined. The calculation starts with a set of initial orbitals and refines them iteratively. Therefore, the Hartree-Fock method is often called a self-consistent field (SCF) approach. Magnetic interactions are not yet included here, but they are taken into account in modified revisions, such as the relativistic Hartree-Fock method. It can be used as a starting point in perturbation theory for light atoms and ions. However, for heavy ions the effective fine structure constant term (αZ) is no longer a small number, and more higher-order relativistic terms are needed.

Another way of solving this problem is to use the following one-body Dirac Hamiltonian:

$$\hat{H}_D = \hat{\alpha} \cdot \hat{p}\, c + \beta \mu c^2 + \hat{V} + \hat{W}_d - \hat{W}_{ex} \, , \tag{1.18}$$

where $\hat{W}_d$ represents the total electrostatic potential due to the $N-1$ other electrons of the Slater determinant Ψ, and $\hat{W_{ex}}$ is the exchange potential between electrons. Thus, the relativistic effects to the one-electron problem are included consistently. The search for self-consistent eigenfunctions of $\hat{H}_D$ is called the *Dirac-Fock method.*

Another relativistic method, known as the *Relativistic Many-Body Perturbation Theory* (RMBPT), has also been extensively used for many years. The non-relativistic approach developed by Kelly [Kel66] was extended later to relativistic problems by Johnson and Sapirstein [JS86]. By replacing the Coulomb repulsion potential term (relativistic Hamiltonian) by a localized, one-electron model potential, a complete set of one-electron eigenfunctions including continuum states is obtained. In this model, each bound electron state satisfies the one-electron Dirac equation. The difference between the Coulomb repulsion term and the model potential is treated as a perturbation. This perturbation is expanded in series of the total energy and wave function by systematically summing single, double, and multiple excitations from the ground state. In most cases, an atomic state being an eigenfunction of the Dirac-Fock equation with a closed core potential is used as a reference state. Modern approaches to RMBPT typically use basis sets whose projection operators are implemented by restricting all sums to positive energy eigenstates.

RMBPT converges rapidly for highly charged ions, making possible to achieve high accuracy already with only the first and second order perturbation terms. However, for neutral atoms and light ions the third, fourth and even higher-order terms are commonly required.

The *1/Z expansion approximation* uses the fact that the electron-electron interaction is $1/Z$ times weaker than the nuclear potential. This method uses antisymmetrized products of hydrogenic orbitals in order to perform a perturbation expansion. It has been used in calculations of few-electron heavy-ion systems, for instance, by *Safronova* and co-workers [IS75]. The 1/Z expansion is a suitable method for heavy ions with only few electrons. This method is applied to both the relativistic [SU79] and the non-relativistic domains.

A certain problem arises from the fact that Dirac-Fock wave functions with a minimum number of radial functions describing only the occupied states do not account for the electron-electron correlation. This issue can be solved by adding extra configurations, called *configuration state functions* (CSF), representing the interaction with different unoccupied configurations. They must have the same total angular momentum J and parity as the occupied configurations. An ansatz for the correlated N-electron wave function ψ is a linear combination of N_S Slater determinants Ψ_ν, which includes various N-electron configurations:

$$\psi = \sum_{\nu=1}^{N_S} c_\nu \Psi_\nu \ . \tag{1.19}$$

The c_ν are the mixing coefficients. In this way antisymmetrized many-electron wave functions are defined. If the sum in Eq. (1.19) includes sufficient terms, this procedure can in principle approximate the exact solution to any desired degree of accuracy. However, an enormous computational effort would be needed if the basis is made too large, but it is solved without much difficulty if the number of configurations introduced in the ansatz (1.19) is judiciously chosen. Then, a simple diagonalization of the Hamiltonian matrix, which may have a dimension of up to several thousands, in the subspace spanned by the Ψ_ν yields a good approximation of the exact eigenstates. This is called *configuration interaction* (CI) technique. If the calculations not only optimize the mixing coefficients c_ν, but also the one-electron wave functions, then this is called the *Multi-Configuration Dirac-Fock* (MCDF) method. It starts with initial estimates of the wave functions, *e.g.*, hydrogenic or Thomas-Fermi one-electron orbitals, and a CI calculation providing initial mixing coefficients. Due to the optimization of the wave functions, this method can reach high accuracy even with a limited number of CSF.

Another possibility is to use a *Sturm-Liouville* basis in which the single particle states are characterized by their similarity to the eigenfunctions of the pure Coulomb potential. The Sturm-Liouville states form a complete set in which states with different principal quantum numbers are no longer orthogonal.

1.1.3 QED and nuclear size effects: the Lamb shift

QED is a field theory which describes all phenomena involving charged particles interacting with the quantized radiation field. Interactions between the charged particles are mediated by the exchange of photons, the quanta of the electromagnetic field.

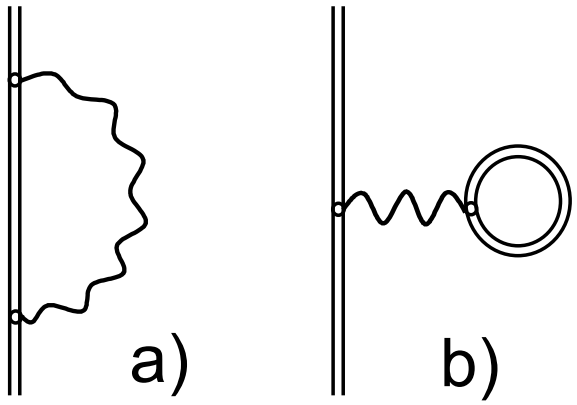

Figure 1.1: Feynman diagrams for the self energy (a) and vacuum polarization (b) correction of a bound electron (in the order of α, two vertices). The double lines indicate electron wave functions and propagators in the external Coulomb potential of the nucleus. The wavy lines represent the virtual photons.

These interactions are generally described with the well known Feynman diagrams. The order of a Feynman diagram in α is defined as the number of virtual photon lines, or loops, that it contains. For a bound electron, the first two so-called one-loop corrections are the self energy (SE) and the vacuum polarization (VP) terms, whose Feynman diagrams are shown in Fig. 1.1. The dominant QED correction in one-electron systems is the SE. It is due to the emission and reabsorption of a virtual photon by the bound electron in a very brief period of time without violating the Heisenberg uncertainty relation. In order to avoid the infinite mass divergency which appear in the calculations, appropriate regularizations are required; this can be achieved by renormalizing the electron mass. The earliest calculations for the self energy correction were performed in the 1950s by Brown, Langer and

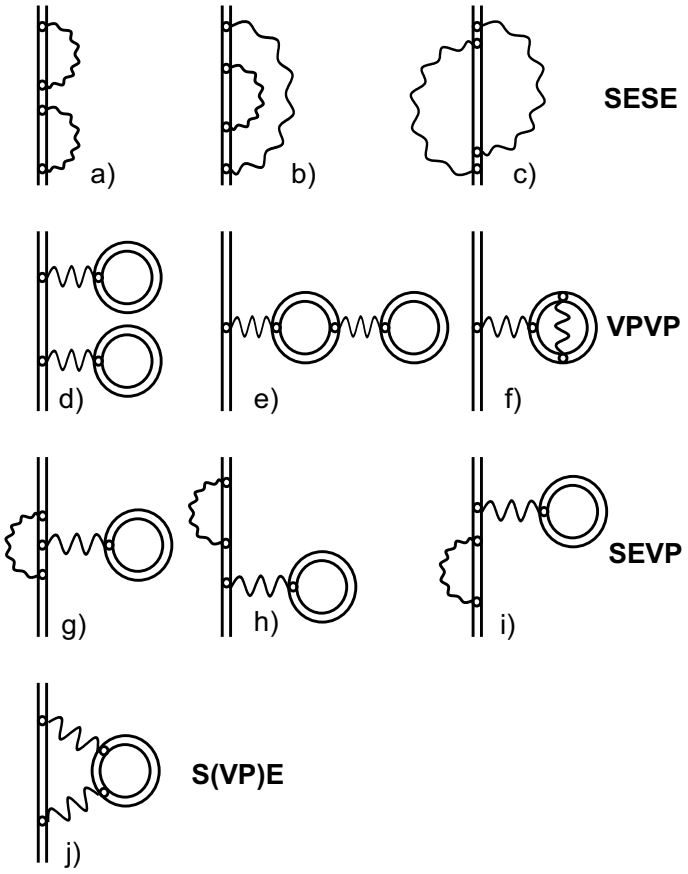

Figure 1.2: Feynman diagrams for various QED corrections in order α^2.

Schaefer [BLS59]. Modern variants of the self energy calculation have been carried out by Mohr [Moh73, MS93].

The vacuum polarization correction (see Fig. 1.1b) can be described as an interaction of the bound electron with virtual electron-positron pairs. In the case of heavy ions, the propagation of those fermionic pairs in the strong field of the nucleus is described relativistically by the Coulomb-Dirac Green's function [MPS98]. The expansion of this propagator in powers of the coupling constant $Z\alpha$ yields in the first order the so-called Uehling part of the VP correction. The remaining orders in $(Z\alpha)^n$ for $n \geq 3$ are subsumed in the Wichmann-Kroll correction [WK56]; according to Furry's theorem, there are no contributions with even powers of n.

Besides of SE and VP, further contributions of second order in α appear in the presence of a nuclear field. The required complex calculations have not yet been completed, in particular in the case of few-electron ion systems. However, they have been carried out to the lowest-order in $Z\alpha$ for He- and Li-like systems.

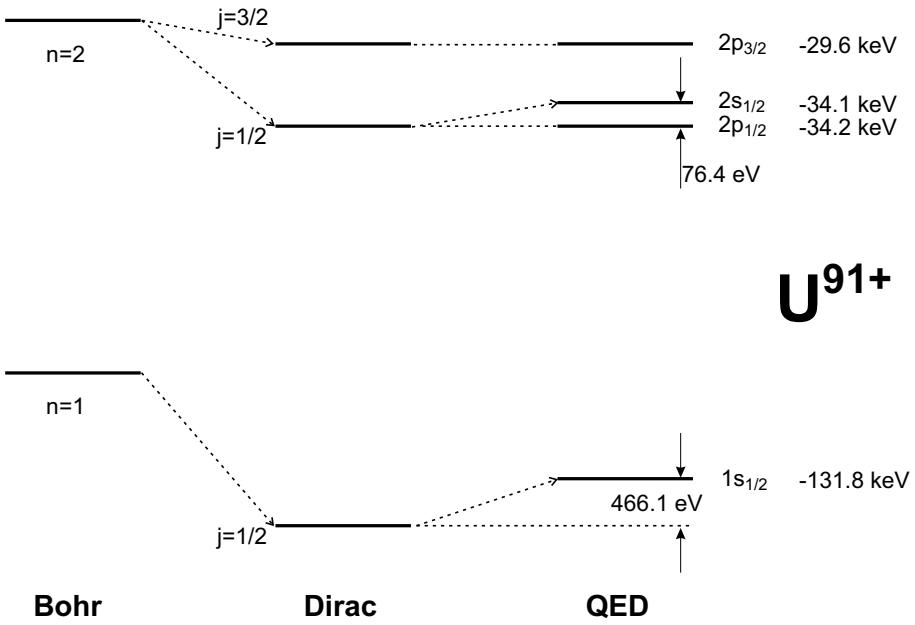

Figure 1.3: Level scheme of hydrogen-like uranium U^{91+} according to various atomic models. The $1s$ Lamb shift is taken from Ref. [YAB 03]. The numbers on the right hand side indicate the approximate binding energies for different levels.

Some Feynman diagrams describing additional contributions to the Lamb shift in hydrogen-like ions are displayed in Fig. 1.2. They are *e.g.*, diagrams containing two-photon self energy SESE, second-order vacuum polarization corrections VPVP, mixed self energy-vacuum polarization SEVP, and the effective self energy-vacuum polarization contribution S(VP)E. Numerical results for these second-order corrections can be found in [BMP 97]. While the VPVP, SEVP and S(VP)E can be calculated exactly, the more complex two-photon self-energy correction remains one active research topic [MS98, LPS 98].

Nuclear size effects

The influence of the nucleus has to be taken into account when a certain level of accuracy is required in electronic structure calculations. Since the nucleus is not a point charge, but it has a finite charge and magnetization distribution, the distortion of the central potential has to be considered. These corrections can be rather large for heavy ions. The distribution of the nuclear charge has to be introduced into the Dirac equation. Due to uncertainties in our knowledge of nuclear parameters, some limitations when testing QED are unavoidable.

For a homogeneous nuclear charge distribution, the following expression (accurate

to 0.2%) is obtained for the nuclear size effect in $ns_{1/2}$ states for hydrogen-like ions [SAY00]:

$$\Delta E_{FS}\left(ns_{1/2}\right) = \frac{(\alpha Z)^2}{10n}\left[1+(\alpha Z)^2 f_{ns}(\alpha Z)\right]\left(2\frac{\alpha Z}{n}\frac{R}{\hbar/m_e c}\right)^{2\gamma} m_e c^2\,, \qquad (1.20)$$

where $\gamma = \sqrt{1-(\alpha Z)^2}$. R is given in first order in terms of the root-mean-square radius ($\sqrt{\langle r^2\rangle}$) as $\sqrt{5/3}\sqrt{\langle r^2\rangle}$ [NM95]. The function f in Eq. (1.20) is explicitly written for $n=1$ and $n=2$ states as

$$\begin{aligned}(n=1)\quad f_{1s_{1/2}} &= 1.380 - 0.162\,(\alpha Z) + 1.612\,(\alpha Z)^2\,,\\ (n=2)\quad f_{2s_{1/2}} &= 1.508 + 0.215\,(\alpha Z) + 1.332\,(\alpha Z)^2\,.\end{aligned}$$

Figure 1.4 shows the contributions to the finite nuclear size effect for the $1s_{1/2}$ and $2s_{1/2}$ states as a function of the nuclear charge Z. The largest contributions

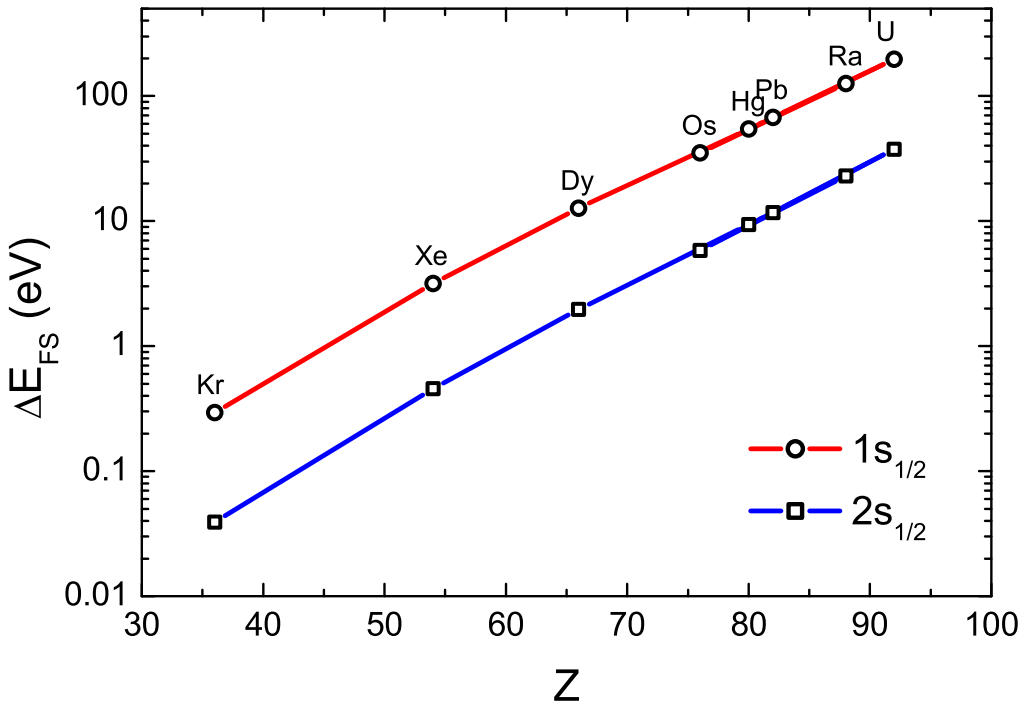

Figure 1.4: Finite nuclear size contribution ΔE^{FS} to the $1s_{1/2}$ and $2s_{1/2}$ states as a function of the nuclear charge Z. The curves were calculated using Eq. (1.20).

are observed for the $n = 1$ state. For instance, the contribution to the $1s_{1/2}$ state of a highly charged mercury ion ($Z = 80$) is already as large as 54 eV. The isotopic effect, *i.e.*, the difference in these contributions due to the mass and volume of the nucleus for two different isotopes, increases also with Z. From Eq. (1.20), the isotopic effect between the heavy nuclei of ^{232}U and ^{238}U is calculated to be ≈ 1.16 eV. The measurement of this tiny energy in comparison with the KLL dielectronic recombination resonance excitation energies in He-like uranium ions (≈ 60 keV) or with the binding energies for the K-shell (≈ 132 keV) challenges the most accurate experimental techniques.

Experimental tests

One way of testing QED is to measure the *Lamb shift* in one- or few-electron systems. The Lamb shift is defined as the difference between the actual binding energy E_{exp} of a given electronic state and the corresponding theoretical Dirac energy E_{Dirac} in the Coulomb field of a point-like nucleus (see Fig. 1.3):

$$\Delta E_{Lamb} = E_{exp} - E_{Dirac}\,. \tag{1.21}$$

The Lamb shift consists of two parts: the pure QED contributions, which are mainly due to SE and VP corrections, and nuclear structure effects mainly those caused by the finite size and shape (FS) as well as virtual excitations or the polarization of the nuclear charge density distribution:

$$\Delta E_{Lamb} \approx \Delta E_{SE} + \Delta E_{VP} + \Delta E_{FS}\,. \tag{1.22}$$

The Lamb shift for the $1s$ electron in heavy ions can be calculated with a total relative precision of 10^{-3}. A recent calculation for the Lamb shift of the $1s_{1/2}$ ground state in $^{238}U^{91+}$ [YAB 03] yields $466.11 \pm 0.39 \pm 1.30$ eV, where the two error bars arise from the uncertainty in the effect of finite nuclear size and in the determination of the SESE contribution, respectively. Table 1.1 shows the different contributions. The labels added in the table $(a, b, c, ...)$ are referred to the diagrams shown in Fig. 1.2. The diagram a was, in one case, calculated with the irreducible mass. As shown in Fig. 1.3, the self energy and finite nuclear size corrections reduce the binding energy by approximately 355 eV and 199 eV, respectively. By observing the Lyman-α_1 transitions ($2p_{3/2} - 1s_{1/2}$) associated with the electron capture by

Table 1.1: One-electron Lamb shift contributions (eV) for the $1s_{1/2}$ state in hydrogen-like uranium ($^{238}U^{91+}$) (from [YAB 03]). Nuclear size effects are based on a nuclear radius $\langle r^2 \rangle^{1/2} = 5.860(2)\ fm$. The estimated uncertainties are due to missing diagrams and limited knowledge of the nuclear radius.

Finite nuclear size		198.81	± 0.38	
First order	SE	355.05		
	VP	-88.60		
Second order	SESE (a, irred.)	-0.97		
	SESE (a, red., b, c)	1.28		± 1.28
	VPVP (d)	-0.22		
	VPVP (e, f)	-0.75		± 0.20
	SEVP (g, h, i)	1.12		
	S(VP)E (k)	0.13		± 0.04
	Total (a-k)	0.59		± 1.30
Total recoil		0.46		
Nuclear polarization		-0.20	± 0.10	
Sum of correction		466.11	± 0.39	± 1.30
Dirac value (point nucleus)	binding energy	-132279.92	± 0.01	

bare ions, the total 1s Lamb shift of H-like uranium has been measured in the ESR storage ring at the GSI resulting in 460.2 ± 4.6 eV by Gumberidze [GSB 05].

Calculations for few-electron systems, even for the He-like ions become very complicated due to the electron-electron interaction. For instance, QED contributions to the energy of a He-like system can be expressed as the sum of two independent one-electron contributions and a two-electron contribution. This last one, the electron-electron interaction term, includes the one- and two-photon exchange, self energy and vacuum polarization screening diagrams and higher order corrections. Some of their corresponding Feynman diagrams are shown in Fig. 1.5. Modern theoretical developments in QED calculations of high-Z many-electron ions are reviewed *e.g.*, by Lindroth in [Lin95].

Most experiments performed for the study of the Lamb shift in more complex heavy ions have also concentrated in measuring x-ray energies. The experimental uncertainties are in the best cases about 10^{-4} for the total energy. In a beam-foil experiment, Schweppe [SBB 91] determined the Lamb shift of the lithium-like uranium (U^{89+}) $2s_{1/2}$ level with an uncertainty of 0.1 eV using Doppler-tuned spectroscopy. In a different approach, Brandau [BKM 03] measured the $2s_{1/2} - 2p_{1/2}$

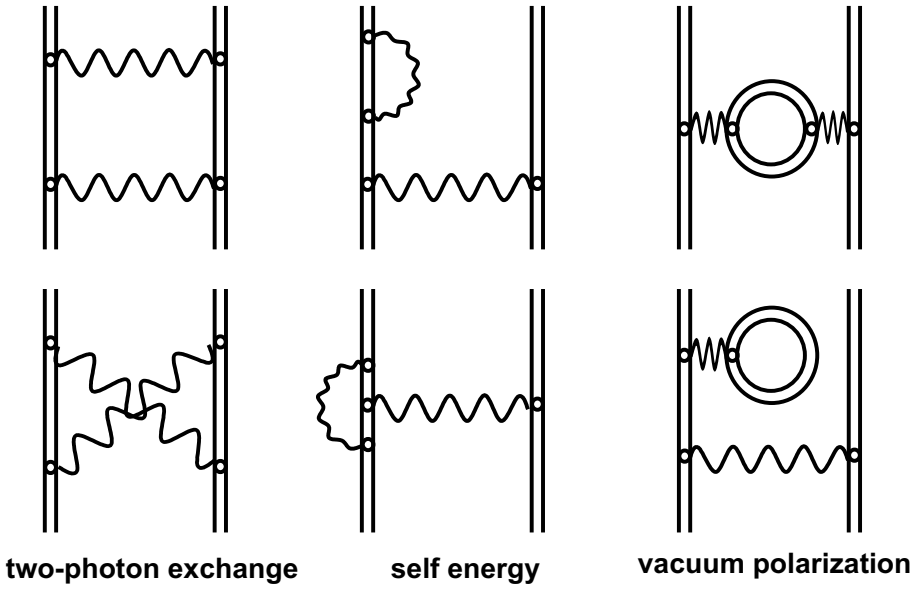

Figure 1.5: Feynman diagrams for the electron-electron interaction corrections corresponding to the Lamb shift in two-electron ions.

energy splitting for few Li-like ion systems (Au, Pb and U) using low energy dielectronic recombination resonances and extrapolating to the Rydberg series limit, and reviews the different experimental and theoretical results. An experiment with trapped Li-like Bi^{80+} at the SuperEBIT [BOS 98] measured the $1s^2 2p_{3/2} - 1s^2 2s_{1/2}$ transition energy with a relative accuracy of 1.4×10^{-5}, and resolved the hyperfine splitting of the ground state $1s^2 2s$ configuration, hence, testing the predictions of QED contributions to this transition energy within 1.5×10^{-3}.

1.2 Photorecombination in electron-ion collisions

This section deals with the basic theory of *resonant* dielectronic recombination (DR) and *non-resonant* radiative recombination (RR).

Figure 1.6 shows schematically the direct process (RR) through the top path and the resonant DR process (bottom path) which passes via an intermediate state. Within the resulting scheme, both processes start at the same initial state and end on the same final state of the recombined ion. This is the essential premise for the two processes to be able to interfere.

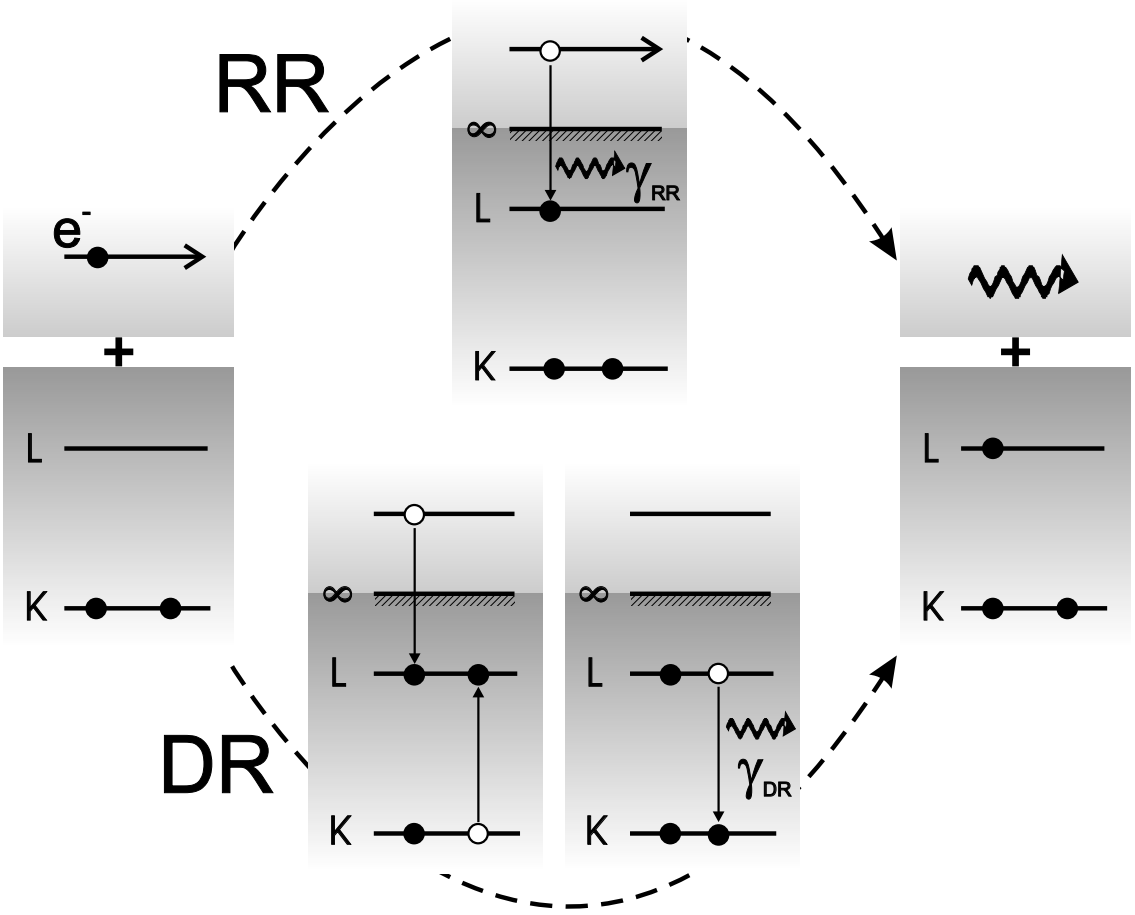

Figure 1.6: Scheme for the dielectronic (DR) and radiative (RR) recombination processes, respectively. Both, the direct recombination (RR) and the two-step recombination (DR) processes start on the left side of the sequence. RR finishes in one single step while the DR goes to the same final state via an intermediate excited state.

1.2.1 Dielectronic recombination

Dielectronic recombination (DR) is a consequence of the electron-electron interaction between a continuum electron and one of the bound electrons in an ion. This process can obviously not happen in the case of bare ions. Here, first, the free electron is captured into a vacant excited state of the ion A^{q+} transferring non-radiatively the energy difference to a core electron with energy E_1, which is simultaneously promoted to a higher laying excited state with energy E_2 of the ion, thus forming an intermediate (singly, doubly or multiply excited state),

$$A^{q+} + e^- \rightarrow \left[A^{(q-1)+}\right]^* \rightarrow \left[A^{(q-1)+}\right] + \hbar\omega_{DR}\,. \tag{1.23}$$

This resonant process, can only happen when the energy difference between the core electron state and the state in which the second electron is excited is equal to the kinetic energy of the free electron E_e plus the binding energy I_p of the recombined state. This resonance condition is written as

$$\Delta E = E_2 - E_1 = E_e + I_p \,. \tag{1.24}$$

In the second step, the formed excited state $\left[A^{(q-1)+}\right]^*$ may decay as well to the ground state via an Auger autoionization process, where again there is a change in the ion charge as the ion returns to its initial state. However, in highly charged ions, radiative deexcitation via emission of one or more photons strongly dominates. While the Auger rates are proportional to the electron-electron interaction and show only a small dependence on Z, the radiative decay rates increase with up to very high powers of Z for magnetic, two photon or higher-order transitions (with Z^4 for simple photon dipole allow transitions). In this way, radiative stabilization of the excited intermediate states is usually the dominant channel in highly charged ions, in contrast to neutrals, where Auger processes dominate.

Dielectronic recombination is the time-reversed Auger process and, thus, the corresponding pathways are labeled accordingly. For instance, in a KLL DR resonance for a He-like initial state, as shown in Fig. 1.6, the free electron is captured into the L-shell of an ion, while a bound electron is promoted from the K-shell to the L-shell to form an excited $1s2l2l'$ state. This intermediate excited state decays radiatively into the $1s^22l$

$$e^- + A^{(Z-2)+}\ (1s^2) \ \rightarrow\ \left[A^{(Z-3)+}\right]^*\ (1s2l2l') \tag{1.25}$$

$$\rightarrow A^{(Z-3)+}\ (1s^22l \text{ or } 1s^22l') + \hbar\omega(K_\alpha)\,. \tag{1.26}$$

In a KLM resonance, the electron is captured into the M-shell, while a K-shell electron is excited to the L-shell (or vice versa), forming the $1s2l3l'$ state. Consequently, this doubly excited state decays radiatively to $1s^23l'$ or $1s^22l$ emitting either a K_α or K_β x-ray line, respectively.

The first theoretical attempts to describe the DR process were made in the 1940s by Massey and Bates [MB42]. Later, Burgess pointed out that DR is of significant importance when high temperature plasmas, like those observed in the solar corona, are considered [Bur64]. The first measurements on DR cross sections were performed in the 1980s [MNF 83, DDM 83]. However, due to low statistics and limited

energy resolution as well as high backgrounds, these experiments could not resolve the structure of most of the observed resonances. In the energy balance of high temperature fusion plasmas, dielectronic recombination has been shown to play an important role. Therefore, precise knowledge of DR processes becomes one of the critical issues modelling fusion plasma reactors.

DR cross section

Following the process given by (1.23) for the different states defined and taking into account the resonance condition (1.24), one can introduce the so-called isolated-resonance approximation, where there are no overlapping resonances with the same total angular momentum in the (doubly) excited state $|d\rangle$. The DR cross section can then be written as the product of the resonant electron capture probability to form the intermediate state and its fluorescence yield, defined as the branching ratio between the radiative and the Auger widths of the intermediate state, Γ_r and Γ_a, respectively. Thus,

$$\sigma_{DR}(E_e) = \frac{2\pi^2\hbar^3}{p_e^2} V_a\,(i \to d)\, L_d(E_e)\, \omega_d\,, \tag{1.27}$$

$$\omega_d = \frac{\Gamma_r}{\Gamma_r + \Gamma_a} = \frac{\Gamma_r}{\Gamma_d}\,. \tag{1.28}$$

Here, $V_a(i \to d)$ denotes the total probability per unit of time for the resonant electron capture from $|i\rangle$ to $|d\rangle$. p_e is the momentum corresponding to the electron initial energy $E_e = \sqrt{p_e^2c^2 + m_e^2c^4} - m_ec^2$ and Γ_d is the total width of the intermediate state. The function $L_d(E_e)$, reflecting the Lorentzian shape of the resonance, is defined as

$$L_d(E_e) = \frac{\Gamma_d/2\pi}{\left(E_e - E_r\right)^2 + \Gamma_d^2/4}\,, \tag{1.29}$$

with the normalization $\int L_d(E_e)dE_e = 1$. E_r is the resonance energy. Considering the principle of detailed balance, the dielectronic capture probability V_a is related to the autoionization probability A_a as

$$V_a(i \to d) = \frac{g_d}{2g_i} A_a(d \to i)\,, \tag{1.30}$$

where g_d and g_i are the statistical weights (degeneracies) of the quantum states of the intermediate and initial states, respectively. The factor 2 reflects the two possible spin orientations of an electron in the continuum state. Combining the previous Eqs. (1.27-1.30), we finally obtain the following expression for the DR cross section

$$\sigma_{DR}(E_e) = \frac{\pi\hbar^2}{p_e^2}\frac{g_d}{2g_i}\frac{\Gamma_a(d\to i)\Gamma_r(d\to f)}{(E_e - E_r)^2 + \Gamma_d^2/4}\,. \tag{1.31}$$

The DR resonance strength S_{DR} is also a useful quantity for describing the DR process. In the case of a very narrow resonance width, the theoretical line profile can be approximated by a delta function. The resonance strength is defined as

$$S_{DR} \equiv \int \sigma_{DR}(E)dE = \frac{2\pi^2\hbar^2}{p_e^2}\frac{g_d}{2g_i}\frac{\Gamma_a\Gamma_r}{\Gamma_d}\,. \tag{1.32}$$

1.2.2 Radiative recombination

In ion-electron collisions the *non-resonant* radiative recombination occurs at any electron energy, thus also at the DR resonance energy. Here, a free electron with an energy E_e is captured into a vacant state with the binding energy I_p, and the excess energy is taken away by the emitted photon. Therefore, the process can be written as:

$$A^{q+} + e^- \to A^{(q-1)} + \hbar\omega_{RR}\,, \tag{1.33}$$

with the photon energy

$$\hbar\omega_{RR} = E_e + I_p\,. \tag{1.34}$$

Figure 1.7 shows the photorecombination of krypton ions (photon energy versus electron energy). Here, the diagonal lines represent the RR process, where the photon energy increases with the electron energy according to Eq. (1.34). In addition to RR, we can also distinguish bright spots due to the resonant DR processes (see Eq. (1.24)).

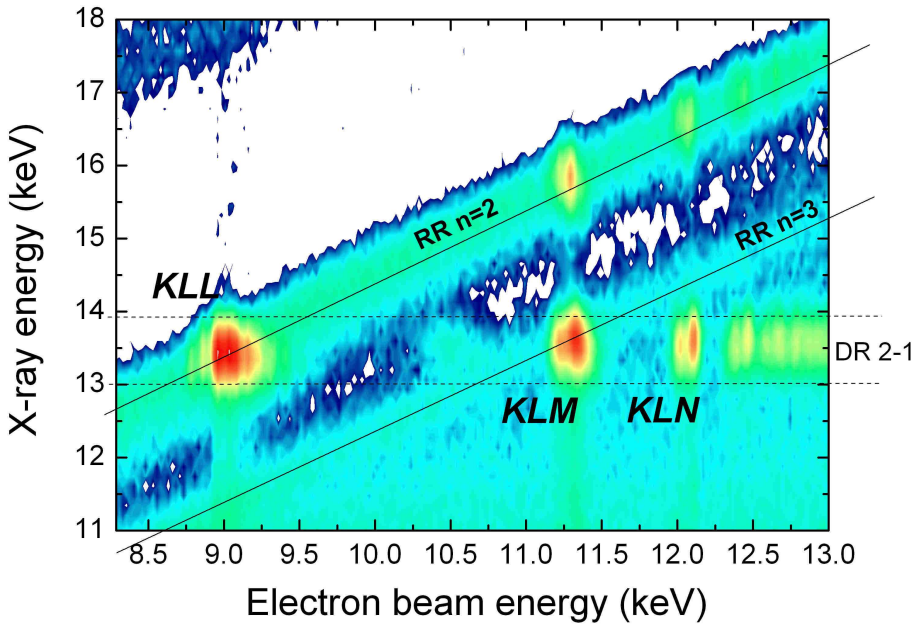

Figure 1.7: Scatter plot of the photorecombination of krypton ions. Diagonal bands are visible due to RR into the $n = 2$ and $n = 3$ shells, respectively. The horizontal line indicates the transitions from $n = 2 \rightarrow 1$ due to DR process. As singular bright spots we can characterize DR resonances. This two-dimensional map was taken during the present work (see section 2.6).

In high-temperature low-density laboratory and astrophysical plasmas, RR radiation is used for the determination of the plasma temperature and the ionization-recombination balance. Since radiative recombination cross sections can be estimated readily with reasonable accuracy, RR can be used to normalize experimental data and determine the cross sections of other processes competing with it. Thus, RR is a useful tool in the diagnostic of plasmas. For instance, the method of line-ratio measurements is used as a temperature diagnostic for plasmas [BRF02]. Also in electron-ion collision experiments, this process is well-suited for the understanding of fundamental reactions. As shown above, in this process a photon of well-defined energy is emitted. Such x-rays from bare- and hydrogen-like heavy ions provide new chances of testing QED [SKE 97]. RR x-ray measurements using free electrons and a dense ion beam allow accurate observations of the Lamb shift in hydrogen-like uranium ions [SMB 00].

The first measurements of RR rates were performed with merged-beam techniques, and showed a good agreement with calculations based on the Kramers formula (see below Eq. (1.36)). This process has been studied in storage rings like the TSR in Heidelberg [MSW 91], with ion charge states ranging from Si^{11+} to Se^{23+} [Mül95]. These experiments provide absolute cross sections and RR rates for

center-of-mass energies from 0 eV to a few keV.

At the GSI in Darmstadt, absolute RR rates of heavier ions such as Au^{76+} and U^{28+} have been measured with an electron energy resolution of 10 meV. The RR cross section measurements on U^{28+} at low electron energies are not in accord with the theoretical results [MSW 91], being underestimated by a factor of 20 to 50. The reasons for this RR enhancement at small, close to zero relative energies between the electron and ion beams that have been observed in all storage ring experiments and were investigated in great detail (see also [GHB 00] in the TSR) are unclear until the present day.

RR cross sections

Formulae for the cross section of the radiative recombination in simple systems, namely, hydrogenic and bare ions have been derived by Kramers [Kra23] and Bethe and Salpeter [BS57]. Due to the fact that RR is the inverse photoionization process, they made use of the principle of detailed balance. Radiative recombination can be applied to study photoionization, in particular in cases where no photoeffect experiments can be performed directly with present technologies. For instance, by observing RR into excited states, the calculated photoionization cross section of the initially excited state of non-hydrogenic ions can be tested [APS92]. In the photoionization process, the photon with energy $\hbar\omega$ is absorbed by the projectile ion which emits an electron with momentum p (photoionization, see Eq. (1.62) in section 1.3). As the photoionization cross sections can be calculated using the Bethe and Salpeter formula [BS57], RR cross sections may be obtained by using the Milne relation:

$$g_q \sigma_{ph}(\omega) = \frac{2 m_e c^2 E_e}{\hbar^2 \omega^2} g_{q+1} \sigma_{RR}(E_e) \,, \tag{1.35}$$

where $g_q = 2n^2$ (sum of l levels in a given n, times 2 accounting for the spin) and $g_{q+1} = 1$ are the statistical weights of the final and initial states, respectively. Using σ_{ph} (see Eq. 1.63) in Eq. (1.35), Kramers derived the following expression for the RR cross section

$$\sigma_{RR}^{Kramers} = \frac{32\pi a_0^2 \alpha^3}{3\sqrt{3}} \frac{Z|E_0|^{3/2}}{(E_0 + E_e)\, E_e} \,, \qquad E_0 = Z^2 \mathbf{Ry}/n^2 \,. \tag{1.36}$$

Here, as in Eq. (1.35), E_e is the kinetic energy of the free electron and **Ry** is the Rydberg constant (13.6 eV). This expression (1.36) can be simplified [BS57] for the recombination cross sections into high-n states. The following formula provides cross sections for hydrogenic ions which are in good agreement with experimental results for the capture into a state with principal quantum number n:

$$\sigma_n = 2.10 \times 10^{-22} \frac{q^4 \mathbf{Ry}^2}{n E_e \left(q^2 \mathbf{Ry} + n^2 E_e\right)} \; cm^2 \; . \tag{1.37}$$

Here, q is the charge of the bare ion. Exact calculations of RR cross sections were carried out in the dipole approximation by Stobbe [Sto30] for bare ions. In the non-relativistic Stobbe formula for radiative recombination into an empty K-shell, the cross section is given by

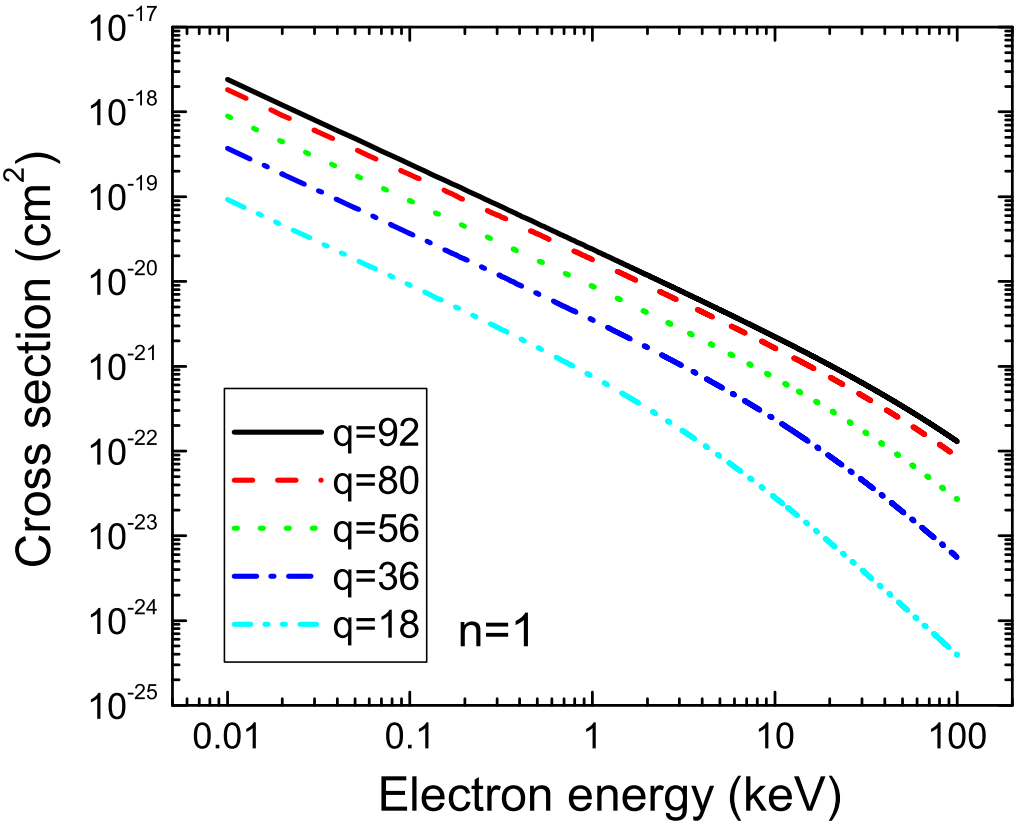

Figure 1.8: Total RR cross section into the K-shell as a function of the electron energy calculated using Eq. (1.37). The parameters q denotes the nuclear charge of bare ions.

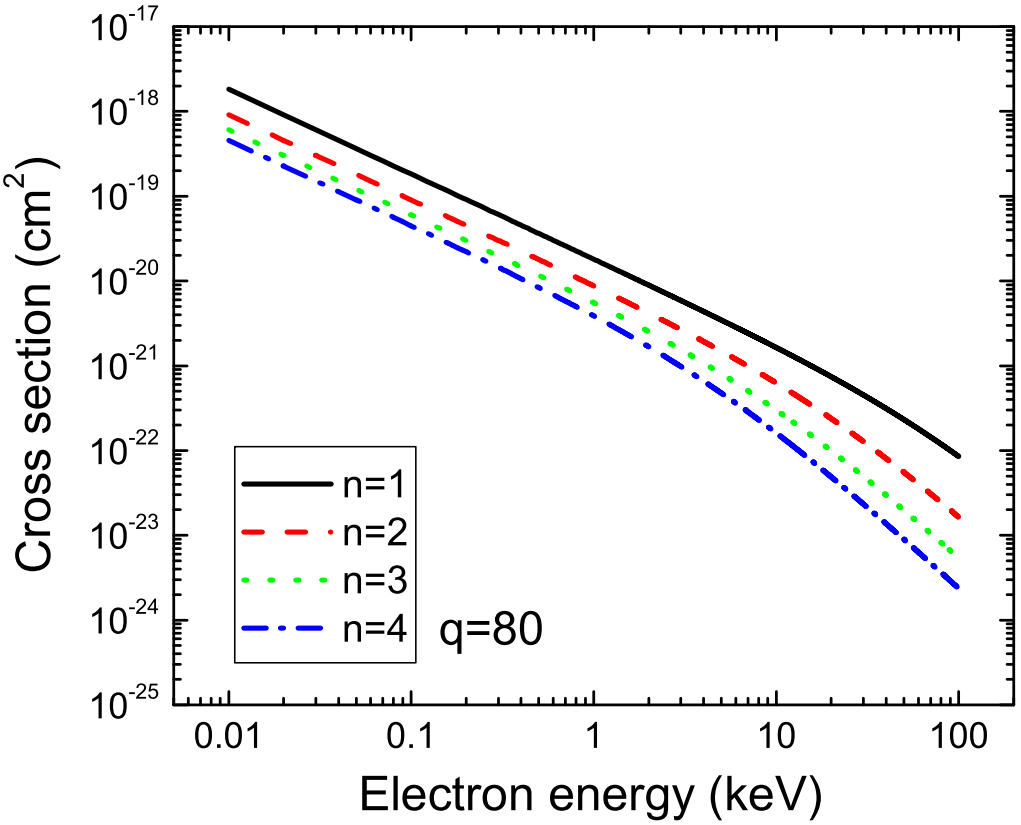

Figure 1.9: Total RR cross sections for Hg^{79+} ions as a function of the electron energy calculated using Eq. (1.37), plotted for different quantum numbers n.

$$\sigma_{RR}^{Stobbe} = \frac{2^8\pi^2\alpha}{3}\left(\frac{\nu^3}{1+\nu^2}\right)^2 \frac{e^{-4\nu\,\mathrm{arctan}(1/\nu)}}{1-e^{-2\pi\nu}}\,, \tag{1.38}$$

where $\nu = \alpha Z/v$ is the Sommerfeld parameter (v the initial electron velocity). This formula can lead to rather tedious numerical calculations if a sum over many n has to be performed. By comparing the results of the Kramers approximation with the more precise one obtained with the Stobbe formula, differences in the cross sections for lower n states appear. A correction (the so-called *Gaunt* factors, Eq. (1.58)) of about 21% has to be subtracted in the case of recombination into states with the principal quantum number $n = 1$, 12% for $n = 2$ and 9% for $n = 3$ [ABK90].

The RR cross section has its maximum at low electron energies and decreases smoothly with increasing electron energy. From Eq. (1.37), the ground state ($n = 1$) is inferred to be dominant. Figure 1.9 shows cross sections of Hg ions obtained by means of Eq. (1.37) for RR into different n states.

1.2.3 Quantum mechanical interference between RR and DR

So far, we have discussed RR and DR under the assumption that they are completely independent. However, it has been shown that such a description is not complete in a rigorous quantum-mechanical approach [JCH87]. In fact, RR and DR in the photorecombination (PR) process have to be treated as coherent interfering components of an electromagnetic transition occurring between the initial and final atomic states. The amplitudes of the direct recombination accompanying emission of a photon and of the indirect process can in principle interfere as the initial and final states are the same.

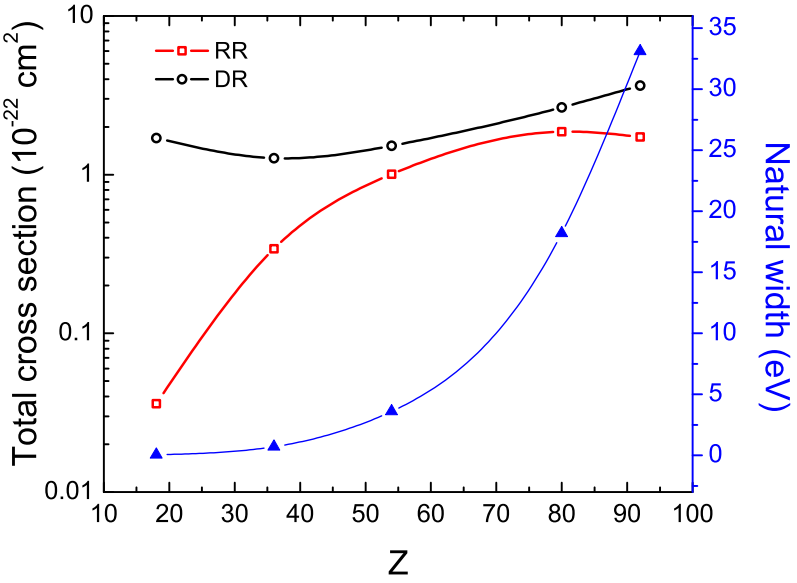

Figure 1.10: Total cross section [Har05] for the radiative (red squares) and dielectronic (black circles) recombination for the $1s(2s_{1/2}2p_{1/2})_0$ excited states as a function of Z. For the calculation of averaged DR cross sections $\sigma_{DR} = S_d/\Gamma$ a rough estimate was taken for the experimental width Γ. On the right scale is shown the Z^4 dependency of the natural width of these resonances (blue triangles).

For low-Z ions, RR is in comparison with DR a weak process with cross sections of the order of 10^{-23} cm^2, whereas DR is a few orders of magnitude stronger, resulting in a large difference in the magnitude of the amplitudes, thus making interference effects usually negligibly small. For highly charged ions (HCI), as shown in Fig. 1.10, stronger interference effects are expected, since the two amplitudes become comparable in magnitude due to the fact that the cross section for RR scales with Z^2, while the one for DR is independent of Z. Moreover, the Z^4 scaling of the natural width of the DR resonances provides a larger overlap with the RR, and, therefore, an enhancement of the interference effect (see Fig. 1.10).

A few theoretical contributions dealing with this issue appeared in the last decade, and in one of the few existing calculations of quantum interference, Badnell and Pindzola [BP92] predicted a significant increase of the interference effect between RR and DR at KLL resonances of HCI [PBG92].

The projection operator formalism

Two main approaches have been developed to provide a unified description of the PR process. The first one is based on a radiative modification of the close-coupling equations in existing R-matrix codes [GBS02]. This method provides highly accurate cross sections [WE47]. The basis of the R-matrix is constructed from the real, pseudo and continuum orbitals which are included to describe the motion of the free electron. A limited number of coupled channels can be taken into account in the calculations. The second approach is based on the so-called projection-operator and resolvent-operator methods [JCH87]. Here, the transition operator describing the electron-ion PR process can be expressed as a sum of the direct (RR) process and the indirect resonant term due to the DR contribution. In the following, this second approach will be explained in more detail.

Under the absence of collisional and radiative decoherence and relaxation processes, the projection-operator and resolvent-operator formulation, as used by Jacobs, Cooper and Haan [JCH87] and by Badnell and Pindzola [BP92] to obtain PR cross sections for uranium ions, provides a unified description of the radiative and dielectronic recombination in the Hilbert-space. The total Hamiltonian describing the PR is the sum of the electronic part H_e, the radiation field H_r and the atom-field interaction term H_{er}, and is given by

$$H = H^0 + V = H_e + H_r + H_{er} \; . \tag{1.39}$$

This Hamiltonian can be separated by applying the so-called Feshbach projection operators P, Q and R to the wave function. P projects onto the initial subspace i of the electron continuum, $|i\vec{p}\rangle$ ($\vec{p}$ is the linear momentum of the incident electron), Q projects onto the subspace of the closed-channel, autoionizing, (doubly) excited state $|d\rangle$ and R projects onto the final subspace of photon continua $|f\omega_{\vec{k}}\rangle$ ($\omega_{\vec{k}}$ represents the emitted photon with energy $\hbar\omega_{\vec{k}}$ and momentum $\hbar\vec{k}$). These operators provide a precise description of the autoionization process for the individual parts of the Hilbert space and have to fulfill some orthogonality and commutation rules [HJ89, ZGS97].

The transition operator $T(z)$ describing the photorecombination process can be described as a function of a complex energy variable z (see details in [ZGS97] and references therein), as

$$T(z) = V + VG(z)V . \tag{1.40}$$

Here, $G(z) = [z-H]^{-1}$ is the resolvent Green operator. The total PR cross section $\sigma_{if}^{PR}(E_e)$ leading to the transition $i \to f$ as a function of the incident electron energy E_e, integrated over all directions $\Omega_{\vec{k}}$ of the outgoing photon has the form

$$\sigma_{if}^{PR}(E_e) = \frac{2\pi}{\hbar} \frac{\int d\Omega_{\vec{k}} \left| \left\langle f\omega_{\vec{k}} \left| RTP \right| i\vec{p} \right\rangle \right|^2}{F(\vec{p})} \rho_{\vec{k}} , \tag{1.41}$$

where $\rho_{\vec{k}}$ is the final state density of the emitted photon per unit of energy and solid angle intervals and $F(\vec{p})$ is the incoming electron flux. The transition operator $T(z)$ can be represented in terms of two contributions, the RR and the DR term, by using projection operators RTP [HJ89]. Therefore, the cross section for the PR process, which involves the square of the matrix element $RT(z)P$ yields [BJO 04]:

$$\sigma_{if}^{PR}(E_e) = \sigma_{if}^{RR}(E_e) + \sigma_{idf}^{DR}(E_e) + \sigma_{idf}^{int}(E_e) , \tag{1.42}$$

where $\sigma_{idf}^{int}(E_e)$ represents the interference term. Haan and Jacobs [HJ89] developed a non-perturbative procedure for obtaining the matrix elements of the projection $RT(z)P$ of the transition operator. Applying this procedure to complex atomic systems implies the inversion of very large matrices. Alternatively, by means of a perturbative expansion in powers of V [ZGS97], problems with limited number of discrete and continuum states can be treated. $RT(z)P$ might be approximated in the lowest order by introducing the projection $QG(z)Q$ of the propagator $G(z)$ onto the Q-subspace of the autoionizing states as

$$RT(z)P = RT^{RR}(z)P + RT^{DR}(z)P \cong \tag{1.43}$$

$$RVP + RVQ \frac{1}{Q\left[z - H^0 - VPG^0(z)PV - VRG^0(z)RV\right]} QVP .$$

In this lowest order approximation, one can extract the cross sections for DR and RR independently. It is noted that an additional interference term appears here which was neglected in the traditional independent resonances approximation.

RR, DR and interference cross sections

To calculate the cross sections, the states defined as $|i\rangle$, $|d\rangle$ and $|f\rangle$ have to be translated into the total angular momentum states with J_i, J_d and J_f, respectively. The magnetic quantum numbers of these atomic levels are consequently expressed as M_i, M_d and M_f. The state of the recombined electron is characterized by its orbital and total angular momenta (l and j), or by a new quantum number $\kappa = (l-j)(2j+1)$ [BJO 04]. Within this nomenclature one can more specifically represent the unperturbed eigenstates of the system as follows

$$\begin{aligned} |i\,\vec{p}\rangle &= |\gamma_i J_i, \vec{p}\,\kappa; J_d\rangle \ , \\ |d\rangle &= |\gamma_d J_d\rangle \ , \\ |f\vec{k}\rangle &= |\gamma_f J_f, \vec{k}\rangle \ . \end{aligned} \tag{1.44}$$

Here, γ represents a set of additional atomic quantum numbers not specified explicitly, which contains the magnetic m and the principal n quantum numbers. Continuum wave functions are normalized on the energy scale. Explicit expressions for the PR cross sections can be derived with these unperturbed states with the use of the corresponding projection operators [BJO 04, ZGS97].

i) Radiative recombination

In the lowest-order, the projected transition amplitude $RT(z)P$ is equal to RVP (1.43), which is essentially Hamiltonian H_{er} of interaction between the ion and the electromagnetic field. The RR cross section is given by the radiative transition between the initial state i and the final state f. Thus, it is obtained from Eqs. (1.41) and (1.43) by summing over the final degenerate magnetic substates and averaging over the initial degenerate magnetic states. In order to obtain the proper dimension of an area for the cross section, the transition amplitude is expressed in units of energy multiplied by the volume. The photon density $\rho_{\vec{k}}$ can be expressed as $\left(\hbar\omega_{\vec{k}}\right)^2/(2\pi\hbar c)^3$. By considering only the electric-dipole radiation and the energy-normalized electronic states in the continuum, the RR cross section is reduced to the following expression:

$$\sigma_{if}^{RR}(E_e) = \frac{1}{2(2J_i+1)}\frac{4\pi^2\hbar^2\omega_{\vec{k}}^3}{3c^2p^3}\sum_{\kappa}\sum_{J}\left|\left\langle \gamma_f J_f \left\| \vec{D} \right\| \gamma_i J_i, E_e\,\kappa; J\right\rangle\right|^2 . \tag{1.45}$$

Here, $\vec{D} = e\sum \vec{r}_j$ is the dipole moment operator, which expresses the reduced matrix elements of the many-electron electric dipole transition.

ii) Dielectronic recombination

In the resonant channel of the PR process, two projection operators ($RT^{DR}(z)\,P$ in Eq. (1.43)) have to be analyzed carefully. The interaction operator RVQ connects the levels d and f by spontaneous radiative decay. The second interaction operator QVP connects the intermediate level d and the electron continuum state i via autoionization, electron recombination and the electron-electron electrostatic interaction ($H_{es} = e\sum 1/r_{kl}$). In order to account for increased relativistic effects on the electron-electron interaction [MJ71], the Breit interaction has to be included in addition for heavy ions. Relativistic effects include retardation and the magnetic interaction of two relativistic electronic currents.

The transition amplitude $T^{DR}(z)$ for DR must be evaluated at $z = E + i\,\epsilon$, $\epsilon \to 0$, in most cases introducing the pole approximation [HJ89] for the resolvent operator.

The DR transition operator (1.43) can therefore be written as

$$T^{DR} = \sum_{M_d} \frac{H_{em}\,|\gamma_d J_d M_d\rangle\,\langle\gamma_d J_d M_d|\,H_{es}}{E - E_d + \frac{i\Gamma_d}{2}}\,, \tag{1.46}$$

$$\Gamma_d = \hbar\left(\sum_f A^r_{df} + \sum_i A^a_{di}\right)\,, \tag{1.47}$$

where Γ_d is the total width of the resonant state d in the absence of environment interactions between the radiative and autoionization decays. A^a_{di} is the autoionization rate from the resonant doubly excited state d to the non-resonant electron-continuum state i and is given by

$$A^a_{di} = \frac{2\pi}{\hbar}\frac{1}{2J_d+1}\sum_\kappa \left|\langle\gamma_i J_i, E_e\,\kappa; J\,\|H_{es}\|\,\gamma_d J_d\rangle\right|^2 \delta_{E_d, E_i+E_e}\,, \tag{1.48}$$

whereas A^r_{df} is the rate for radiative decay from the state d to the final state f given by

$$A^r_{df} = \frac{4e^2\omega^3}{3\hbar c^3}\frac{1}{2J_d+1}\left|\left\langle\gamma_f J_f\left\|\vec{D}\right\|\gamma_d J_d\right\rangle\right|^2 \delta_{E_d, E_f+\hbar\omega}\,. \tag{1.49}$$

In these equations, δ is the Kronecker delta function, which can be substituted by the Dirac delta function δ' when the electron continuum states are defined with periodic boundary conditions ($-i\pi\delta'(E-E') \rightarrow -i\pi\rho(E_e)\,\delta_{E,E'}$). The DR cross section is then given in terms of the reduced matrix elements for these two interaction Hamiltonians. By introducing standard expressions for the radiative decay and autoionization rates, this cross section is written in the following form

$$\sigma_{idf}^{DR}(E_e) = \frac{(2\pi\hbar)^3}{8\pi m E_e}\frac{(2J_d+1)}{2(2J_i+1)}A_{di}^{a}L_d(E_e)\,\omega_d\,, \tag{1.50}$$

with ω_d being the level-specific branching ratio for the $d \rightarrow f$ spontaneous transition (for the definition of L_d see Eq. (1.29)).

iii) Interference term

In order to analyze the interference term in the PR cross section, one has to take into account the phase relations in the calculation of the transition amplitudes for the RR and the DR processes, respectively. The interference term, from a level i to a level f via level d, is obtained using the lowest-order autoionization and radiative decay rates as well as the lowest-order DR cross section for a single electric-multipole (L) in the following form

$$\sigma_{idf}^{int}(E_e) = \sigma_{idf}^{DR}(E_e)\,\frac{4}{\hbar A_{di}^{a}}\mathbf{Re}\left\{\left[(E_i+E_e-E_d)+\frac{i\,\Gamma_d}{2}\right]\frac{1}{Q_{idf}}\right\}\,, \tag{1.51}$$

where Q_{idf} is the "dimensionless" multichannel Fano line-profile parameter defined as

$$\frac{1}{Q_{idf}} = \frac{\pi}{\sqrt{(2J_d+1)}}\frac{\sum_\kappa \left\langle \gamma_f J_f \left\| \vec{D} \right\| \gamma_i J_i, E_e\ \kappa; J_d \right\rangle \left\langle \gamma_i J_i, E_e\ \kappa; J \left\| H_{es} \right\| \gamma_d J_d \right\rangle}{\left\langle \gamma_f J_f \left\| \vec{D} \right\| \gamma_d J_d \right\rangle}\,. \tag{1.52}$$

An extended analysis of higher order electromagnetic-multipole contributions of Q_{idf} is given in ref. [ZGS97]. In that work Q_{idf} can have in addition to the real part given in Eq. (1.52) an imaginary part. Eq. (1.51) can finally be rewritten, because only the real part belongs to the interference term, as follows:

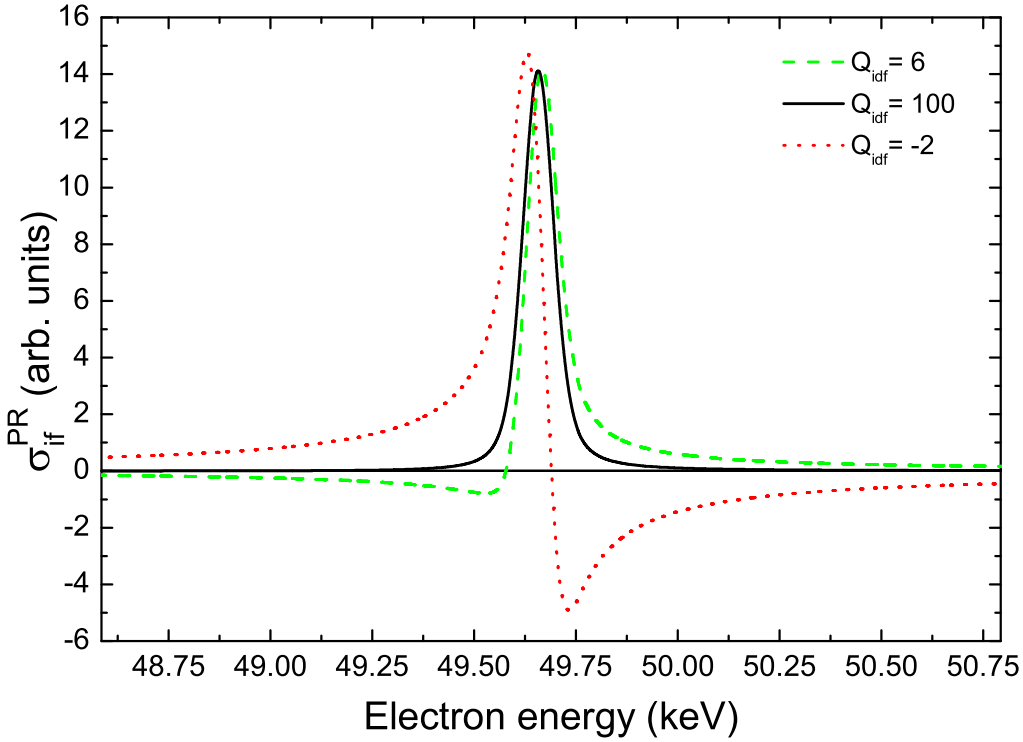

Figure 1.11: Calculated shape for a DR resonance in the $KL_{1/2}L_{3/2}$ region of boron-like mercury ions (Hg^{75+}) with different Fano factors Q_{idf} (convoluted with a Gaussian distribution of 70 eV FWHM). The fixed parameters are the natural width (35 eV) and the electron energy (49.657 keV). Generally, the asymmetry nearly disappears for values of the Fano factor higher than 30.

$$\sigma_{idf}^{int}(E_e) = \sigma_{idf}^{DR}(E_e)\,\frac{4}{\hbar A_{di}^{a}}\left[(E_i + E_e - E_d)\,\mathbf{Re}\left(\frac{1}{Q_{idf}}\right) - \frac{\Gamma_d}{2}\,\mathbf{Im}\left(\frac{1}{Q_{idf}}\right)\right]. \quad (1.53)$$

It is understood from Eq. (1.53) that, in the vicinity of a resonance, the cross section of the interference term results as a product of the linear function E_e, which changes sign at a resonance energy $(E_d - E_i)$, and the Lorentzian profile function characterizing the DR cross section. Therefore, the energy dependency results in asymmetric line profiles [Fan61]. It can also be noticed that the continuum-continuum coupling modifications are more significant and the resonance shape is most pronounced when the values of Q_{idf} are small. In particular, in heavy highly charged ions, for values of Q_{idf} being larger than $30 - 40$ the asymmetry nearly vanishes and the curve profiles emerge into symmetric Lorentzians. As an example, Fig. 1.11 illustrates how the shape of a KLL DR resonance ($Z = 80$) changes for different Fano factors Q_{idf} (for a fixed natural width and resonance energy).

Fano showed [Fan61, FC65] that the observed asymmetric resonance curves in the inelastic scattering cross sections of electrons by atoms are explained by taking into account the interference between transition amplitudes leading directly into the ionization continuum and those indirectly proceeding via a discrete autoionizing intermediate resonant state. He could reproduce the asymmetric resonance line shapes for the energy-dependent photoionization spectra around the resonances. Figure 1.12a shows the interference in electron inelastic scattering from helium atoms taken from his work. The larger resonance state in Fig. 1.12a corresponds to the inelastic scattering through the $2s2p\ ^1\mathrm{P}$ level of helium atoms. The fits to this resonance, convoluted with a Gaussian distribution to accounts for the experimental resolution, are shown for different natural linewidths in Fig. 1.12b.

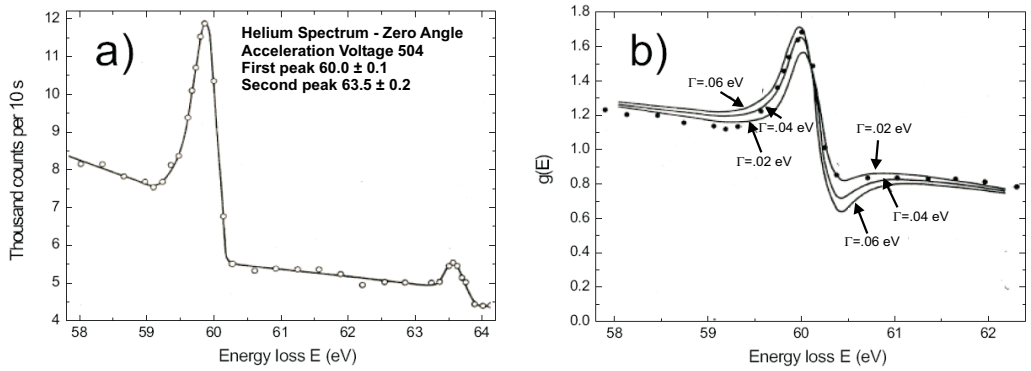

Figure 1.12: a) Experimental inelastic scattering of electrons from He atoms (open dots) in the Fano original work [Fan61]. The two peaks are due to the $2s2p$ resonance at low energy loss and the $2s3p$ or $3s2p$ level at higher energy loss. b) Detail of the fits to the $2s2p$ resonance in [Fan61] for different natural linewidths Γ.

The first signature for the interference between DR and RR processes in photorecombination in collisions of free electrons with highly charged, heavy ions (Fig. 1.13) was reported by Knapp for uranium ions ($U^{87+...90+}$) in the LLNL SuperEBIT [KBC 95] using a technique, very similar to the one presented here, but at lower resolution, and with poorer statistics. In addition, the photon energy resolution was not used to separate the photorecombination into the different charge states. Therefore, their Fano factors were determined only for the averaged charge state taking into account their respective DR strengths.

Considerable efforts have also been pursued at storage rings, where only the charge changing ions are detected, to observe the interference effect for ions in low charge states such as Sc^{3+} by Schippers [SKM 02]. In one experiment (Fig. 1.14), a small experimental evidence for an asymmetry of the $3p^5 3d^2\ (^3\mathrm{F})\ ^2\mathrm{F}$ resonance line shape was concluded. The low energy side of this resonance is blended with three

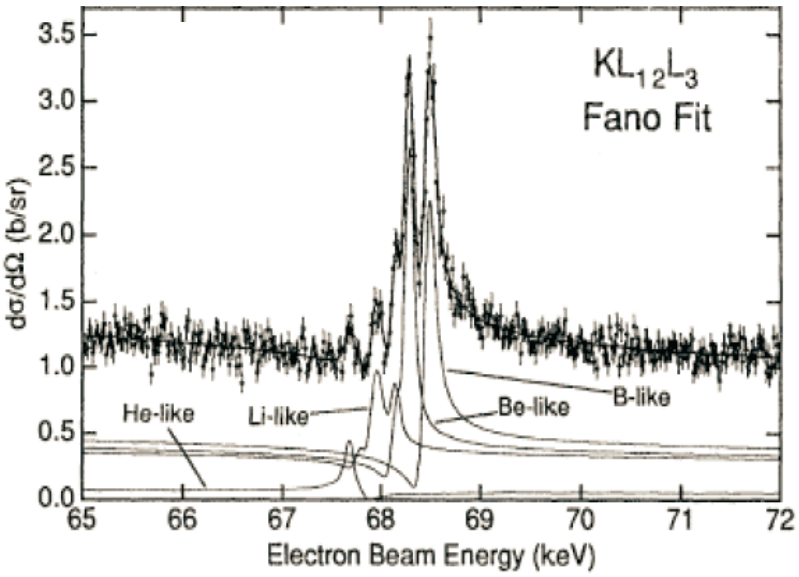

Figure 1.13: DR resonances in the $KL_{1/2}L_{3/2}$ region for highly charged uranium ions in collision with electrons [KBC 95].

close resonances, thus, making the observation of the interference difficult. The measured Fano factor for this structure resulted in 6.3 ± 1.8 which was strongly affected by the residual gas molecules. Here, by allowing a constant background as an additional free parameter, the Fano factor appeared to be 10.4 ± 4.1 (39%).

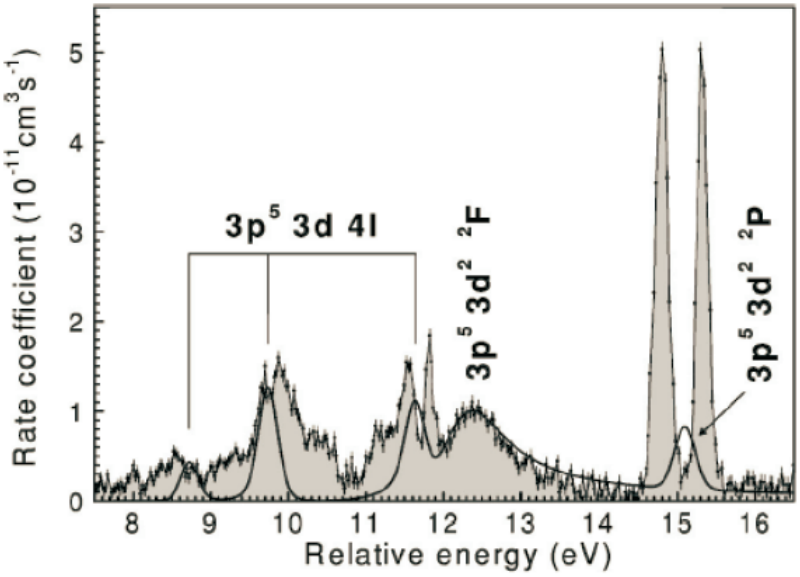

Figure 1.14: DR resonance line shape ($3p^5 3d^2(^3\mathrm{F})\ ^2\mathrm{F}$) in Sc^{3+} in collision with electrons [SKM 02].

1.3 Dynamic processes

Plasmas, in particular those at high temperatures, are characterized by the collisions taking place between their constituent particles. The Coulomb forces let these particles interact with each other on a long range scale. Excitation, ionization, charge exchange and recombination processes coexist and a certain degree of ionization is reached in equilibrium. The excited states can autoionize by emission of an electron or radiatively decay to lower states emitting one or more photons. In the following for completeness and for practical reasons when working with an EBIT a short description of the main electronic processes except from radiative and dielectronic recombination is given, namely electron or photon impact ionization and excitation as well as charge transfer.

1.3.1 Electron impact excitation and ionization

The most common processes involving highly charged ions in collisions with electrons are the *collisional excitation* (also called electron impact excitation), and *ionization*. There is extended literature covering both of these topics and sophisticated theoretical calculations are at hand. Here, for short overview, only the scaling features of electron impact excitation and ionization are briefly described and widely-used semi-empirical formulas are provided for the estimation of the respective cross sections.

The excitation process takes place if the kinetic energy E_e of the incident electron is larger than the threshold energy to excite an ion from level n to level n' (1.54). The excited ion is stabilized usually by emitting a photon with specific energy, by photon cascades (1.55), or by Auger processes.

$$\begin{aligned} \textit{Excitation}: \quad A^{q+} + e^- \quad &\rightarrow \left[A^{q+}\right]^* + e^- \\ &\rightarrow A^{q+} + \hbar\omega\,. \end{aligned} \tag{1.54}$$

A^{q+} indicates an ion q-times ionized and the asterisk denotes the excited state. The excitation can also be resonant (*resonant excitation*) if the incident electron, after exciting one of the inner-shell electrons, is captured generally forming an intermediate doubly-excited state. This state decays preferentially by Auger electron emission for light ions. If the doubly excited state decays by emission of a photon, the process is called *dielectronic recombination* (see Eq. (1.23)), as described previously.

$$\begin{aligned} \textit{Resonant excitation}: \quad A^{q+} + e^- \quad &\rightarrow \left[A^{(q-1)+}\right]^{**} \\ &\rightarrow \left[A^{q+}\right]^{*} + e^- \\ &\rightarrow A^{(q-1)+} + \hbar\omega \end{aligned} \tag{1.55}$$

For positive ions the dipole excitation cross sections is approximated by the Bethe formula,

$$\sigma_{ex} \approx \frac{A}{E_e} + B\frac{\ln E_e}{E_e}\,, \quad E_e \gg E_{n,n'}\,, \tag{1.56}$$

where A and B are constants, and $E_{n,n'}$ the transition energy. The so-called Bethe constant B is associated with the dipole oscillator strength. The empirical Van Regemorter formula [FRB 97] provides also a good estimate of excitation cross sections by electron impact. The cross section for the allowed dipole $n \rightarrow n'$ transitions is given there as a function of x, the ratio between the kinetic energy of the incoming electron and $E_{n,n'}$ ($x = E_e/E_{n,n'}$):

$$\sigma_{ex}^{VR}(x)[cm^2] = 2.36 \times 10^{-13} \frac{1}{E_{n,n'}^{\,2}} \frac{G(x)}{x} f_{n,n'}\,, \tag{1.57}$$

where $f_{n,n'}$ is the absorption oscillator strength and $G(x)$ the effective Gaunt factor. An empirical approximation for the Gaunt factor as a function of x is given in [FRB 97] as

$$G(x) = 0.349\ \ln(x) + 0.0988 + 0.455\, x^{-1}\,. \tag{1.58}$$

Experiments based on the measurements of electron impact excitation cross sections are performed with crossed-beam (high-energy) or merged-beam (low-energy) methods. As the effective ion target densities are extremely low (effectively less than 10^{-11} Torr), sophisticated techniques are necessary to extract the weak signal from the much larger background. Here, absolute excitation cross sections have been measured mainly for the resonance $s-p$ transitions in low charged ions such as C^{3+}, N^{4+}, Al^{3+}, Si^{3+} or Ar^{7+}. The observed cross sections decrease with increasing the ion nuclear charge Z, following roughly a $\sigma \propto Z^{-4}$ law.

An EBIT can also be used for these experiments by observing the photons emitted by the excited trapped ions. To obtain absolute cross sections, one can normalize the photon yield to that one observed for the radiative recombination process (see 1.2.2) [KMS 93].

In the case of resonant excitation, the doubly-excited state decays predominantly via autoionization (1.56) in low-charged ions, while radiative decay (1.56) becomes the dominant channel for highly charged ions.

The *direct ionization* process takes place if E_e exceeds the binding energy or ionization potential I_p of the target electron. The sum of the energies of the two scattered electrons is equal to the kinetic energy of the incoming electron minus the binding energy of the bound electron, thus,

$$\begin{aligned} \textit{Direct ionization}: \quad A^{q+} + e^-(E_e) \quad &\rightarrow A^{(q+1)+} + e^-(E_1) + e^-(E_2)\,, \\ &E_e - I_p = E_1 + E_2\,. \end{aligned} \tag{1.59}$$

Electron impact ionization is used to breed high charge states of ions in various ion sources including an EBIT. An often used expression for calculating the ionization cross sections for positive ions is the semi-empirical Lotz formula:

$$\sigma_i^L[cm^2] = 4.49 \times 10^{-14} \frac{N}{I_p^2} \frac{\ln(u+1)}{u+1}\,, \qquad u = E_e/I_p - 1\,, \tag{1.60}$$

where N is the number of equivalent electrons in the same shell. This formula is known to be well suited for few-electron ion systems. Nevertheless, it can be used for estimations of cross sections for most cases with an accuracy within about a factor of 2 or 3.

Using crossed-beam methods, and later storage rings, experiments on Cl^{6+}, Fe^{15+} or Se^{23+} have been carried out. Ionization cross sections for ions as highly charged as U^{91+} have been measured using an EBIT and the results were compared to various relativistic calculations [MEK94].

It should be noted that, in the ionization processes of multi-electron ions by electron impact, the indirect ionization process plays a significant role. When one of the inner-shell electrons is excited to a higher state or ionized into the continuum, a series of the autoionization cascades might follow. In particular at low energies this leads to an increase of the cross section which, in some cases, can be one order of magnitude. Moreover, considerable amount of double and multiple ionization might occur at high electron impact energies.

1.3.2 Photon impact

Two main processes can occur in ion-photon collisions, namely, *photoexcitation* and *photoionization* via absorption of the photon. In principle, at high photon energies, both processes can occur as well by Compton scattering of the photon but cross sections are extremely small and are not considered here. In the photoexcitation (1.61), the absorption of a photon results in excitation of a bound electron in the ion. In the photoionization process (1.62), a bound electron is ejected into the continuum.

$$Photoexcitation: \quad A^{q+} + \hbar\omega \rightarrow \left[A^{q+}\right]^* , \tag{1.61}$$

$$Photoionization: \quad A^{q+} + \hbar\omega \rightarrow A^{(q+1)+} + e^- . \tag{1.62}$$

There is a lack of experimental data for such cross sections on ions with a charge state higher than $q = 5$. The main reason for this is the difficulty in producing a dense target of highly charged ions to study their interactions with relative weak photon beams even at third generation synchrotrons.

Sophisticated calculations performed on the photoionization cross sections in the non-relativistic dipole approximation have shown a good agreement with experimental results at low photon energies. At high photon energies, the presence of a series of sharp resonances strongly affects the behavior of the photoionization cross sections. These resonances have their origin in the autoionization of intermediate doubly excited states.

The photoionization cross section is often estimated with the Kramers formula

$$\sigma_i^{ph}(n) = \frac{64\pi a_0^2 \alpha}{3\sqrt{3}n^2} \left(\frac{|E_0|}{|E_0| + E_e}\right)^3 , \qquad E_0 = Z^2 \mathbf{Ry}/n^2 , \tag{1.63}$$

where α is the fine structure constant and a_0 the Bohr radius of the ground state hydrogen atom. This formula contains the dependence on the various atomic parameters, the ion charge Z, the photon energy ω ($E_e = \hbar\omega - E_0$) and the principal quantum number n.

1.3.3 Charge exchange

The charge exchange is a process in which a bound electron is transfered from one atom or ion to another one. This process is particularly effective when slow neutral

atoms or molecules approach highly charged ions. Here, two or even more electrons can be exchanged in a single collision. The electrons occupy vacant states of the target ion. If these states are excited states, the ion subsequently decays to the ground state by a series of successive photon emission cascades:

$$\textit{Charge exchange}: \quad A^{q+} + B \rightarrow \left[A^{(q-1)+}\right]^* + B^+ \tag{1.64}$$

$$... \rightarrow A^{(q-1)+} + \hbar\omega + B^+ \,. \tag{1.65}$$

A simple classical model is useful to understand this mechanism. The predominant principal quantum number n_0 of the electron-transferred state depends mainly on the ion charge q and the binding energy I_p of the neutral target atom, but not on the nuclear charge Z:

$$n_0 = 3.7 \frac{q^{0.75}}{\sqrt{I_p[eV]}} \,. \tag{1.66}$$

With increasing collision energy, the electron is captured into lower laying n-states. Only at very high energies in deep laying n at highly charged ions with extremely small cross sections. As for the previous equation (1.66), an empirical formula for the electron capture cross section can be obtained within the "over-the-barrier" model (q $\geq$ 6) with an accuracy of $30 - 50$ % at collision velocities well below 1 $a.u. = 1/137 \cdot c$ by

$$\sigma_{CX}[cm^2] = 2.6 \times 10^{-13} \frac{q}{I_p^2[eV]} \,. \tag{1.67}$$

Although multiple electron capture may also occur in very highly charged ions, single electron capture always dominates.

Chapter 2

Experimental setup

The experiments on photorecombination of highly charged ions demand the use of sources of ions and electrons. Both conditions are met in an electron beam ion trap, which also allows one to collect the photons emitted in the process. The apparatus enables to vary the electron beam energy while maintaining good resolution and reproducibility in the range needed to access the deep laying shells of the ions under study. A slowly energy-varying electron beam is used for the simultaneous production of ions via ionization and for scanning the recombination resonances. The photorecombination is observed by detecting the x-rays which are emitted in the RR or during the relaxation of the (doubly) excited states formed in the DR. An appropriate data acquisition system allows to measure the energy and intensities of the photons and the energy of the interacting electron simultaneously as well as to determine DR and RR strengths as a function of the electron energy.

2.1 The Electron Beam Ion Trap

The basic principle of an electron beam ion trap (EBIT), depicted in Fig. 2.1, is to use the negative space charge of an electron beam to trap positive ions, and ionize them. The high density electron beam produced at high energies is therefore the most important component in an EBIT. Here, depending on the electron beam energy, ions can be prepared in all possible charge states.

The electron beam is generated in a Pierce-type electron gun, and its energy can be varied depending on the experimental requirements. Electrons are accelerated towards the positively biased trap region guided by a high magnetic field. After passing the trap region, the beam is decelerated to nearly its initial energy, allowed

to expand and dumped in the collector. The magnetic field is produced with two superconducting coils in a Helmholtz configuration. This field compresses the electron beam generating a large space charge potential, confining the ions in the radial direction. Several independently biased electrodes, the drift tubes, are used to trap the ions longitudinally and to manipulate or extract them. The trapped ions occupy a volume of cylindrical shape of 40 mm length and roughly 0.2 mm in diameter. Ionization takes place mainly inside the trap volume through successive collisions with the energetic electron beam. Figure 2.1 shows a conceptual picture of the EBIT, displaying the trapping potentials in the radial and longitudinal direction.

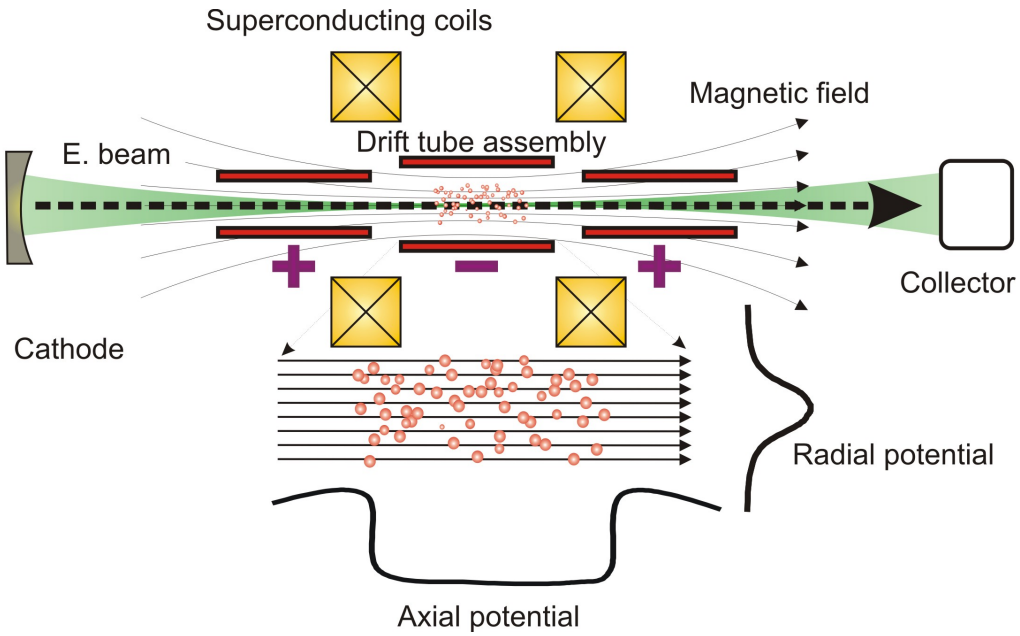

Figure 2.1: Principle of an electron beam ion trap. The electron beam is accelerated towards the drift tube region (three of nine shown here). It passes the drift tubes with nearly constant velocity, and is then decelerated before it arrives at the collector, to minimize there the heat deposition and x-ray production. The bold lines illustrate the radial potential produced by the space charge of the electron beam and the axial potential generated by the drift tubes bias voltage.

History

The underlying principle of the EBIT, namely the use of an electron beam to ionize and trap, has its origin in the modified electron beam ion source (EBIS). The EBIS was invented by Donets in 1965 in Dubna, who showed four years later the production of Au^{19+} [DIA69] using a vacuum tube inside an ordinary conducting solenoid. This device was improved and a few cryogenic versions called KRYON-I

to -III, were built. There, the drift tubes inside the superconductive solenoid were kept at 4.2 K. In particular, KRYON-I injected successfully bare C, N an O ions into the Dubna Synchrophasotron to boost the ion energy. KRYON-II was the first EBIS producing bare Ne, Ar, Kr and Xe ions [Don85]. Many EBIS were developed worldwide since then. The latest improvement of EBIS is required by the demand to provide intense ion beams for big accelerators and colliders like the RHIC at BNL or the LHC at CERN.

Even smaller EBIS were constructed to use them as a tool for atomic physics experiments in many laboratories world-wide. Litin *et al.* [LVS82], who had extensive experience with the Berkeley EBIS concluded that the long electron beam path tends to induce plasma instabilities and, therefore, a shorter electron beam path would be preferable. Instead of a solenoid, the use of a split pair magnet was proposed. The first EBIT with Helmholtz coils was constructed by Levine *et al.* [LMB 89] at the Lawrence Livermore National Laboratory (LLNL). This EBIT was later improved in order to reach higher electron energies up to 200 keV and electron beam currents as high as 200 mA (Super-EBIT). This machine yielded even small amounts of bare uranium ions (U^{92+}) [MEK94]. The original low energy LLNL design has been used to build two similar devices, located at the National Institute of Standards and Technology (NIST) [Gil97] and at the Oxford University [Sil94]. A further modified copy is the Berlin EBIT [BFF 97] and a new EBIT is at the Stockholm University [Uni05]. A high-energy EBIT (150 keV and 150 mA) was constructed at the University of Electro-Communication, Tokyo [CAI 96]. The EBIT at the Max-Planck-Institut für Kernphysik in Heidelberg [CDM 99] has a worldwide unique design and is one of the existing three high-energy EBITs. It is designed to enable the production of electron beam with energies up to 350 keV and currents as high as 750 mA, thus, reducing experimental acquisition times for high-energy experiments. Two more EBITs are under construction in Heidelberg: A high-current (5 A) EBIT which will be used for charge-breeding of radioactive isotopes at the ISAC facility at TRIUMF (Vancouver), and a second device for experiments at the VUV free electron laser (FEL) at the Tesla test facility Laboratory in Hamburg. Furthermore, quite recently, another high-energy EBIT designed for electron beam energies up to 200 keV is commissioned in the Institute of Modern Physics in Shanghai.

There are two principal differences between an EBIT and an EBIS. First, in an EBIS the magnetic field is provided by a single long and closed solenoid, while the short split coil Helmholtz configuration in an EBIT allows one to easily access the trap volume via several ports enabling all types of spectroscopy. The second difference is that the EBIT trap length is much shorter than that of an EBIS (roughly 1:25). A shorter trap helps to reduce plasma instabilities. The longer trap in an EBIS

can produce, therefore, a higher flux of ions. On the other hand, the main purpose of an EBIT is to *trap* ions for spectroscopy. The higher electron beam compression in an EBIT and optimized evaporative cooling results in faster ionization as well as higher interaction rates with the electron beam.

2.1.1 The Heidelberg EBIT

The Heidelberg EBIT design and construction took place at the Freiburg-University in 1998, and after two years of operation the machine was moved to the Max-Planck-Institut für Kernphysik in July 2001. The main difference to other EBITs is its horizontal arrangement, which has the advantage of simpler ion extraction and transfer to external experiments. In addition, a better thermal shielding reduces the liquid helium consumption. The liquid helium tank (4 K) is surrounded by two thermal shields (at 20 K and 50 K, cooled with a separate cryogenic system) which also provide additional pumping. In fact, while EBIT-II at LLNL has been reported to have a boil-off of liquid helium of 5 l/h, in the Heidelberg EBIT this has been reduced by a factor of 25 (0.2 l/h), thus significantly reducing the running costs. The magnetic field strength can be varied in the range from 3 T to up to 9 T. This strong field compresses the electron beam down to below 50 μm diameter, bringing the electron beam density to values as high as $\approx$ 12000 A/cm^2. The excellent vacuum conditions (10^{-13} Torr) minimize the losses of the trapped ions by charge-exchange. Due to the electron beam properties, namely high energy and high current, a broad variety of ion charge states (Hg^{78+}, W^{74+}, Xe^{54+}, Kr^{36+}, Ge^{30+},...) have already been produced.

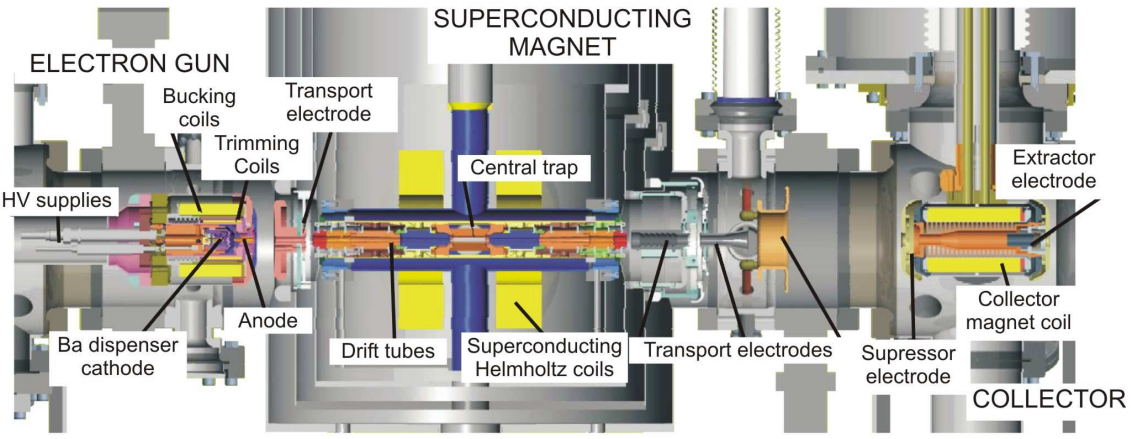

Figure 2.2: Structural picture of the Heidelberg EBIT.

Stable electron beams with an energy up to 100 keV as well as high current beams (up to 535 mA) have been achieved so far. After mass-to-charge ratio selection a variety of ion species (Ne^{10+}, Ar^{18+}, Kr^{34+}, Xe^{44+}, U^{64+}) have been extracted from the trap forming low-energetic beams with typical energies of 10 keV/q. These ions have been used for atomic collision experiments in a reaction microscope [UMD 03], carried out with the cold target recoil ion momentum spectroscopy (COLTRIMS).

In the following a detailed description of the main parts of the Heidelberg EBIT, as the electron gun, the drift tube assembly, the collector and the gas or ion injection is given.

The Electron Gun

A schematic picture of the electron gun shown in Fig. 2.3 displays the assembly of its various electrodes (anode, cathode, focus). The *cathode* of the electron gun has a Pierce geometry and, thus, a spherical-concave shape with a diameter of 3 mm and a concave radius of 5 mm. The cathode is made of a porous tungsten matrix impregnated with barium. Due to the diffusion of the barium through the tungsten matrix to the cathode surface, the emitting layer, which has a low work function ($\Phi_{W,Ba}$ = 2.0 eV) is constantly regenerated. By means of a tungsten filament, the cathode (indirect heating) is brought to temperatures of around 1100 °C.

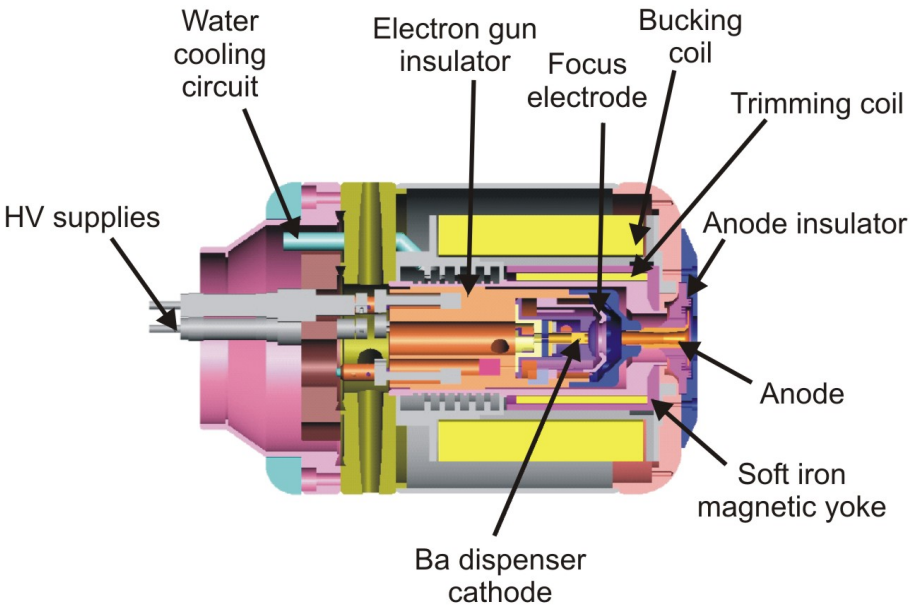

Figure 2.3: Electron gun assembly.

The *focus electrode* controls the emission current and compensates the edge effects

of the cathode field. The *anode* electrode also generates an extraction field for the electrons emitted from the cathode. The combination of these two electrodes determines the beam intensity and affects its focusing.

The cathode and the focus electrode are surrounded by a soft iron shield in order to reduce any influence of the EBIT magnetic field on the emitted electron beam since the residual magnetic field at the cathode surface B_c is critical with respect to minimize the beam radius [Her58] (see section 2.3). Two solenoidal coils surround the electron gun; the so-called *bucking coil*, which cancels the residual magnetic field, and the *trimming coil*, which provides better focusing of the electron beam.

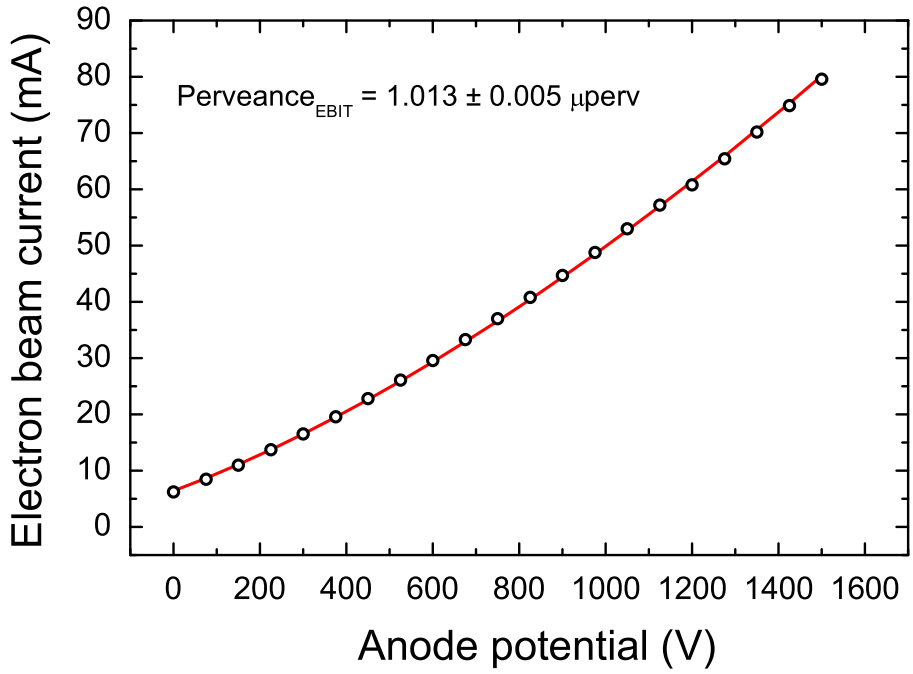

Figure 2.4: The measured perveance of the Heidelberg EBIT electron gun showing the electron beam current as a function of the voltage applied to the focus electrode [Roh05].

Electron guns are commonly characterized by the so-called perveance P, defined as $P = I/V_{cathode}^{3/2}$, where I is the electron beam current (A) and $V_{cathode}$ the voltage (V) applied between the cathode and anode. As displayed in Fig. 2.4, the Heidelberg EBIT gun has a perveance of 1 μperv (1 perv = 1 A/V$^{3/2}$). For comparison, the Super-EBIT gun reaches a perveance of 0.6 μperv [Wid98] while the Tokyo EBIT gun has been reported to achieve about 0.4 μperv [WAC 97]. The maximum voltage on the electron gun platform is expected to be 350 keV. Therefore, the total electron energy to be reached is about 370 keV in the ionization region (20 kV) which is sufficiently high to produce U^{92+} ions.

The Ion Trap

The trap region consists of nine electrodes (drift tubes) made of high purity copper. These electrodes have a cylindrical shape, with a central bore whose radius decreases towards the direction of the central trapping region (see Fig. 2.5). They can be biased independently, thus allowing for different trap configurations (see Fig. 2.2) with a total trap length varying from 40 mm to 200 mm. Accordingly, such a geometry allows the setting of appropriate conditions, to use the EBIT either as an ion trap for spectroscopy (short trap) or as an ion source (long trap). The central drift tube or trapping electrode (DT9 in Fig. 2.5) has an inner diameter of 10 mm. The whole set of drift tubes is biased at positive voltages up to $\approx$ 20 kV.

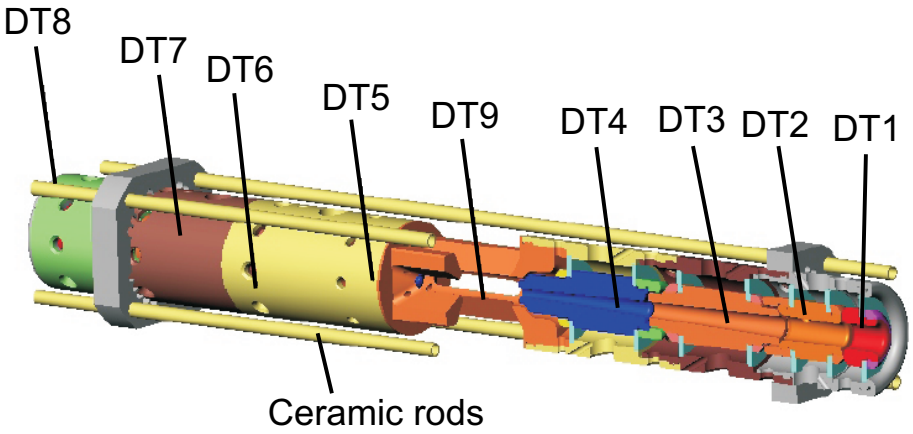

Figure 2.5: Assembly of the nine drift tubes.

Two superconducting coils in a Helmholtz configuration are located around the drift tubes, generating a field of 8 T at a current of 76.24 A (4.2 K). Higher magnetic fields (9 T) are produced by cooling the system down to 2.2 K with a Lambda refrigerator. The central drift tube has four elongated apertures allowing optical access to the trapped ions. The vacuum chamber has two horizontal ports located at a distance of 300 mm from the trap center. On one of these ports, under normal running conditions, a set of optical lenses for visible spectroscopy is mounted, while the opposite port has a beryllium window of 250 μm for x-ray spectroscopy. The x-rays observed through this port need to pass two more beryllium foils located in the thermal shields in order to separate the vacuum of the cryostat operating at different temperatures. A third port is conventionally used for the external atom injection. The fourth aperture port is placed on top of the helium tank at about 1200 mm distance from the trap center and is planned to be used for inserting an x-ray detector.

The Electron Collector

After passing through the drift tubes the electrons are decelerated to 1.5 keV energy or even less. Inside the collector (Fig. 2.6) the electron beam is allowed to expand, since the residual magnetic field of the superconducting magnet at that place is compensated by a magnetic coil surrounding the collector electrode. The defocused beam is dumped onto the inner wall of the collector electrode. The *suppressor electrode* at the entrance of the collector, biased negatively with respect to the collector, prevents secondary electrons produced in the collector walls from escaping the collector. Both the collector current and the suppressor current are regularly monitored to check the beam tuning. The *extractor electrode* located at the exit of the collector is biased to a negative voltage with respect to the cathode, to make sure that no electrons can pass the collector. Moreover, as indicated by its name, the extractor electrode is used to separate the ions coming from the trap from the electrons in the beam.

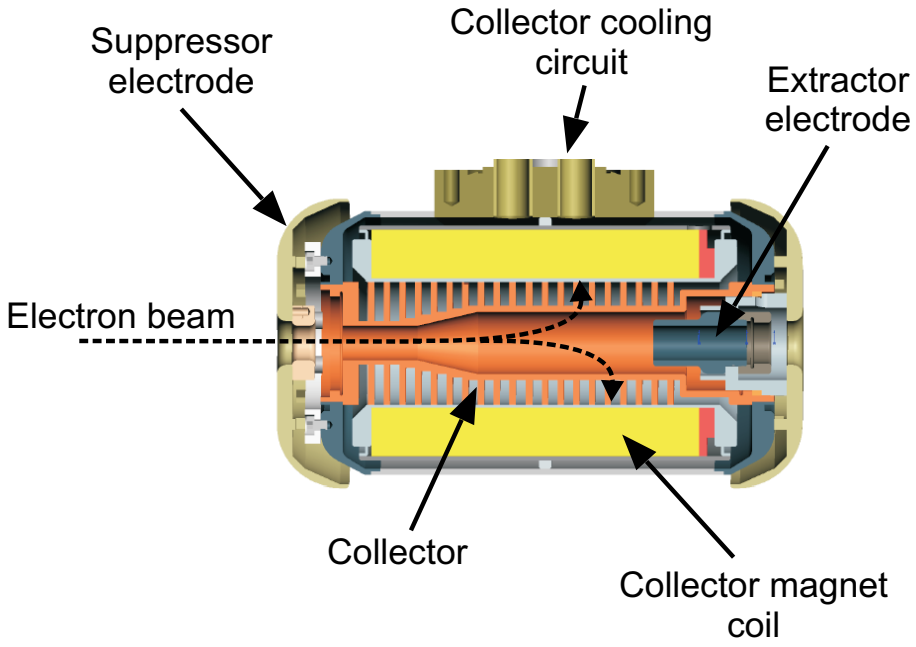

Figure 2.6: Cross section of the electron collector.

Ion and gas injection

In order to load the trap with the desired element, two types of injection systems are available at the Heidelberg EBIT: a *gas injector* and a *laser ion source* (LIS) for solid targets.

The gas injector delivers a neutral, collimated atomic beam to the trap region through multiple differential pumping stages (see Fig. 2.7). Elements or molecules which can be brought into the gas phase (Ne, Ar, Kr, Xe, Cl_2, UF_6, Hg, Bi,...) can be injected in this way. The input of a needle valve is connected to the gas supply. The gas pressure in the first stage is about 10^{-6} Torr, while at the second stage it is reduced to 10^{-9} Torr (monitored with an ionization gauge). By using slits at the various differential pumping stages, a slit-shaped atomic beam is formed, which overlaps with the electron beam in the central trap region. The final pressure in the ionization region is reduced by a few orders of magnitude (estimated value of 10^{-13} Torr). The density of neutral atoms injected into the trap is assumed to be proportional to the pressure measured in the second stage of the injector.

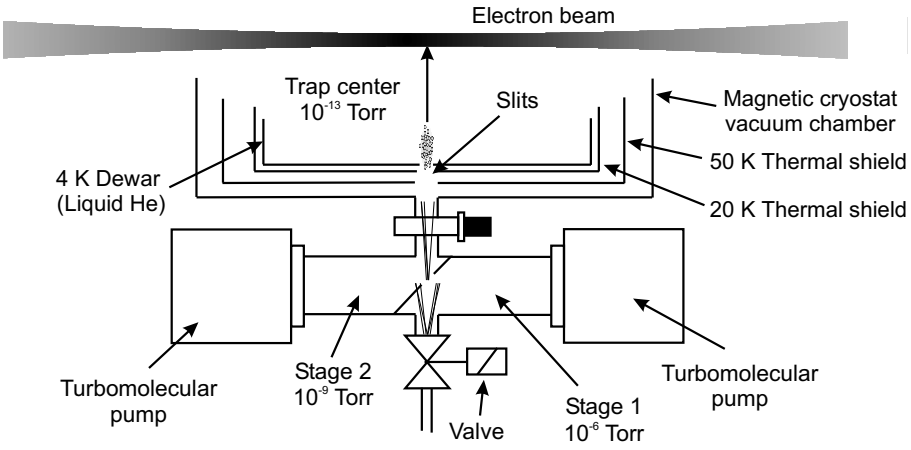

Figure 2.7: The two-stage differentially pumped gas injection system.

The laser ion source (Fig. 2.8) is located behind the electron collector. This source uses a plasma generated by focussing a pulsed laser of a few mJ and 9 ns pulse duration onto a solid target (10^8-10^9 W/cm^2). The plasma expands from the solid target surface. A beam consisting mostly of singly charged ions is extracted from the plasma by applying short high-voltage pulses between two grids, when the plasma in its expansion is located in between them. Thus, electrons are separated from the ions, which are finally accelerated into the EBIT. By modulating the voltages applied to the trap electrodes, the injected ions are allowed to enter the central drift tube and then trapped longitudinally (for details see [MTW 03]). The LIS has been used for the injection of ions from solid materials such as Ge, Cu, Al and Pb. The estimated number of ions produced (on the target surface) is approximately 10^{14} per Joule of the laser power.

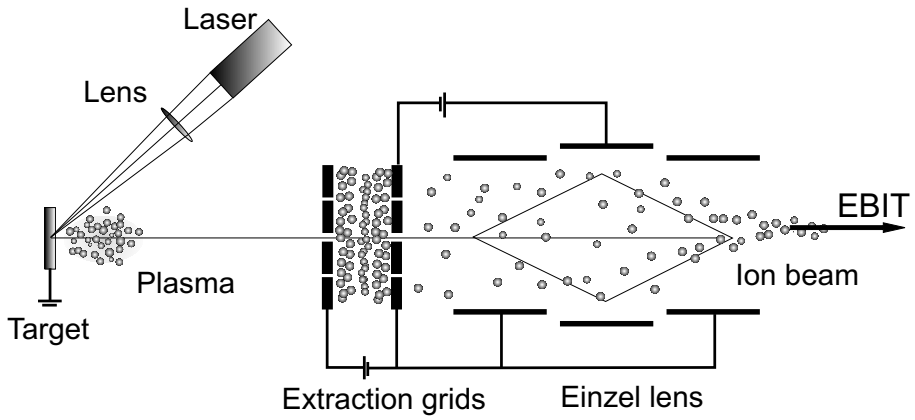

Figure 2.8: The laser ion source for solid targets.

Operation

For the proper operation of the EBIT it is mandatory to maintain very clean conditions using UHV and XHV technology. The vacuum pumping system consists of high compression (ratio up to 10^9 for N_2, 10^4 for H_2) turbomolecular pumps. To enhance the compression ratio for H_2, each large turbo pump (pumping speed 300 l/s) is backed by a small turbo pump (70 l/s) in the forevacuum line. Diaphragm pumps and scroll pumps are used for oil-free roughing. To effectively pump the electron gun and collector chamber region, non-evaporative getter (NEG) modules are mounted in addition. By far, the highest pumping speed is obtained by the two large coaxial thermal shields, operating at 50 K and 16 K, respectively, and by the liquid helium tank at 4.2 K. The different vacuum regions separated by the thermal shields are connected through narrow gaps and labyrinthic structures, to maintain pressure differentials as large as possible. The only vacuum gauge mounted on the magnet dewar is located outside the 50 K shield. Its reading is therefore indicating the worst pressure in the whole system, which is typically in the range of 5×10^{-10} Torr to 2×10^{-9} Torr. The pressure values between the 50 K and the 16 K shields, inside the 4 K dewar, and finally in the central magnet bore become stepwise lower. Accurate pressure values in the trap region can not be given, but they are estimated from charge exchange rates to be in the 10^{-13} Torr regime.

The EBIT is mounted on a high-voltage platform which will allow in the near future to accelerate the extracted ion beam to energies of up to 350 keV/q. A separate platform (electron gun) supports the electron-gun which is connected through an insulated, high-voltage hollow coaxial line to the collector. A high voltage cage surrounds this platform. It also encloses a three-phase motor-generator system to

Table 2.1: Typical parameters of the Heidelberg EBIT.

Electron beam energy	100 keV
Electron beam current	$250 - 535$ mA
Electron beam radius	23 μm (calculated) at 150 mA and 50 keV
Trap length	$40 - 200$ mm
Vacuum	10^{-13} Torr (estimated)
Maximum magnetic field	8 T at 4.2 K; 9 T at 2.2 K

deliver AC power to the devices mounted on the electron gun platform. During high energy operation, this cage is closed for safety reasons. For experiments in which the kinetic electron energy needs to be known, a high precision voltage divider has been constructed (see its detailed description below) to measure the exact platform voltage. The voltages for the electron gun platform (negative) and the drift tube

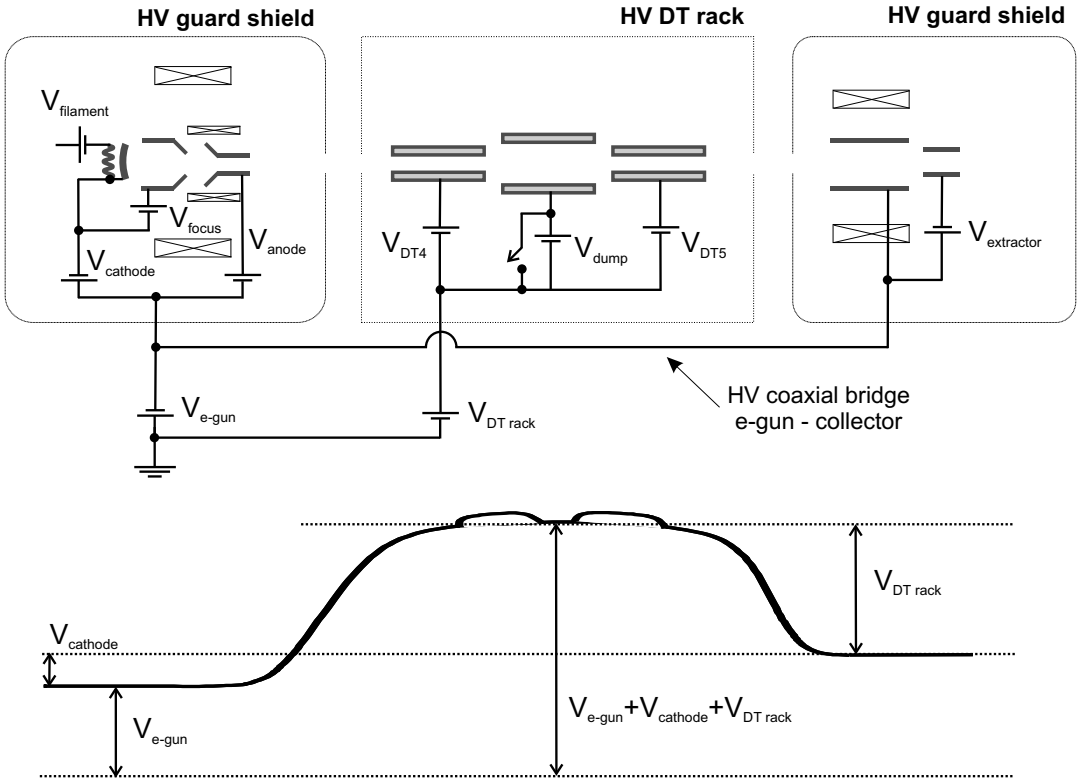

Figure 2.9: A schematic diagram of the different potentials applied to the elements of the Heidelberg EBIT. The lower curve indicates the potential distribution along the longitudinal axis.

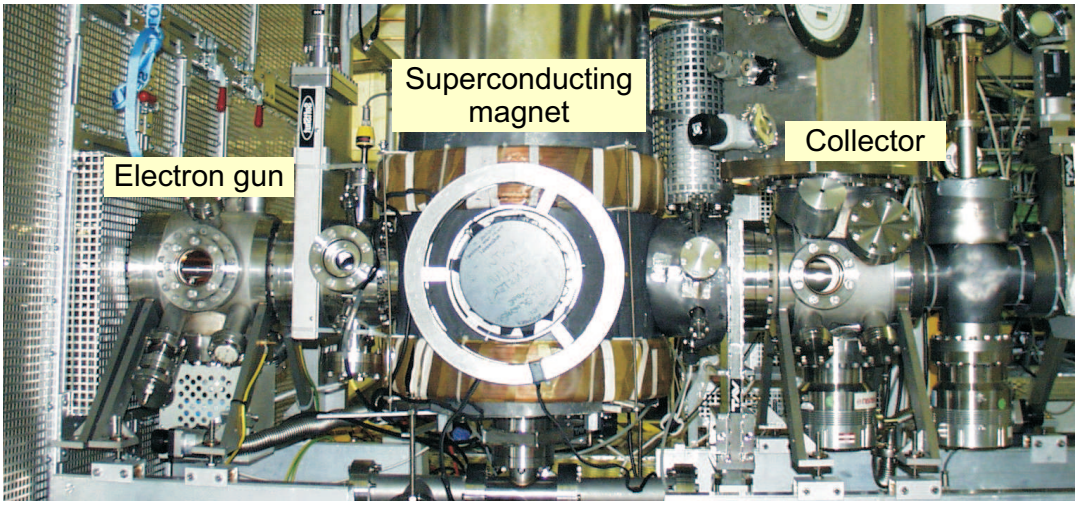

Figure 2.10: Photograph of the Heidelberg EBIT without lead radiation shields. The electron gun, collector and superconducting magnet chambers can be seen, respectively.

rack (positive) are fed in by different high voltage power supplies. Three Glassman power supplies (Models 60, 125 and 350 kV) and two fast Trek high voltage amplifiers (Models Trek 20/20 and Trek 30/20) of 20 and 30 kV capable of delivering up to 20 mA of current with a voltage scanning speed of 350 V/μs for fast ramping purposes are used.

The EBIT is equipped with an interlock system for person and machine safety reasons. Since all the vacuum levels and high voltage settings are integrated into this system, the EBIT can only be run under proper, well-defined conditions.

Thanks to the low helium consumption, the magnet dewar has to be filled with 50 l liquid helium only at intervals of approximately 10 days.

2.2 Modelling of the ion production and population

A quantitative description of the photorecombination process requires detailed knowledge of the charge balance, electron as well as ion densities, and other trap parameters. In order to understand the ion charge evolution with time and its spatial distribution in the trap region, a system of rate equations describing the collision processes has to be solved. The individual relevant processes have already been discussed in sections 1.2 and 1.3. The charge state of a specific ion changes, in most of the cases, only in steps of single elementary charges, as single electron processes are assumed to be dominant, although multielectron processes (involving changes in

the final charge state of two or even more) are not negligible [ST98].

Rate equations for the evolution of charge states have been derived, for instance, in [PBD 91]. There are mainly two types of charge-changing processes: those due to interactions with the electron beam (recombination and ionization) and those due to collisions with the residual gas or actively injected neutrals (charge exchange). The processes occurring inside the electron beam have rates R that can be described in the form

$$R \equiv \frac{dN_q}{dt} = \pm \frac{J_e}{e} N_p \sigma_p(E_e) f(r_e, r_p)\,, \tag{2.1}$$

where N_q is the population of the ion of interest with charge q. The sign ($\pm$) indicates the creation or destruction of ions with charge q and thus, depends on the process. J_e is the electron beam current density and e the elementary charge. The index p indicates the specific charge changing reaction with its corresponding cross section σ_p. Here, we will consider only single ionization or electron capture, *i.e.* $p = q - 1$ and $p = q + 1$, *i.e.* excitation is neglected. Finally, $f(r_e, r_q)$ is the overlap factor between the electron beam and the ion species with the charge q. This factor is different for electron impact ionization (EI), radiative (RR) and dielectronic (DR) recombination on the one side and charge exchange on the other side. The production rates of ions with charge q under steady-state conditions, outside DR resonances considering single electron transitions only, are given [PBD 91] by EI and RR

$$R_q^{EI} = \frac{J_e}{e} N_{q-1} \sigma_{q-1}^{EI}(E_e) f(r_e, r_{q-1})\,, \tag{2.2}$$

$$R_q^{RR} = \frac{J_e}{e} N_{q+1} \sigma_{q+1}^{RR}(E_e) f(r_e, r_{q+1})\,. \tag{2.3}$$

These two processes are driven by the electrons and, thus, occur always within the electron beam. In contrast, ions can capture electrons by collisions with neutral gas atoms or molecules, which are injected for cooling purposes or due to the residual background, in the whole volume occupied by the trapped ion cloud. The rates for these charge exchange (CX) processes or electron capture (see Eq. (1.64) and its following discussion) are given by

$$R_q^{CX} = N_0 N_{q+1} \sigma_{q+1}^{CX} \overline{v}_{q+1}\,, \tag{2.4}$$

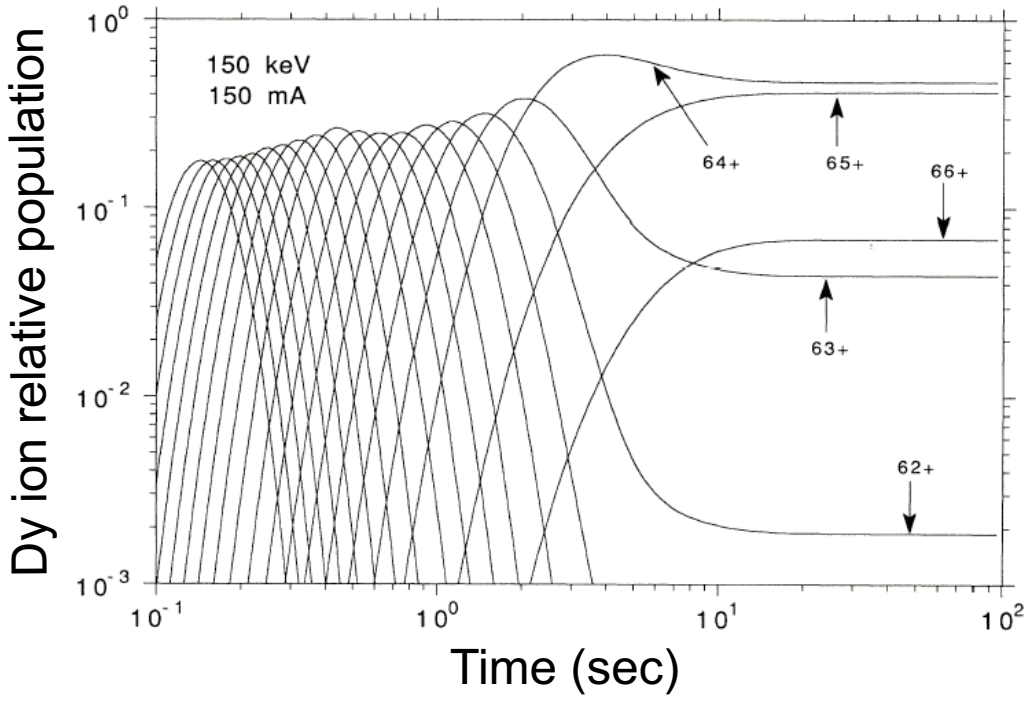

Figure 2.11: Evolution of dysprosium ($Z = 66$) ion charge states, taking into account only the electron impact ionization and the radiative recombination processes, respectively. The fixed parameters are $E_e = 150$ keV, $I_e = 150$ mA and $B = 3$ T. This result was obtained under the assumption that the target gas is injected only at time zero.

where N_0 is the neutral gas density and $\overline{v}_{q+1}$ the average velocity of ions in the trap. Here, the overlap factor $f(r_e, r_{q+1})$ has been set to one, since neutrals are assumed to cover the whole trap region. In addition, three more rates intrinsic to the trapping are usually taken into account, the axial and radial escape rate as well as the source rate, respectively. Ions with nuclear charge Z_q can escape from the electrostatic trap V if their energy is larger than eZ_qV. The source rate appears due to the continuous injection of neutral gas. The escape rates of highly charged ions can be estimated to be very small, and the source rate is typically small as well, usually having a low injection flow. Under such conditions, they can be neglected in approximate calculations.

For highly charged ions being axially strongly confined by the negative electron beam charge potential, we assume the overlap factor f to be equal to unity, *i.e.* all the ions of all the charge states are inside the electron beam. Then, the full rate equation for ions with charge q is given by (neglecting the DR contribution as DR occurs only at a very narrow energy range)

$$\begin{aligned}\frac{dN_q}{dt} &= \frac{J_e}{e}\left[N_{q-1}\sigma_{q-1}^{EI} + N_{q+1}\sigma_{q+1}^{RR} - N_q\sigma_q^{EI} - N_q\sigma_q^{RR}\right] \\ &\quad -N_0N_q\sigma_q^{CX}\overline{v}_q + N_0N_{q+1}\sigma_{q+1}^{CX}\overline{v}_{q+1}\,. \end{aligned} \tag{2.5}$$

In order to illustrate the time evolution of the different charge states present in a trap, Fig. 2.11 shows the evolution of dysprosium ions in the idealized case where the charge balance is determined only by the ionization and the radiative recombination processes under the assumption that no ions are lost during trapping [PBD 91]. The ion losses caused by the charge exchange of the background gas are assumed to be negligible.

Elastic as well as inelastic collisions with electrons from the beam not resulting in ionization events have nonetheless an indirect effect on the charge state balance in the trap, since the ion ensemble is heated with a rate given by

$$\frac{dkT_i}{dt} = f_{e,i}\frac{8\pi(J_e/e)q_i^2e^2\ln\Lambda_i}{3m_i}\,, \tag{2.6}$$

where kT_i is the ion temperature, $f_{e,i}$ the electron-ion overlap factor for a given ion charge q of specie i and mass m_i. Λ_i is the so-called Coulomb logarithm which describes the length scale over which the electron beam appears to be different from a smooth fluid. Since this heating depends on q_i^2, it is enhanced for the more highly charged ions. This heating would eventually lead to losses of trapped ions. Fortunately, a cooling technique can be applied, removing constantly energy from the ion cloud, namely, evaporative cooling. It was used in 1988 for the first time in an EBIT [LMH 88], and is based on the principle that all ions with different masses thermalize in the trap. Thus, lighter ions, share their kinetic energy with the heavier ones but, at same time experience lower effective trapping potentials due to their smaller maximum charge state, and, therefore evaporate more easily, thereby removing a sizable fraction of the heat input and cooling the heavier components.

For the particular case of dielectronic recombination measurements, the rate equation for the evolution of helium-like ions with the above mentioned approximations is given by:

$$\frac{dN_{He}}{dt} = \frac{J_e}{e}\left[N_{Li}\sigma_{Li}^{EI} - N_{He}\sigma_{He}^{RR} - N_{He}\sigma_{He}^{DR}\left(E_r\right)\right] - N_0N_{He}\sigma_{He}^{CX}\overline{v}_{He}\,, \tag{2.7}$$

where E_r indicates the resonant energy of the DR process. Note that, at $E \neq E_r$, $\sigma_{He}^{DR} \approx 0$.

Two methods have been mainly used to study the dielectronic recombination in an EBIT, depending on the particular interest, by using either fast or slow sweeping of the electron beam energy around the DR resonances. The most common one, dubbed "unperturbed scanning", consists of three phases [KMS 93]. First, the electron beam is set to high energy and current to generate the desired charge state distribution (*cooking* stage). Then, the electron beam energy is rapidly ramped down linearly to pass through the dielectronic recombination resonances (*probe*). Each ramping takes only a few milliseconds (< 50 ms) in order to avoid any perturbation of the ion charge distributions before bringing back the electron beam to the cooking stage. Finally, after repeated cooking-ramping cycles, there is a *dump* to avoid accumulation of heavy impurity ions and to clean the trap. Here, it is assumed that the DR does not change the charge state balance, and only a few percent of all trapped ions are recombined in each scan.

In the second, so-called "steady-state" method, which we use throughout the present experiments, the electron beam energy is scanned very slowly up and down through the resonances to keep a quasi-stationary charge balance between ionization and recombination at each energy. This has for our purposes the decisive advantage to allow for a far more accurate determination of the electron beam energy, since the strongly varying accelerating voltage is much better defined than with the other methode.

If one is interested in obtaining total DR cross sections, which was not the main intention of the present work, it is usually assumed that the charge distributions are similar to those found for the static case discussed above. The charge equilibrium equation ($dN_{He}/dt = 0$ in Eq. (2.7)) can be rewritten as

$$\frac{N_{Li}}{N_{He}} = \frac{1}{\sigma_{Li}^{EI}} \left[\left(\sigma_{He}^{DR}(E_r) + \sigma_{He}^{RR} \right) + N_0 \sigma_{He}^{CX} \frac{e\overline{v}}{J_e} \right] . \tag{2.8}$$

If the collisions of the ions with neutral atoms are negligible, the DR cross section for helium-like ions is expressed in terms of the ratio $\mathrm{N}_{Li}/\mathrm{N}_{He}$ by

$$\sigma_{He}^{DR}(E_r) = \sigma_{Li}^{EI} \frac{N_{Li}}{N_{He}} - B(E_e) , \tag{2.9}$$

where B is an off-resonance slowly varying background due to RR [ABC 90]. This approximation is used to obtain DR cross sections in combination with the corresponding electron-impact ionization cross sections of Li-like ions to fit the observed DR resonances [ZCU03, ZCG 04], taking into account the electron beam spread, the detector efficiency and other parameters.

2.3 Electron beam properties

In this section we describe in more detail general features of the electron beam, like its radius and its space charge potential, since these properties play the most important role in the production and trapping of the HCI and especially in determining the actual electron-ion interaction energy in the EBIT, the decisive point for any DR precision experiment.

2.3.1 Electron beam radius

In a first model, the Brillouin theorem [Bri45] describes a uniformly distributed electron beam propagating under the presence of an uniform axial magnetic field B. This theory assumes a laminar flow (the electron trajectories do not cross each other) and that the electrons are produced in a region of zero magnetic field. It does not take into account the initial thermal energy of the electrons. The electron beam radius r_B is then given in terms of the electron beam current I_e, the axial magnetic field B and the electron speed v_e as

$$r_B = \sqrt{\frac{2m_e I_e}{\pi\epsilon_0 v_e e B^2}}\,, \tag{2.10}$$

where m_e is the electron mass, e the elementary charge and ϵ_0 the permittivity of vacuum. Equation (2.10) can be reduced to the following form:

$$r_B\,[\mu m] = 829.91\frac{\sqrt{I_e}\,[A]}{B\,[T]\,E_e^{1/4}\,[eV]}\,. \tag{2.11}$$

In the non-relativistic regime, the radius is obtained using $v_e = \sqrt{\frac{2eE_e}{m_e}}$ with E_e being the electron energy. For relativistic electron beam energies the electron speed is given by:

$$v_e = c\sqrt{1-\left(\frac{E_e}{m_e c^2}+1\right)^{-2}}\,. \tag{2.12}$$

More rigorous calculations of the electron beam radius were performed by Herrmann [Her58], starting with a non-laminar electron beam of cylindrical shape and

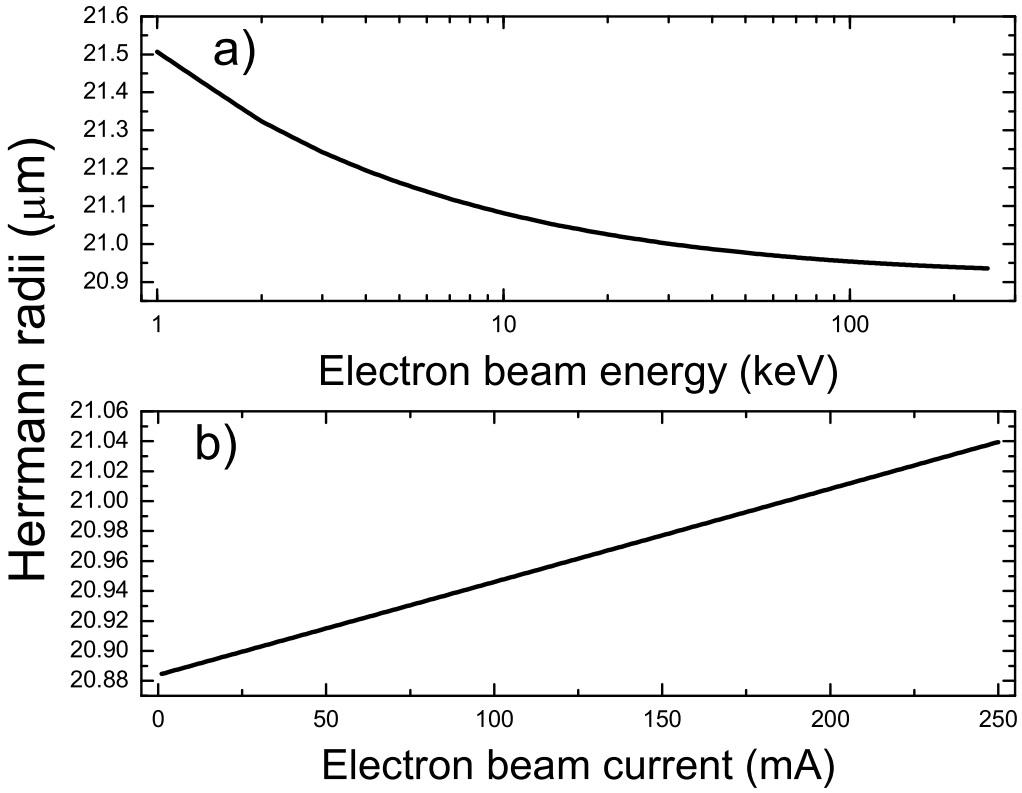

Figure 2.12: The Herrmann radii as a function of the electron beam current and energy, for the specific gun properties of the the Heidelberg EBIT.

taking into account the thermal motion of the electrons. Assuming that the axial velocity of the electrons is independent of the radial position, the effective electron beam radius is expressed in terms of the Brillouin radius r_B and a multiplicative factor containing contributions resulting from the properties of the cathode (radius r_c, magnetic field strength on its surface B_c and temperature T_c) and of the magnetic field used for compression. The Herrmann radius r_H defined as containing 80% of the total electron beam current then reads:

$$r_H = r_B \sqrt{\frac{1}{2} + \frac{1}{2}\sqrt{1 + 4\left(\frac{8 m_e k_B T_c r_c^2}{e^2 r_B^2 B^2} + \frac{B_c^2 r_c^4}{B^2 r_B^2}\right)}}, \tag{2.13}$$

where k_B is the Boltzmann constant. This equation is also valid in the relativistic regime by using Eq. (2.12) for v_e. Figure 2.12 illustrates the variation of the beam radius as a function of electron beam energy and current. Showing a smooth decrease of the radius with decreasing electron beam current and increasing energy.

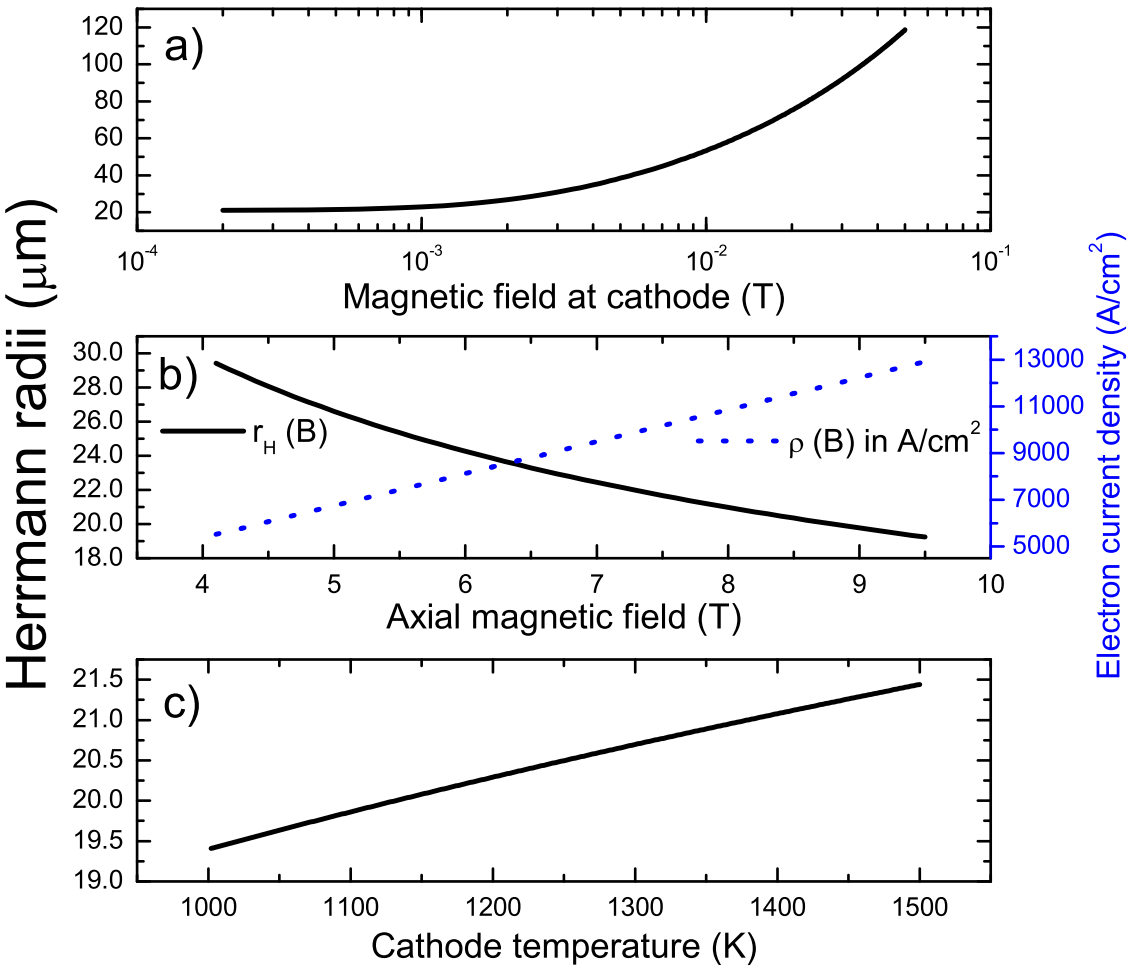

Figure 2.13: The Herrmann radii as a function of the magnetic field at the cathode surface (a), of the axial magnetic field inside the EBIT (b) and of the cathode temperature (c). Also indicated as the blue dotted line together with the scale on the right hand side (b) is the electron current density as a function of the axial magnetic field.

As it can be observed in Fig. 2.13a, the radius becomes considerably smaller when the residual magnetic field on the cathode is close to zero, and thus, should be minimized in the experiments. By setting T_c and B_c to zero, Eq. (2.13) becomes identical to the Brillouin formula Eq. (2.10). Figure 2.13b displays the dependence of the electron beam radius and electron current density on the magnetic field. Figure 2.13c shows the variation of the electron beam radius with the cathode temperature.

2.3.2 Negative space charge potential and the ion compensation

When resonance (or excitation) processes are being investigated, it is a requisite to precisely know the electron energy. Under conditions of an intense electron beam like in an EBIT, the radial space charge potential V_{sp} generated by the negative charge density of the electrons in the beam has to be taken into account as it reduces the effective interaction energy in relation to the actually applied acceleration voltage. In order to come to a quantitative notion of this space charge potential, we first have to assume an electron beam with a top-hat uniform profile distribution along the radial direction [Gil03] and identical radius r_e, *i.e.* a uniform magnetic field along the axial direction. The electron density ρ is written in terms of the electron beam current I_e by

$$\rho = \frac{I_e}{v_e}\frac{1}{A} = \frac{I_e}{\pi r_e^2 v_e} \,, \tag{2.14}$$

where v_e is the velocity of the electrons and A the cross section of the beam. Here, r_e is the Herrmann radius r_H calculated with Eq. (2.13) for a magnetic field realized in the center of the trap.

The Poisson differential equation,

$$\nabla^2 V_{sp} = -\frac{\rho}{\epsilon_0} \,, \tag{2.15}$$

is represented in cylindrical coordinates and the radial equation with $\nabla^2 = \frac{1}{r}\frac{\partial}{\partial r} r \frac{\partial}{\partial r}$ is solved in order to determine the electric field $E_{sp}(r)$ and the potential $V_{sp}(r)$ inside and outside the electron beam along the radial direction r. $E_{sp}(r)$ is found after a few steps taking into account the continuity of the derivative $\partial V_{sp}/\partial r$ at the boundary $r = r_e$ as

$$E_{sp}(r \leq r_e) = -\frac{I_e}{2\pi\epsilon_0 v_e}\frac{r}{r_e^2} \,, \tag{2.16}$$

$$E_{sp}(r \geq r_e) = -\frac{I_e}{2\pi\epsilon_0 v_e}\frac{1}{r} \,. \tag{2.17}$$

The space charge potential ($-\frac{d}{dr}V_{sp} = E_{sp}$) has to satisfy the conditions that the potential at the wall of the drift tube is zero ($V_{sp}(r = r_{dt}) = 0$) and that the

potential is again continuous at $r = r_e$. With these boundary conditions, the space charge potential is given by:

$$V_{sp}(r \leq r_e) = \frac{I_e}{4\pi\epsilon_0 v_e}\left[\left(\frac{r}{r_e}\right)^2 + \ln\left(\frac{r_e}{r_{dt}}\right)^2 - 1\right], \tag{2.18}$$

$$V_{sp}(r \geq r_e) = \frac{I_e}{2\pi\epsilon_0 v_e}\ln\left(\frac{r}{r_{dt}}\right). \tag{2.19}$$

Figure 2.14 shows the radial space charge potential obtained for an electron beam current and energy of 150 mA and of 50 keV, respectively, as well as for a magnetic field of 8 T at the center of the trap. The radius of the electron beam resulted to be 23 μm from Eq. (2.13). The space charge potential becomes zero on the wall of the drift tube electrode and is largest at its center ($r = 0$):

$$V_{sp}(0)[V] \approx \frac{30 I_e\,[A]}{\sqrt{1 - \left(\frac{E_e[keV]}{511} + 1\right)^{-2}}}\left(\ln\left(\frac{r_e}{r_{dt}}\right)^2 - 1\right), \tag{2.20}$$

using Eq. (2.12) for relativistic velocities.

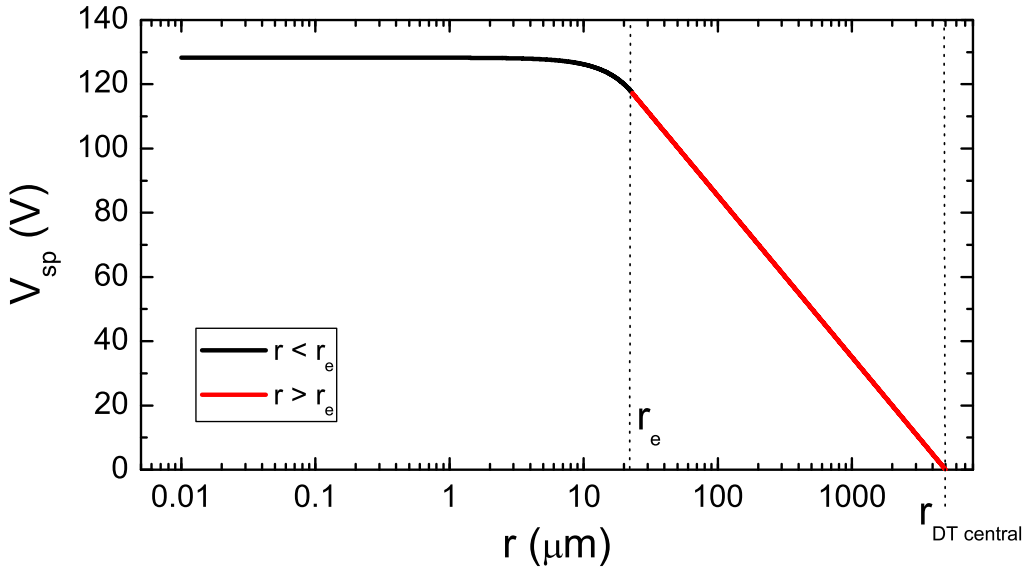

Figure 2.14: Radial space charge potential distribution as a function of the radial position r for an electron beam energy and current of 50 keV and 150 mA, respectively. The radius of the drift tube is 5 mm while the electron beam radius is calculated to be 23 μm for a magnetic field of 8 T.

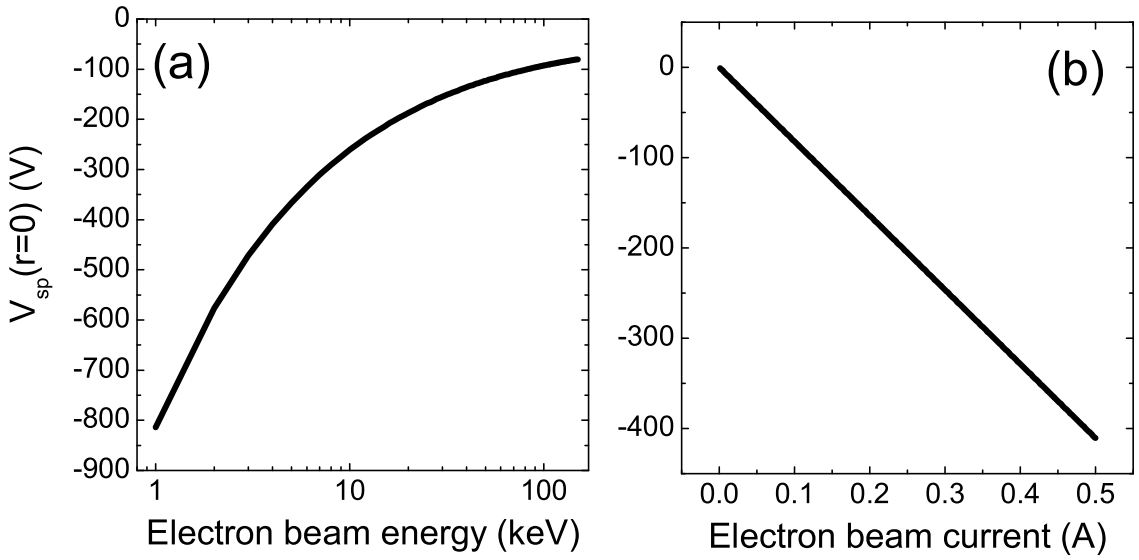

Figure 2.15: (a) The radial space charge potential as a function of the electron beam energy at $r = 0$. (b) The space charge potential versus the electron beam current at $r = 0$. In these figures the beam properties were $I_e = 150$ mA, $E_e = 50$ keV and $r_e = 23$ μm.

Some examples relevant for the present experimental work are described in the following.

The dielectronic recombination resonances of He-like Kr^{34+} occur at electron beam energies of roughly 9 keV. The experiment was performed using a magnetic field of 5 T. Under these conditions, the Herrmann beam radius is 29 μm, and a space charge potential of -183 V is calculated ($r_{dt} = 5$ mm, $I = 100$ mA). Increasing the magnetic field to 8 T, the electron beam energy and current to 50 keV and 150 mA, respectively, results in a beam radius of 23 μm, and, accordingly in a space charge potential of -128 V. Figure 2.15 shows the dependence of the V_{sp} at $r = 0$ as a function of the electron beam current and energy.

We have to note that, due to the different radii of the drift tubes along the beam axis, a so-called axial space charge potential is generated as well. This potential ΔV_{sp}^{ax}, is calculated at the trap center as the difference between the radial space charge potential of two neighboring electrodes with different radii (the central electrode $DT_{central}$ and a second electrode DT_i), thus, $\Delta V_{sp}^{ax} = V_{sp}^{DT_i} - V_{sp}^{DT_{central}}$. The present geometry of the Heidelberg EBIT ($r_{DTcentral} = 5$ mm and $r_{DTi} = 1.5$ mm) results in the axial space charge potential at the trapping center against the drift tube nearby as follows:

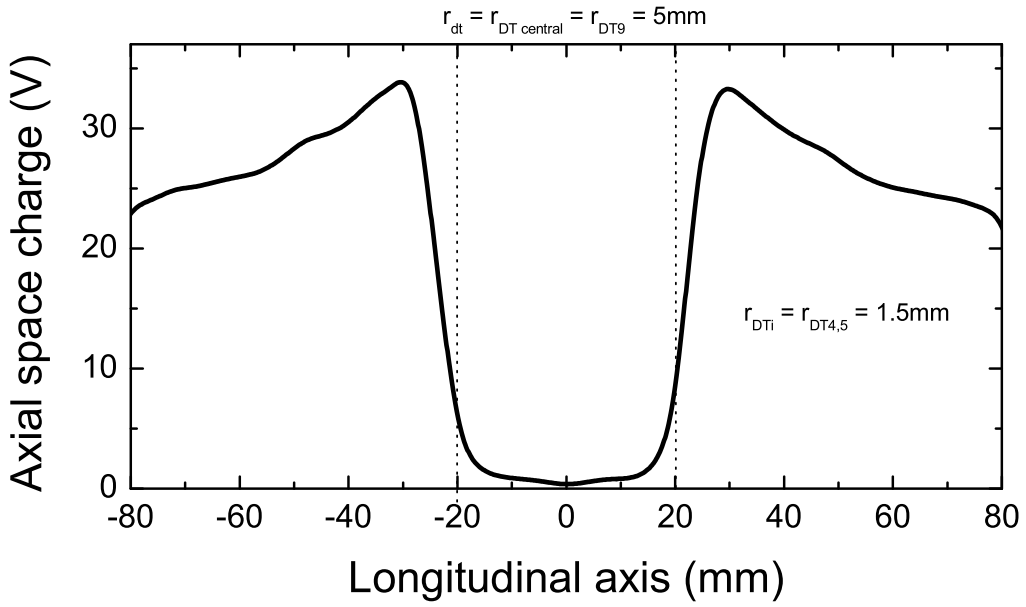

Figure 2.16: Axial space charge potential generated by an electron beam energy and current of 9 keV and 100 mA, respectively (see Fig. 2.5). The middle region (40 mm) corresponds to the central drift tube $r_{dt} \equiv r_{DTcentral} \equiv r_{DT9}$ with a radius of 5 mm. The next electrodes $r_{DTi} \equiv r_{DT4,5}$ have a radius of 1.5 mm.

$$\Delta V_{sp}^{ax}\,[V] = \frac{72.24\, I_e\,[A]}{\sqrt{1 - \left(\frac{E_e[keV]}{511} + 1\right)^{-2}}}\,. \tag{2.21}$$

For instance, a potential well of about 38 V (see Fig. 2.16) is generated along the electron beam axis which efficiently traps ions along the axial direction even without applying any voltage to the drift tube electrodes.

Furthermore, the compensation to the radial space charge potential by positive ions accumulated in the trap has to be also taken into account. The compensation factor f is defined as the ratio between total positive n_q and negative electron n_e charges [Wid98]:

$$f = \frac{\sum_q n_q q}{n_e}\,. \tag{2.22}$$

The actual number of ions and the charge distribution depend strongly on the operating conditions, namely, the electron current, its energy, current density, the

element trapped, injection pressure, trapping time etc. There is also a strong influence by the impurity contents of the trap (including residual gas).

The ion compensation can be estimated by observing the energy shift of dielectronic recombination resonances as a function of the electron beam current under some assumptions. We will show below, in chapter 2.6, that an ion compensation as large as 30 to 40 % can be obtained under normal running conditions.

2.3.3 Electron beam energy

The electrons are accelerated to the required energy by establishing a potential difference between the cathode electrode and the drift tubes. For experiments at medium electron energies, this is done by biasing the drift tube trap assembly at a positive voltage ($V_{drift\ tubes}$) as high as 20 kV in addition to the standard cathode voltage of -1501.5 ± 0.1 V ($V_{cathode}$). For high energy experiments the whole electron gun platform is negatively biased up to -350 kV ($V_{platform}$). Neglecting the influence of the space charge potential, the electron beam energy is therefore given by

$$E_{beam} = (-V_{cathode} - V_{platform} + V_{drift\ tubes}) \cdot q_e \,. \tag{2.23}$$

The voltages applied to the drift tube and electron gun platform are measured by means of two high-precision voltage dividers (see Fig. 2.17). They were designed to have an output voltage range measurable with the highest possible accuracy by means of two high precision multimeters (Keithley 2002 series, see Table 2.2 for their specifications) whose best accuracy is specified in the range of $0.2 - 20$ V. The multimeter read is transfered through a GPIB bus to a PC and recorded every 200 ms by means of a Labview program. The value of the acceleration voltage used to determine the electron beam energy is taken from this instrument.

Table 2.2: Specifications using the Keithley 2002 model multimeter for DC voltage measurements. ΔV represents the uncertainty of the measured voltage.

Voltage (V)	**Range** (V)	**Full scale**	**Resolution** (nV)	**ΔV (24 h)** (μV)	**ΔV (90 d)** (μV)
1	$0.2 - 2$	± 2.10000000	10	1.8	7.6
10	$2 - 20$	± 21.0000000	100	14	63

The *drift tube* voltage divider is mounted on top of the drift tube rack. It consists of 20 resistors of 200 MΩ (type *MG 815*) and a smaller one of 1 MΩ. The dimensions

of the *MG 815* resistors are about 150 mm in length and 9 mm in diameter. The resistor set is located inside a Lucite box surrounded by soft iron sheets in order to reduce electromagnetic noise. Its dividing ratio at constant temperature (± 0.5 °C) is 3986.9 ± 0.4 (see Table 2.3). This ratio was determined by applying very well defined voltages from a special source (Keithley Model 2430 Source/Meter) between 0 V and 1000 V, both positive and negative, ramping them slowly and recording the voltage drop on the different elements, the total current flow, the temperatures in the laboratory and of the divider etc. This divider has been periodically recalibrated, showing always ratios within the indicated error bars.

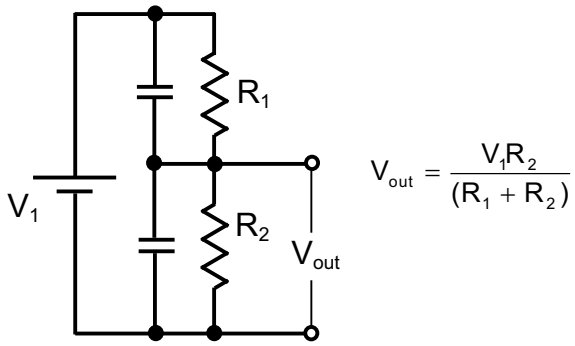

Figure 2.17: Electronic voltage divider scheme for the drift tube and platform with resistors $R_{1,2}$ specified in Table 2.3.

The *platform* voltage divider (see a sketch in Fig. 2.18) is connected to the electron gun platform and has 40 resistors of 200 MΩ. The resistors are mounted on a plastic column inside an inner Lucite cylinder of 260 mm diameter and 1200 mm length. The whole inner cylinder is filled with SF_6 gas in order to avoid any discharges between the divider elements. The metal film resistors are also of the type *MG 815* and have a temperature coefficient, according to their specifications, of 80 ppm/°C, very good long-term stability and narrow fabrication tolerances (1%).

The temperature coefficient of the individual 200 MΩ resistors was (+8390 ±12) Ω/°C (42 ppm); this value is also valid for the whole set of 40 resistors. Initially, a 200 kΩ resistor R_2 was mounted which had a temperature coefficient of (+5.0±0.4) Ω/°C (25 ppm). The total temperature coefficient of the divider ratio was then 17 ppm/°C. Since the temperature fluctuations in the air-conditioned laboratory were typically ± 0.5 °C, the systematic error induced by the thermal coefficient of the divider was at that time ± 0.5 V at 50 kV.

In order to reduce this uncertainty even more, and to prepare the *platform* voltage divider for calibration at the Physikalisch-Technische Bundesanstalt (PTB), several improvements have been introduced to this setup. The temperature dependency of

the whole resistor R_1 set was made nearly negligible small (in the sub-ppm range) by adding to it appropriately chosen resistors with very low resistance values but very high temperature coefficients of opposite sign (5×10 kΩ) in series with the main large resistors of which R_1 was made. Depending on the voltage range to be measured, the voltage output is now read by means of any of three different, selectable resistors, $R_2 = 7.998$ MΩ, 1.267 MΩ and 406 kΩ. In addition, these resistances are composed of combinations of resistors also selected to have roughly a zero total temperature coefficient. For this purpose the thermal coefficients of single resistors were measured in the temperature range of 20°C – 80°C. A conservative

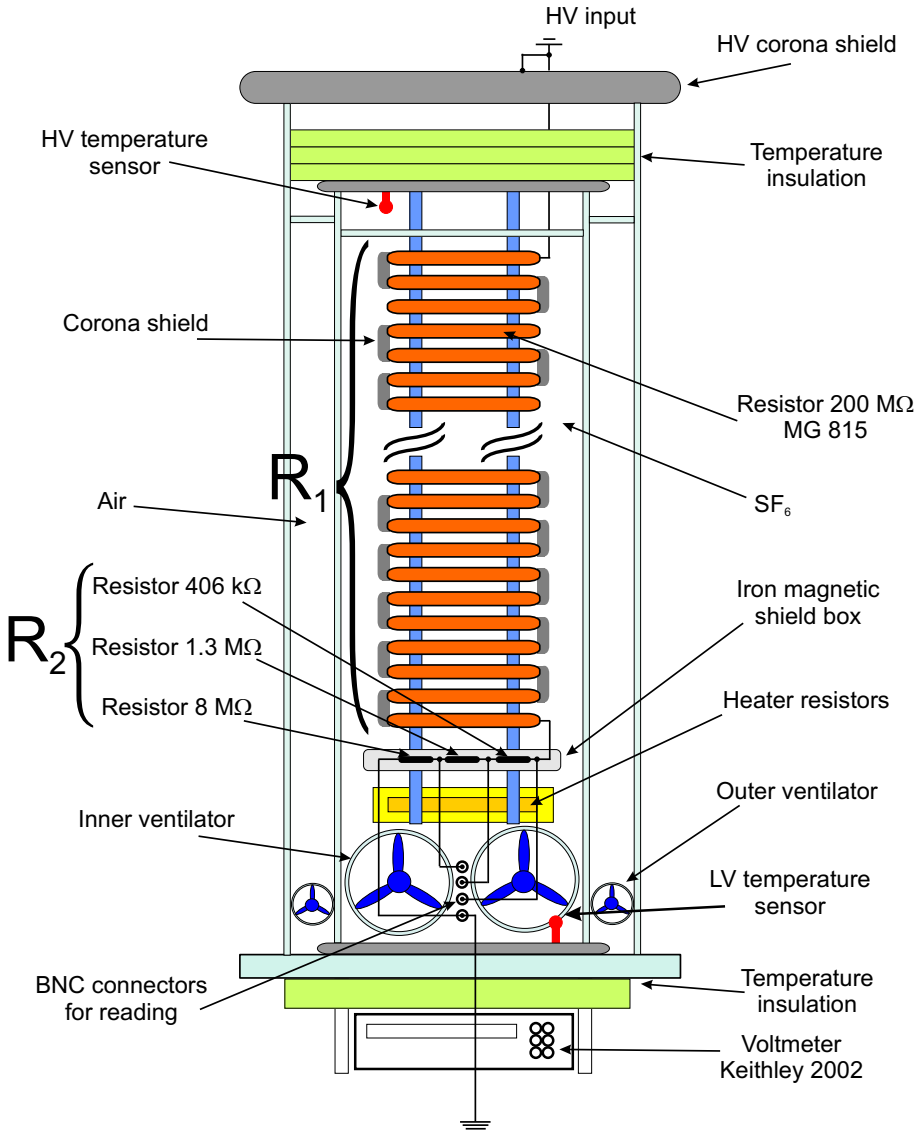

Figure 2.18: Mechanical drawing of the *platform* voltage divider.

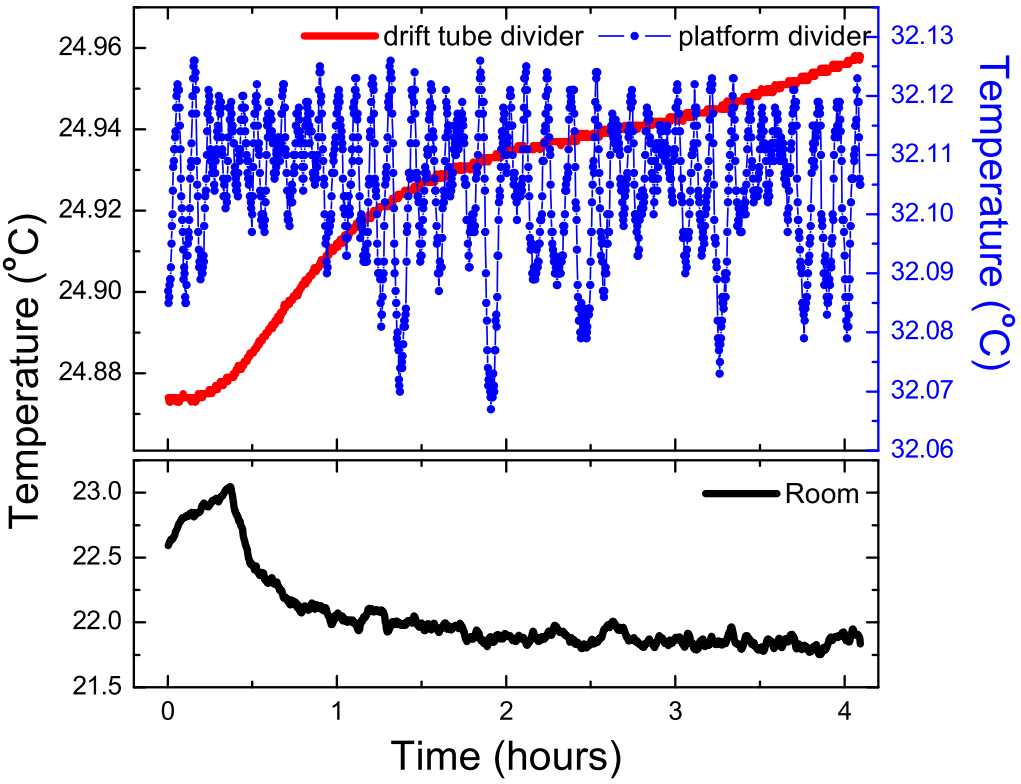

Figure 2.19: Temperature variation of the two voltage dividers and of the room as a function of time.

estimate of the divider temperature coefficient < 2 ppm is considered.

The inner cylinder of the divider has a wall along its axis at 1/3 of its diameter. This wall has holes with two ventilators at the bottom and a slit of about 5 cm at the top which allow to circulate the SF_6 gas up and down the cylinder. An outer concentric cylinder, which thermally isolates the inner divider from the room environment, also reduces external temperature gradients by a forced air flow between the two cylinders using two additional ventilators. An active thermal stabilization system, not shown in Fig. 2.18, allows to maintain a constant temperature inside the voltage divider. The temperature is measured with sensors (type AD 590) which are read by a temperature control unit of type TEC. This unit regulates the current through four heater resistors of 25 W each. This setup reduces the temperature fluctuations to a range as narrow as 0.02 °C at 32 °C (see Fig. 2.19, solid blue dots on the right-hand side scale), even as the external temperature makes excursions of $\pm$ 3 °C during 4 hours. Thus, the voltage divider ratio is expected to stay constant with a maximum variation of less than 2ppm/°C $\times$ 0.02 °C.

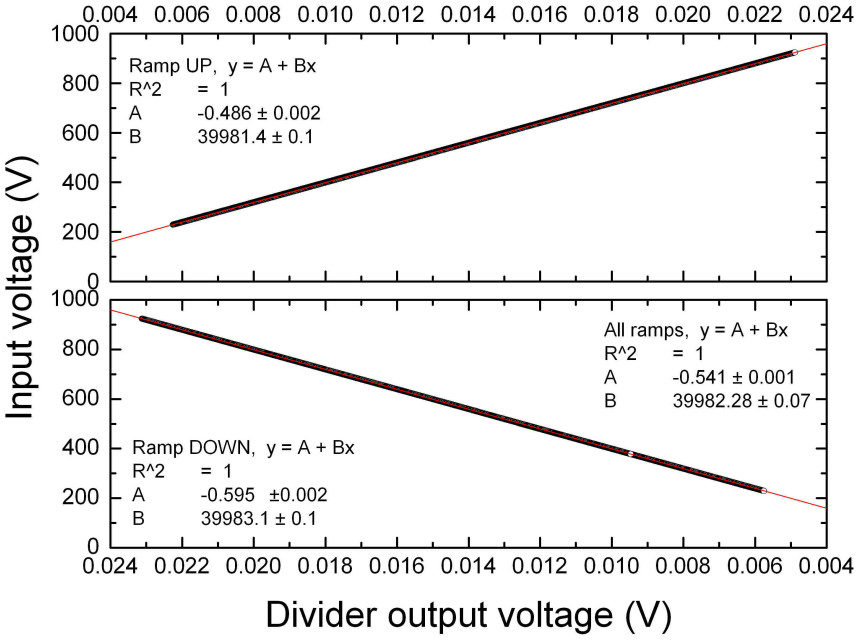

Figure 2.20: Calibration of the *platform* voltage divider for the two ramping directions as a function of the divider output voltage.

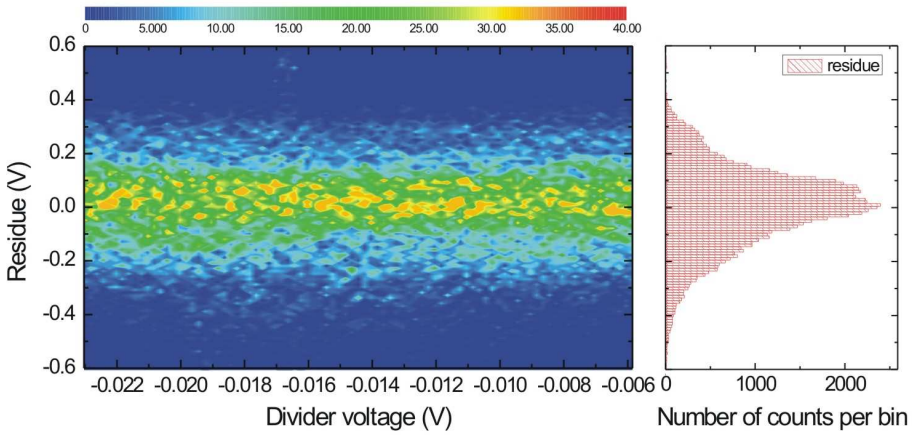

Figure 2.21: Density plot of the residue obtained in the linear fit to the whole data (up and down) shown in Fig. 2.20. The left figure shows the histogram obtained by bining the residual data with 0.01 V.

As in the case of the *drift tube* voltage divider, the *platform* voltage divider is calibrated with a maximum input voltage of 1000 V and with different scan speeds ranging from 5 V/s (typical values for experiments) to 100 V/s. Figures 2.20 and 2.21 show the calibration of this voltage divider for the two ramping directions and the density plot of the residues, respectively. Their measured ratios are shown in Table

2.3. Note that the divider ratio shown in Fig. 2.20 is different from those shown in Table 2.3. The high energy experiments presented in this work were performed without the temperature coefficient compensation and active stabilization setup. Thus, the estimated uncertainty in our results due to temperature fluctuations in the voltage divider resistors is below 0.5 V at 50 kV.

Table 2.3: Characteristics of the voltage dividers developed for the Heidelberg EBIT. R_1 and R_2 are taken as shown in Fig. 2.17.

Label	**R_1**	**R_2**	**Ratio**	**Range (kV)**
drift tube divider	20×200 MΩ	1 MΩ	3986.9 (0.4)	< 20
		7.998 MΩ	992.8 (0.3)	2-20
platform divider	40×200 MΩ	1.267 MΩ	6335.62 (0.01)	12-120
		406.5 kΩ	≈ 20000	40-400

2.4 X-ray spectroscopy setup

In the present experiment, the flux and energy of the emitted photons, as well as the electron energy have to be precisely measured. The simultaneous requirements of large solid angle and a broad spectral range lead to the use of semiconductor solid state detectors. X-ray detectors designed for good energy resolution are typically made of silicon or germanium crystals. These detectors are used in many fields of experimental physics. Semiconductor detectors work as solid state ionization chambers. When an x-ray impinges onto the detector and deposits its energy on a primary electron resulting from an ionization event, a large number of secondary electron-hole pairs are generated in the crystal since the energy of the primary electron is subsequently shared with more electrons from the valence band. As the energy required to create an electron-hole pair in germanium is only 2.96 eV, the number of pairs produced is larger than that of the ion-electron pairs in gas detectors, whose production requires, typically, 10 times more energy. Therefore, semiconductor detectors have better energy resolution due to the smaller statistical fluctuations. The detector crystal is placed between two electrodes generating an electric field. This field collects the free electrons and generates a detectable electrical signal. The amplitude of the signal is proportional to the photon energy. The electronic charge produced in the detector is transformed to a voltage signal by a preamplifier, which is later processed by a multi-channel analyzer.

Table 2.4: Some properties of a solid-state germanium detector (*GLP* 36360) used at the Heidelberg EBIT.

Geometry	Coaxial
Area (mm^2)	1018
Crystal thickness (mm)	13
Be window thickness (mm)	0.254
Resolution (eV)	560 at 122 keV
Distance to the trap (mm)	343.7 (10)
Solid angle (sr)	86 (5) 10^{-4}

In this work, a *GLP* 36360 (see Table 2.4) coaxial detector with high efficiency over a broad spectral range (see Fig. 2.22) was used. It is made of intrinsic germanium with an impurity concentration below 10^{10} atoms/cm^3. Coaxial Ge-detectors have a larger detection volume than those with planar geometry.

Generally, detectors are characterized by their detection efficiency and resolution. The detection efficiency depends on the solid angle Ω subtended by the detector as seen from the source or interaction point and its intrinsic efficiency ϵ_{int}. The solid angle is calculated from the experimental geometry:

$$\Omega = \int_A \frac{\cos\theta}{d^2} dA\,. \tag{2.24}$$

Here, d represents the distance between the source and the surface element dA. θ is the angle between the normal to the surface element and the source direction. For a non-negligible source size a second integration has to be taken into account. For the particular case of a point source located along the axis of a circular cylindrical detector where the distance between them $d \gg a$ (a is the detector radius), the solid angle is approximated by

$$\Omega = \frac{A}{d^2}\,. \tag{2.25}$$

The intrinsic efficiency is the fraction of photons registered by the detector over the total number of photons impinging on it:

$$\epsilon_{int} = \frac{\text{registered photons}}{\text{photons on detector}}\,. \tag{2.26}$$

This intrinsic efficiency depends on the type of radiation. In the case of a photon hitting a germanium detector, three main processes occur, namely, the photoelectric effect, coherent and incoherent scattering (Rayleigh and Compton scattering) and pair production. Compton scattering and pair production can be safely neglected at the present photon energy range. The photoelectric effect arises when an atomic electron absorbs a photon, being ionized and subsequently ejected from the atom with an energy equal to the photon energy minus the binding energy of the electron. The cross section can be calculated for example using the first-order Born approximation for photons well above the K-shell binding energy [Leo87].

The total cross section σ due to these processes yields

$$\sigma = \sigma_{photoionization} + Z\sigma_{Compton} + \sigma_{pair} \approx \sigma_{photoionization} \,. \tag{2.27}$$

The product of the total cross section and the density of atoms N gives the interaction probability per unit of length:

$$\mu = N\sigma = \sigma \left(\frac{N_A \rho}{A} \right) \,. \tag{2.28}$$

Here, N_A is the Avogadro number and ρ the density of the material.

Figure 2.22 displays the calculated intrinsic efficiency of germanium crystals of different thickness combined with Be windows as a function of the photon energy. Here, the solid black curve shows the efficiency of the detector used in the present work, which has a 254 μm Be window and a Ge crystal thickness of 13 mm. Over the photon energy range of roughly 8 to 100 keV, the efficiency of the detector is almost 100 %, excluding the K-edge region of germanium at 11.1 keV. These curves were calculated using a parametric equation for the efficiency given in Ref. [DMB 98]. In experiments, the attenuation of the photons by the different beryllium windows has to be taken into account as well.

The energy resolution R of a detector is conventionally defined as the full width at half maximum (FWHM) of a peak divided by the photon energy E:

$$R = \frac{\mathrm{FWHM}}{E} \,. \tag{2.29}$$

The overall energy resolution in a germanium detector is generally determined by three factors: the statistical spread in the number of charge carriers produced in the crystal W_D, the variation in the charge collection efficiency W_X, and the electronic

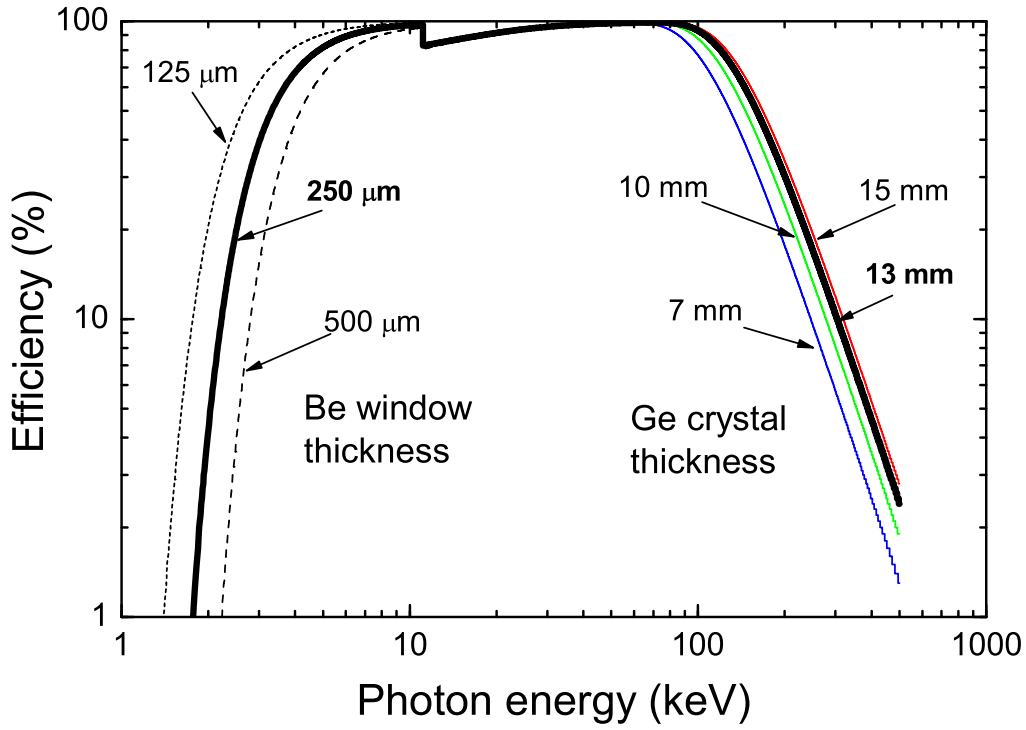

Figure 2.22: Intrinsic efficiency as a function of the photon energy. The black solid curve shows the efficiency for the Ge-detector used in the present experiments (*GLP* 36360).

noise W_E. The total FWHM W_T can be expressed as the sum of the quadrature of these three contributions as follows:

$$W_T^2 = W_D^2 + W_X^2 + W_E^2 \,. \tag{2.30}$$

The second contribution, W_X, is the most significant one in detectors of large volume and low average electric field. The third factor, W_E, represents the noise caused in all the electronic components following the detector. At low energies, the contributions from electronic noise W_E and charge collection W_X dominate, while W_D becomes important at higher energies.

2.4.1 Line shapes in solid state detectors

When a monoenergetic photon impinges on solid state x-ray detectors, the expected Gaussian pulse height distribution is always distorted by tails at the low-energy side. These are a result of the incomplete charge collection in the detector crystal, due to defects or impurities in the crystal [Gun78, GR80]. The observed shape can

be described as a mixture of symmetric and asymmetric profiles in the following analytical form [Wid98]:

$$y(E) = A\, e^{-\frac{(E-E_c)^2}{2\sigma^2}} + a\, A\, e^{b(E-E_c)} \left[1 - e^{-\frac{c(E-E_c)^2}{2\sigma^2}}\right] \mathrm{H}\,(E - E_c)\ , \tag{2.31}$$

where E_c denotes the centroid energy of a Gaussian distribution with an amplitude A. a, b and c are free parameters used in the fitting procedure for the tail characterization. The second term is multiplied by a Heaviside function H which only acts at the lower side of the centroid (see Fig. 2.23a).

A more detailed description and analysis of the response of solid state detectors is given in Ref. [CMH 01]. By recording the spectra of a monoenergetic source, it has been empirically found that the line shape can be described by the primary Gaussian peak (G) accompanied by a long flat structure (S) at the low-energy side of the centroid. In many detectors such a flat structure is superimposed by a second flat one (TS), and a peak due to the escape of K_α x-rays from the detector crystal is observed and denoted as ESC (not shown in Fig. 2.23b). In addition, an exponential-like feature (D) on the low energy side of the main Gaussian peak is needed to fit the data. By taking into account the features, G, S and D, the observed line shapes in Ge-detectors are reproduced as shown in Fig. 2.23b. The exact function used for the fitting procedure is

$$\begin{aligned} y(E) = A_G\, e^{-\frac{(E-E_c)^2}{2\sigma^2}} + A_S\ \mathrm{erfc}\left(\frac{E-E_c}{\sigma\sqrt{2}}\right) + \\ A_D\, e^{\frac{E-E_c}{\beta}}\ \mathrm{erfc}\left(\frac{E-E_c}{\sigma\sqrt{2}} + \frac{\sigma}{\beta\sqrt{2}}\right)\ , \end{aligned} \tag{2.32}$$

where A_G, A_S and A_D are the amplitudes for the Gaussian, the flat structure and the exponential contribution, which were treated as free parameters. β is the slope of the exponential feature, σ the standard deviation of the Gaussian component and $erfc$ the complex error function. The quality of the fits was tested with the χ^2/DoF method by successive iterations. As an example, Fig. 2.23 shows the result of these fitting function profiles and the plot of the obtained residue for x-rays due to the radiative decay of the doubly excited state $1s2p^2$ in krypton ions. The data points fitted with the function (2.31) resulted in a χ^2/DoF of about 0.82 while a slightly better χ^2/DoF of 0.93 was obtained by using Eq. (2.32).

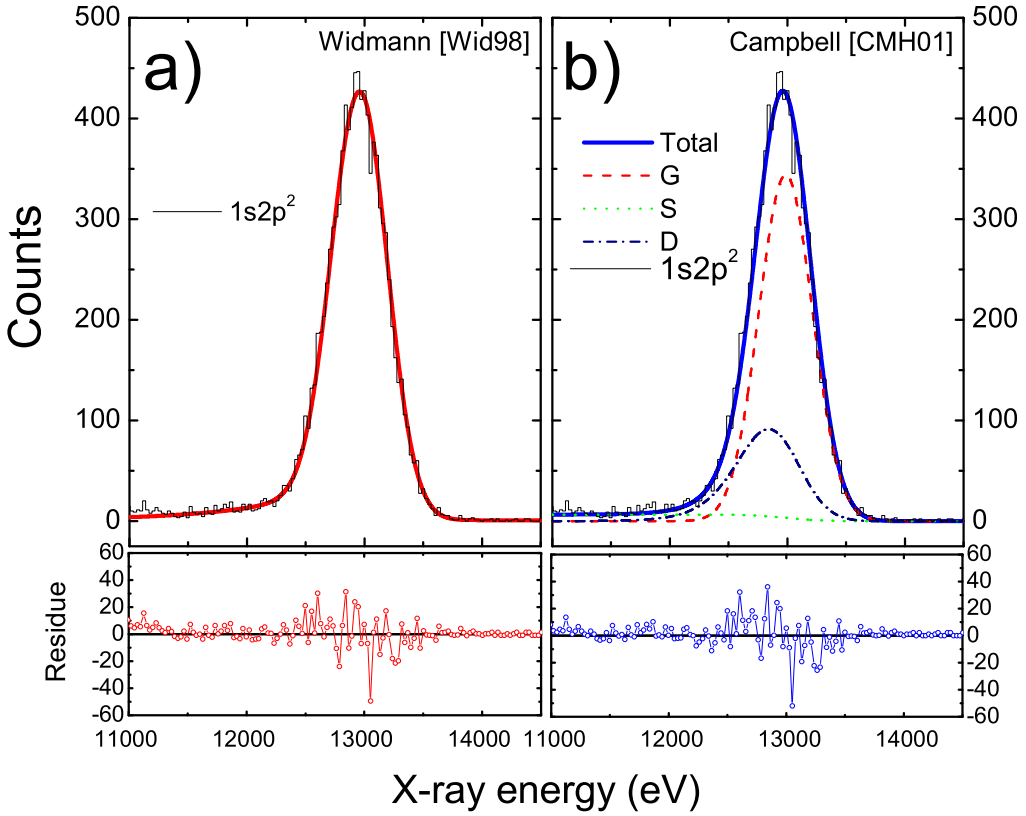

Figure 2.23: Experimental data for the x-ray peak emitted from the radiative emission of the $1s2p^2$ DR resonance of Kr ions and fits: (a) with Eq. (2.31) and (b) with Eq. (2.32). Both fitting procedures result in an almost perfect description of the experimental line shape and the quality of both fits is practically identical. The lower diagrams display the residuals.

2.5 Experiment control and data acquisition

As it has been described above, in the present experiments two energy values have to be measured and recorded simultaneously, namely the photon and the electron beam energy. Since this means that a pulse and a slowly varying ramp signal have to be digitalized in coincidence, we have used a pulse sensing ADC (Analog Digital Converter *Silena 4418*) on a CAMAC crate. The ADC requires the following pulses in order to proceed with the conversion: the amplified analog pulse from the Ge-detector, a pulse with a height proportional to the drift tube voltage and a gate pulse which triggers the module. Figure 2.24 shows schematically the data acquisition system used for the photon and electron energy collection.

A Labview application running on a personal computer controls the acceleration voltage. A voltage ramp is produced with a two channel, 16-bit DAC ($0 - 10$ V)

function generator which is used to program the output of a high voltage power supply. The sawtooth function allows to scan the relevant DR resonances at rates of 5 V/s to 100 V/s. The function generator provides a second ramp, which is fed into a second channel of the ADC. The reason for not using the first sawtooth is that the range $(0 - 10$ V) of the ADC can be fully used in this way, and the additional digitalization noise introduced by this ADC is therefore reduced. A third signal at the end of each scan cycle is used for the EBIT dump (see section 2.1.1). The dump is always set at the end of the scanning to make sure that the ion charge distributions

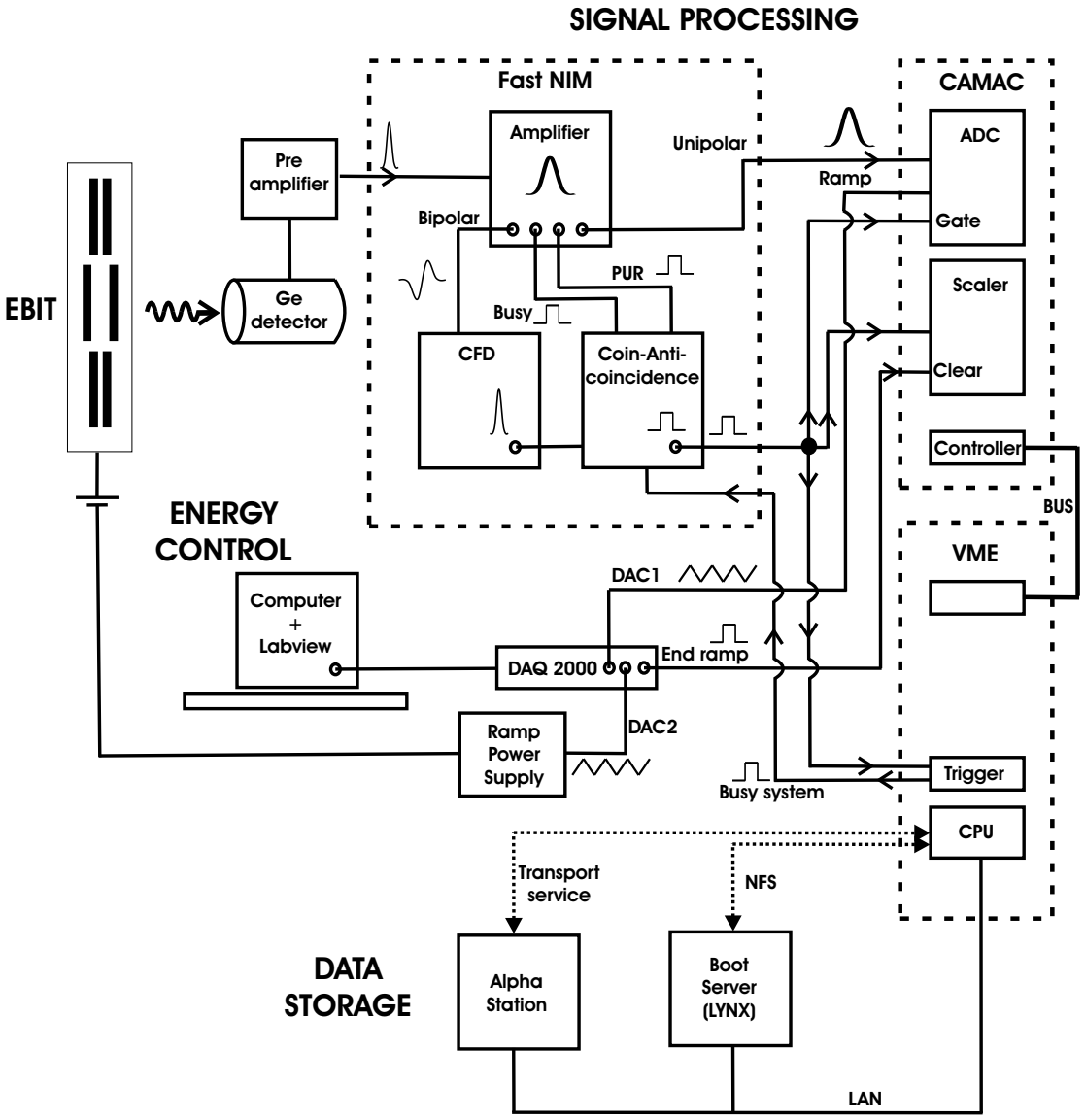

Figure 2.24: Overall scheme of the data acquisition system.

at the DR resonance region is always the same. This signal is also used to clear a CAMAC scaler which counts the photons on each ramp. Such information allows to distinguish in the data analysis between the up or down direction of the ramping.

At a given energy during the scan, photons emitted are recorded by the germanium detector. The output signal of its preamplifier is sent to a spectroscopy amplifier (*ORTEC 672*). This amplifier provides four output signals: bipolar and unipolar outputs, a busy and a pile-up-rejection (PUR) signals, respectively. The unipolar output is directly sent to the ADC.

The gate used for the ADC trigger is prepared as follows: the bipolar signal passes through a constant fraction discriminator whose output is set in coincidence to the busy signal of the spectroscopy amplifier. In addition, the PUR signal and a busy signal of the data acquisition system are set in anti-coincidence.

The CAMAC crate is controlled through a bus by a VME crate. The operating system on the VME crate (RIO processor) of this computer is LYNX. The data acquisition software running on the VME computer is a multi-branch system (MBS), which provides a transport service in order to transfer the raw data to a client. In our case, the client is called GOOSY (GSI-Online-Offline-System), which runs on an Alpha work station and stores the data in an event-by-event list mode. GOOSY allows to plot and analyze the data online or offline.

2.6 Test Measurement: DR in He-like Kr^{34+}

During the setup time, a preliminary experiment with He-like krypton ions was carried out to test different parts of the data acquisition system and explore various possibilities. Krypton can already be brought to the He-like state at energies beyond 4 keV, and can be filled easily into the EBIT. Another reason for the choice of Kr was the availability of data by other groups for comparison. Although our results are incomplete, due to the lack of a reliable calibration of the electron and x-ray energy scales at that time, they are illustrative of the photorecombination processes and therefore presented in the following section.

2.6.1 Dielectronic recombination in He-like Kr^{34+} ions

The experimental data previously available for He-like krypton ions were mainly related to the x-ray region. The wavelengths of its K-shell x-rays have been accurately measured with a high-resolution crystal spectrometer (see Fig. 2.25) at the

LLNL EBIT by Widmann [WBD95]. The achieved precision of 55 ppm allowed to test theoretical predictions with experimental data. At the Berlin EBIT, the DR resonance strengths for the KLn (n = 2 to 5) series of He-, Li- and Be-like krypton ions have also been measured by Fuchs [FBR 98] providing a better understanding of the ionization balance in tokamak plasmas (see Fig. 2.26).

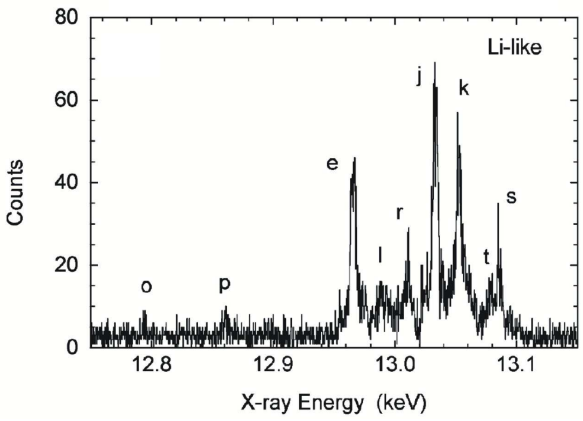

Figure 2.25: Spectrum of Li-like satellites of krypton ions obtained with x-ray crystal spectrometer by Widmann [WBD95] by scanning the electron beam energy in the range from 8.7 to 9.5 keV.

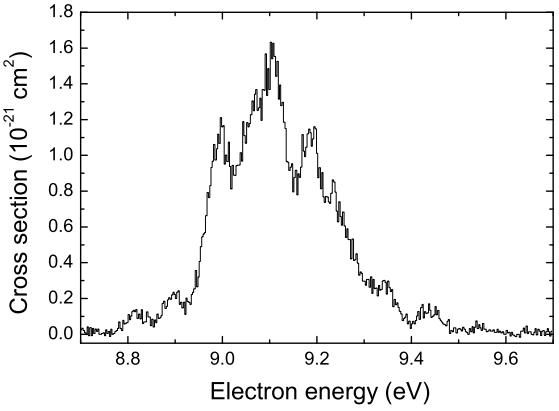

Figure 2.26: Measured total DR cross section of the KLL resonances of krypton ions (from Fuchs, [FBR 98]).

In order to cover a region including the main dielectronic resonances of the K-shell and also the direct excitation of the $n = 1$ to $n = 2$ transitions, the electron beam energy was swept up and down between 7 and 14 keV. The scanning time in each direction was about 50 s. The trap was dumped each 300 s in order to avoid

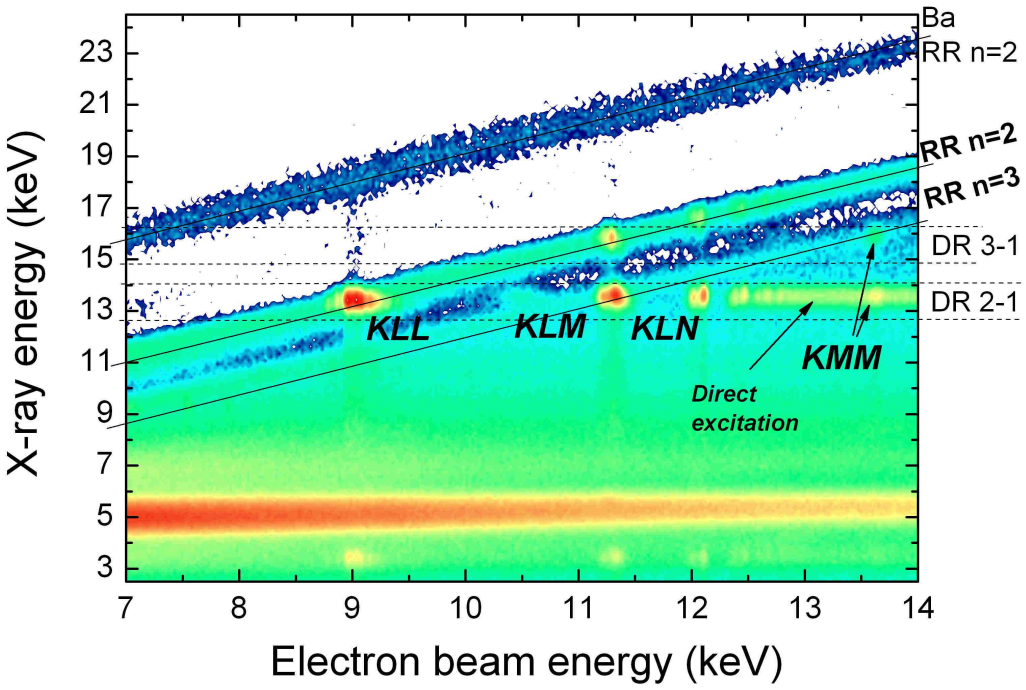

Figure 2.27: Scatter plot of the photorecombination in krypton ions. Diagonal bands due to RR into the $n = 2$ and $n = 3$ shells are visible. The horizontal line indicates the photon transitions from $n = 2 \rightarrow 1$ after KLL, KLM, KLN,... DR processes, indicated as bright spots. The broad band at low x-ray energies (at $\approx$ 5 keV) corresponds to x-ray lines resulting from $n = 3 \rightarrow 2$ transitions of impurity barium ions. The upper diagonal band represents RR into the $n = 2$ shell of barium. At lower x-ray energies (3.5 keV), weak features are observed due to the escape peak in the Ge-detector.

the excessive accumulation of impurity ions. The axial magnetic field was fixed at 5 T.

In Fig. 2.27, the photon energy is plotted versus the electron beam energy. These two-dimensional (2D) maps allow to project selected regions either onto the electron beam energy axis or onto the x-ray energy axis. The acquisition time needed to record this overview map was about 5 hours at an electron beam current of 60 mA.

The diagonal bands displayed in Fig. 2.27 are due to the radiative recombination (RR) processes (see section 1.2.2) into states with principal quantum number $n = 2$ and $n = 3$. The uppermost weak diagonal band is due the RR into $n = 2$ states of the impurity barium ions. A projection of the krypton $n = 2$ band onto the electron beam energy axis is shown in Fig. 2.28a. A series of bright spots along a horizontal band at x-ray energies of about 13 keV are assigned to the radiative decay ($n = 2 \rightarrow 1$) after the formation of intermediate excited states in the KLn ($n = 2, 3, 4, ...$) DR processes (see Fig. 2.28b). In this band, the cluster at

the lowest electron energy ($\approx$ 9 keV) is due to the KLL DR resonances. At an electron energy of approximately 11.3 keV, the KLM resonances appear, which can radiatively decay either through an $n = 2 \rightarrow 1$ transition or through an $n = 3 \rightarrow 1$ transition leading to higher photon energies. At 12.1 keV, the KLN resonances are observed. Increasing the electron beam energy even more, the resonances become unresolvable and, eventually, overlap with lines produced at electron energies greater than 13.1 keV due to the direct excitation process of the $1s$ electrons to the $n = 2$ shell [WBD95]. At about 13.7 keV, superimposed on the direct excitation region, the KMM resonance appears, resulting from capture into $n = 3$ and excitation from $n = 1$ to $n = 3$.

The features observed at very low x-ray energies of about 3.5 keV are due to the escape peak, which appears when part of the photon energy deposited into the Ge detector (here $\approx$ 13 keV) escapes it as a Ge K_α photon ($KL_1 = 9.69$, $KL_2 = 9.86$ and $KL_3 = 9.89$ keV, [DKI 03]).

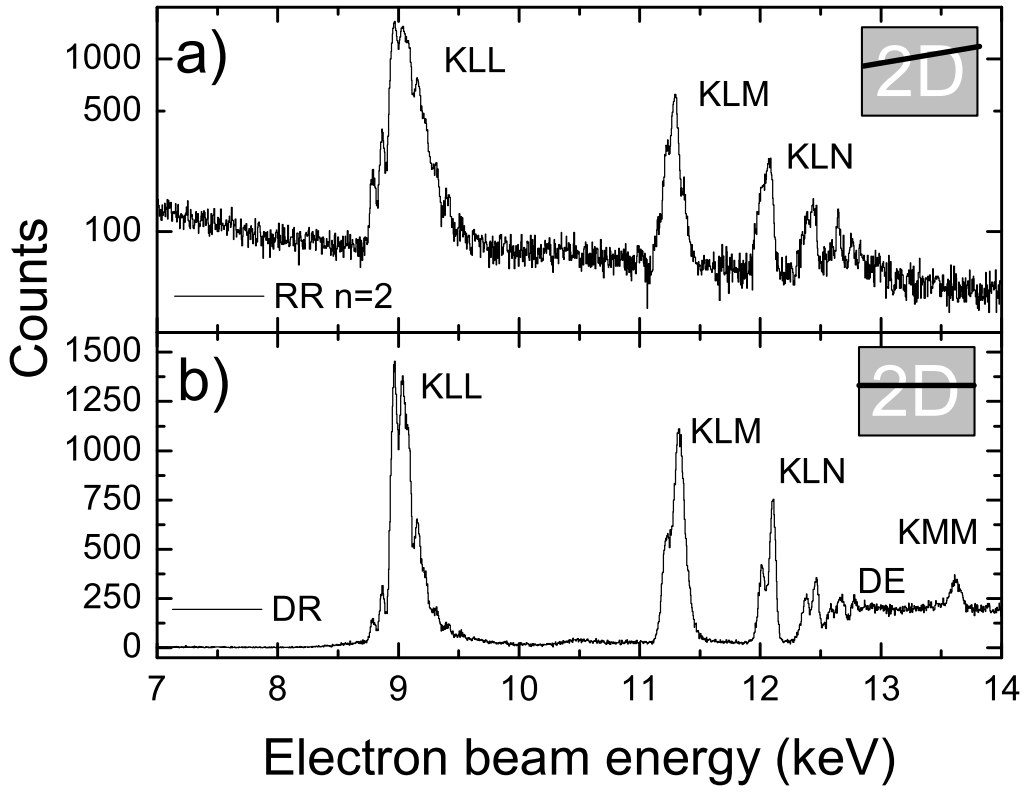

Figure 2.28: Photorecombination of krypton HCI. Projections of the diagonal band (a) due to radiative recombination into $n = 2$ states and of the horizontal band containing the $n = 2 \rightarrow 1$ transitions at about 13 keV x-ray energy (b).

Scans of the electron beam energy from 7 to 11 keV covering only the KLL resonances were also carried out (Fig. 2.29). The speed of the electron beam scan was about 90 V/s and, thus, every cycle lasted roughly 100 s.

In order to reduce the ion temperature and to obtain a better electron beam energy definition, the external longitudinal trapping potentials were set to zero, thus making the trap as shallow as possible. A relative energy resolution of $E/\Delta E \approx 300$ at 9 keV was achieved. Nevertheless, even without positive potentials applied to the outer drift tubes, an axial trapping potential ($\approx$ 20 eV at 50 mA and 9 keV) is always induced by the electron beam simply due to the changes in the value of the radii of the drift tubes along the beam axis, as discussed in more detail in section 2.3.2. The next subsections describe the analysis of the KLL DR resonances of He-like Kr^{34+} ions.

2.6.2 Towards an absolute electron beam energy determination

The upper diagram in Fig. 2.29 displays the photon yield at different x-ray energies against the electron acceleration voltage. Here, the KLL DR resonances of krypton ions from He-like Kr^{34+} (the first three spots on the left-hand side) to O-like Kr^{28+} ions (the spot on the right) can be seen. The lower diagram in Fig. 2.29 shows the projection of the x-ray intensity onto the electron energy axis. The theoretical relative contributions of different DR states to the observed He-like resonances [Saf02] are indicated as histogram bars.

There are three main DR resonance groups from the initial He-like state ($1s^2$) leading to intermediate $1s2l2l'$ states, namely, those corresponding to the $1s2s^2$, $1s2s2p$ and $1s2p^2$ excited configurations. Each of them consist of several different states. The $1s2s^2$ ($^2S_{1/2}$) peak with the lowest excitation energy is isolated from the others, as well as the peak due to the $1s2s2p$ ($^2P_{1/2}$) state at 8.9 keV. The peak corresponding to the $1s2p^2$ levels contains several closely-spaced resonances with total angular momentum $J = 1/2$ or $J = 3/2$ which can not be resolved. Here, two strong resonances, the $^4P_{5/2}$ and $^2P_{3/2}$, are blended together at an electron energy of about 9 keV. Other $1s2p^2$ resonances overlap with those belonging to Li-like ions (resonant state $1s2s^22p$). In Fig. 2.30, the four theoretical [Saf02, Che86] He-like resonances (delta functions convoluted with a Gaussian distribution of 40 eV width, dotted blue and solid black curves) are shown in comparison with the experimental data (step curve). Here, the energy scale was referred to the predicted $1s2s^2$ line position.

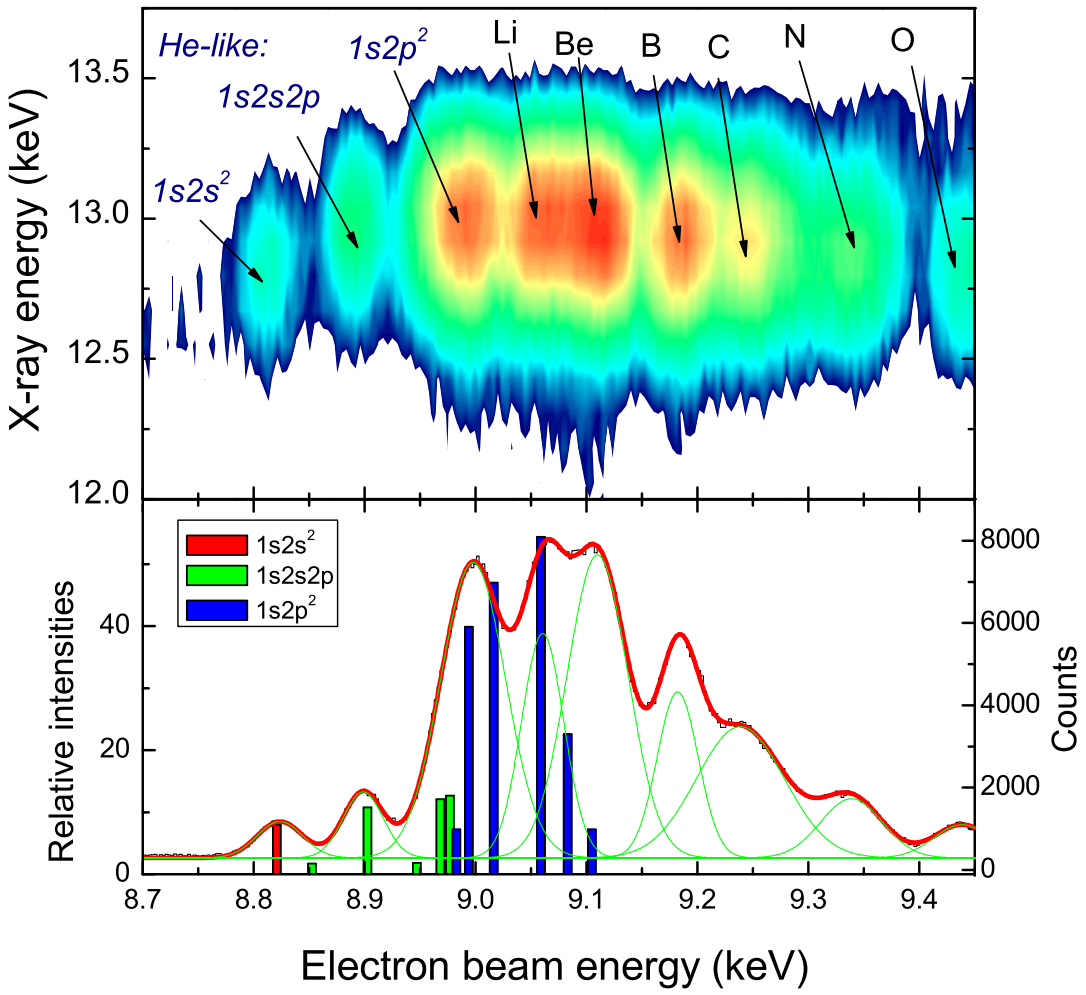

Figure 2.29: Top: two-dimensional map of the KLL DR region of He- to O-like krypton ions. Bottom: projection of the KLL resonances onto the electron beam energy axis together with an histogram which shows the (theoretical) relative intensities for the three analyzed He-like DR resonances.

We have used series of Gaussian functions (see green curves in Fig. 2.29) to fit the centroids of the resonance peaks appearing in the projections onto the electron beam energy axis. The quality of these fits was tested with the χ^2 over degrees-of-freedom (DoF) method. The widths of the projected resonances are mainly caused by the electron beam energy spread, due to the space charge potential and to high-voltage noise of the power supplies.

Due to the work function of the materials used in the cathode ($\Phi_{Ba,W} = 2.00$ eV) and in the drift tube electrodes ($\Phi_{Cu} = 4.65$ eV), a final correction of 2.65 eV has to be applied to the measured voltage.

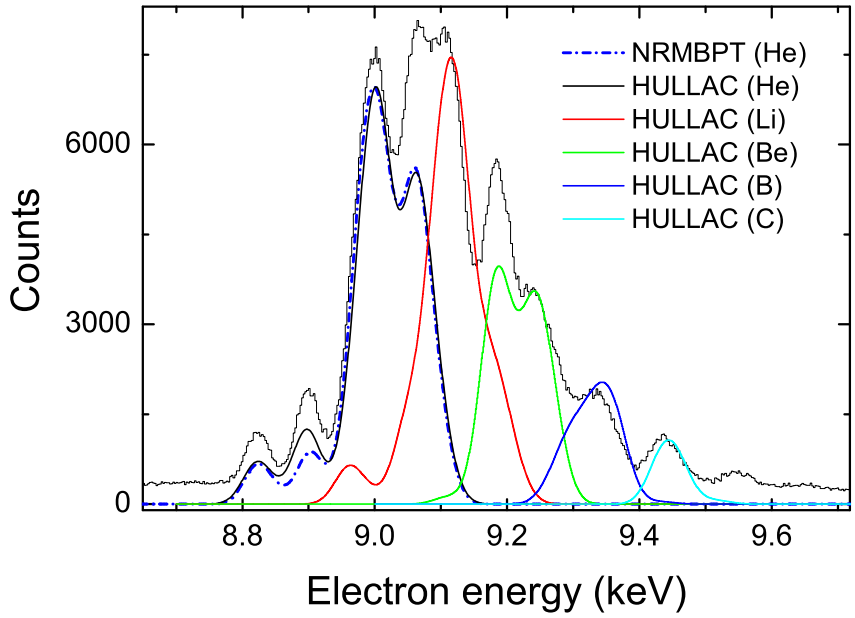

Figure 2.30: Experimental data (black) in comparison with two theoretical curves: the dotted blue curve is calculated by convoluting the He-like resonances given by Safronova in the NRMBPT [Saf02] with a Gaussian distribution with an experimental width of 40 eV. The solid curves show predictions obtained with the HULLAC code [Che86, FBR 98] for several charge states.

As has been discussed in detail in the experimental section, the actual electron beam energy in the central drift tube and thus the measured energy of a given resonant state of DR depends on the combined electron and ion space charge potentials. According to Eq. (2.20) the electron space charge depends linearly on the electron beam current I_e. Therefore, by precisely determining the acceleration voltages at which a certain DR resonance appears as a function of the beam current and extrapolating to $I_e = 0$, where neither electron nor ion space charge exist, one can obtain its absolute excitation energy.

Figure 2.31 shows the acceleration voltage of three He-like KLL DR resonances as a function of the electron beam current. As expected, they clearly display a linear dependence on the electron beam current. A polynomial of second order was also tried, but the fit quality was found to be significantly poorer (see details in Table 2.7). As indicated on the top of Fig. 2.31, extrapolated absolute resonance energies for the three He-like lines were determined with an experimental uncertainty of $\pm$ 1 eV. Since the observed shift (see Fig. 2.32) of the $1s2p^2$ line from the theoretical prediction is a result of the combined space charge potential of the electrons and the ions, one can try to extract the ion space charge potential under the assumption that the one for the electrons is given by Eq. (2.20). Then, the ratio of the experimental shift

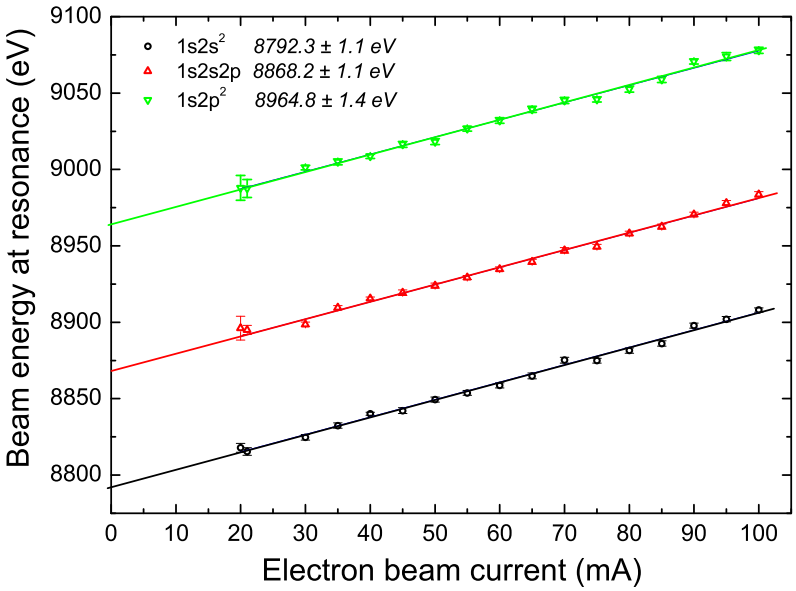

Figure 2.31: The observed *apparent* resonance energy versus the electron beam current for three He-like ion KLL DR resonances. The numbers on the top of the figure represent the electron beam energy for each resonance extrapolated to zero electron beam current.

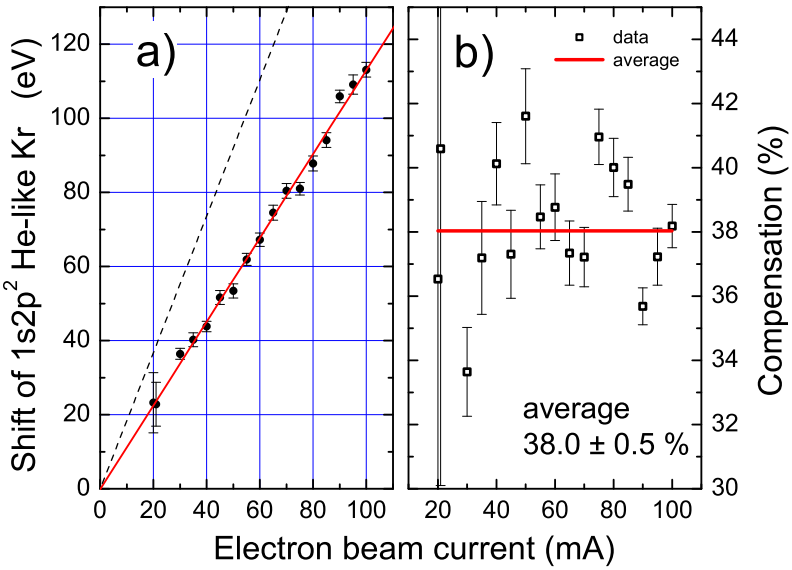

Figure 2.32: a) Observed shift of the $1s2p^2$ DR resonance in Kr^{34+} from the calculations [Saf02] as a function of the electron beam current. The red line represents a linear fit to the data points, while the dashed black line shows the shift only due to the radial space charge potential. b) Calculated ion compensation of the space charge potential for the $1s2p^2$ resonance.

and the calculated radial space charge yields the percentage of the compensation by the ions. Figure 2.32b displays the deduced ion compensation as a function of the electron beam current which results, under the given conditions, to be about 38% of the radial space charge potential and essentially independent on the electron current.

As shown in Fig. 2.33, no significant effect of the total space charge on the accumulation of positive ion charges could be observed by varying the dump interval between 300 s and 40 s (shorter cycles result in less trapped ions).

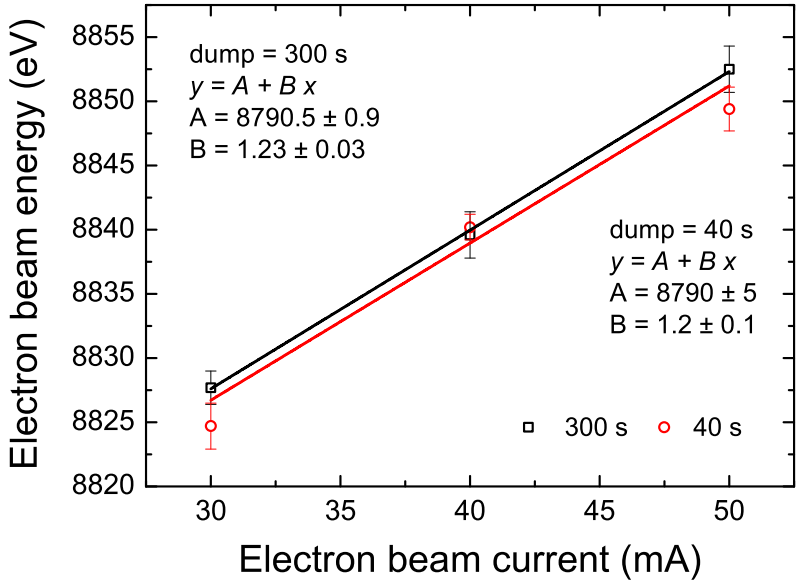

Figure 2.33: Resonance energy ($1s2s^2$) as a function of the electron beam current with different dumping times, 40 s (red circles) and 300 s (black squares).

In Fig. 2.34 we explore height and space charge potential corrected positions of the resonances as a function of the electron beam current for two groups of $I_e = 20-40$ mA and $70-100$ mA, respectively. Here, we observed that the analyzed He-like peaks of interest are not disturbed by the increase of the other charge state populations (Li- to O-like) at lower values of the electron beam current.

Finally, in Fig. 2.35 we explore the dependence of the voltage difference obtained for the He-like DR resonances on the ramping direction (up or down) at a scan rate of 90 V/s for different electron beam currents. While ramping up, the $1s2s^2$ and $1s2s2p$ resonances consistently appear at values 4.1 eV higher than when under ramping down. The capacitive load of the voltage divider, due to the input impedance of the voltmeter and the capacity of the coaxial cable used to connect R_2 with the instrument, causes an apparent shift of -1.2 V at about 9 kV when the average

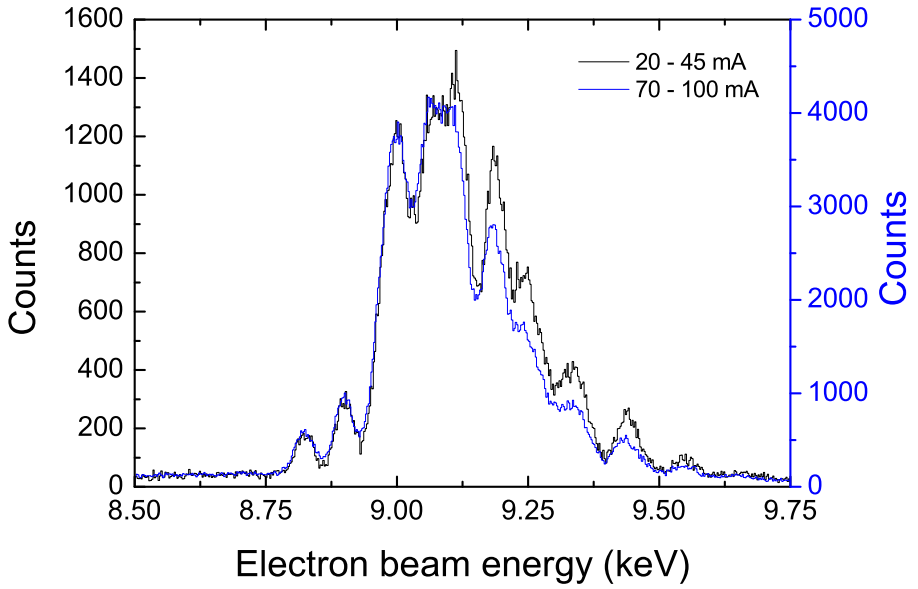

Figure 2.34: Projections of the KLL DR region for two different ranges of electron beam current ($70-100$ and $20-45$ mA). The energy scale of these curves is referred to the predicted resonance excitation energy of the $1s2s^2$ state (see Table 2.5).

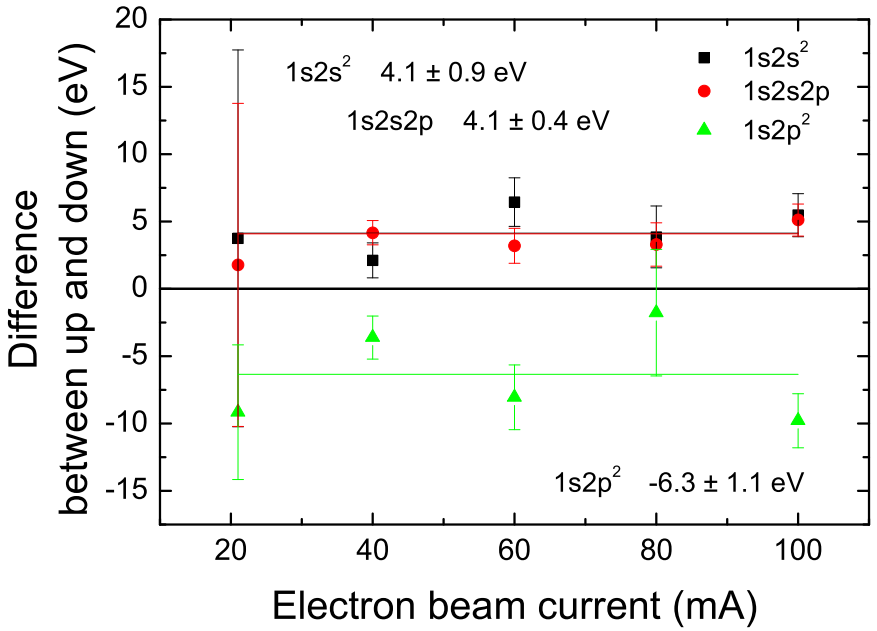

Figure 2.35: Energy difference between the centroids of the He-like resonances while ramping up and down the electron beam energy, as a function of the electron beam current.

divider ratio is used, as it is the case in Fig. 2.36. This value, in fact, increases the discrepancy observed in that figure, resulting in a difference of 5.3 V for the resonances between the up and down ramps. The most likely explanation is a dynamic change in the ion charge balance, which can qualitatively appreciated from Fig. 2.36. The up branch shows a photon yield for the He-like resonances of about 20% higher in comparison to the down branch. This behaviour could be induced by the strong recombination of Li- to C-like ions in the down branch when the beam energy decreases before the He-like resonances are hit, as illustrated in Fig. 2.36. The change in the ion population and its average charge state could cause a reduced ion compensation of the space charge, thus possibly explaining the observed up/down asymmetries. The $1s2p^2$ resonance shows a down shift of 6.3 eV, into the opposite direction and is most probably due to the influence of the nearby Li-like resonances peaks. Nonetheless, by using the sum of the up and down branches, as has been done in all the measurements presented in this work, this effect should vanish, or at least be strongly attenuated.

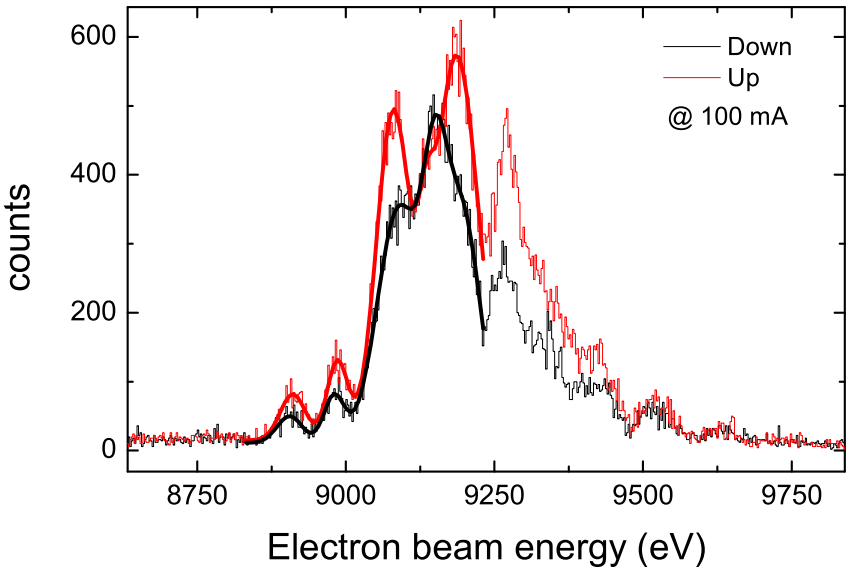

Figure 2.36: Projections of the KLL DR region for the two branches of the ramp at a fixed beam current of 100 mA. The displayed energy scale is uncorrected for the space charge potential.

2.6.3 Results for DR resonance positions of He-like Kr

By taking into account the theoretical relative intensities (parameter QD in Table 2.5) it is possible to estimate the center of gravity of the three peaks for both, the excitation and the x-ray energies. Table 2.5 shows the theoretical resonance and

x-ray energies (see section 2.6.4) for the He-like krypton ions. They are calculated in a Non-Relativistic Many Body Perturbation Theory (NRMBPT) approach by Safronova [Saf02] and through a Multi-Configuration Dirac-Fock method ($MCDF_M$) by Harman [Har05]. The first column indicates the usual labels (compare, *i.e.*, [JPS84]).

Table 2.5: Theoretical DR resonance energies of He-like krypton ions from $MCDF_M$ [Har05] and NRMBPT calculations [Saf02] (also photon energies). QD represents the satellite intensity factor including the statistics weights and is given in 10^{13}/sec (NRMBPT). The labels (p,o,...) are the commonly used.

Label	**Level**	**$MCDF_M$**	**NRMBPT**		
		Resonance (keV)	**Resonance** (keV)	**X-ray** (keV)	**QD**
p	$1s2s^2\ ^2S_{1/2}$ - $1s^22p\ ^2P_{1/2}$	8.823	8.8222	12.8590	5.44
o	$1s2s^2\ ^2S_{1/2}$ - $1s^22p\ ^2P_{3/2}$		8.8222	12.7968	2.52
t	$1s2s(^1S)2p\ ^2P_{1/2}$ - $1s^22s\ ^2S_{1/2}$	8.9697	8.9683	13.0775	12.1
r	$1s2s(^3S)2p\ ^2P_{1/2}$ - $1s^22s\ ^2S_{1/2}$	8.9008	8.9026	13.0119	10.8
s	$1s2s(^3S)2p\ ^2P_{3/2}$ - $1s^22s\ ^2S_{1/2}$	8.9766	8.9768	13.0861	12.7
q	$1s2s(^1S)2p\ ^2P_{3/2}$ - $1s^22s\ ^2S_{1/2}$	8.9479	8.9472	13.0565	1.82
	$1s2s2p\ ^4P_{1/2}$ - $1s^22s\ ^2S_{1/2}$	8.8405	8.8432	12.9525	0.07
	$1s2s2p\ ^4P_{3/2}$ - $1s^22s\ ^2S_{1/2}$	8.8501	8.8526	12.9619	1.71
	$1s2s2p\ ^4P_{5/2}$ - $1s^22s\ ^2S_{1/2}$	8.9036	8.9036	13.0129	0.00
m	$1s2p^2\ ^2S_{1/2}$ - $1s^22p\ ^2P_{3/2}$	9.1061	9.1034	13.0780	7.22
	$1s2p^2\ ^2P_{1/2}$ - $1s^22p\ ^2P_{1/2}$	9.0084	9.0095	13.0464	0.16
a	$1s2p^2\ ^2P_{3/2}$ - $1s^22p\ ^2P_{3/2}$	9.0841	9.0817	13.0563	22.6
	$1s2p^2\ ^4P_{1/2}$ - $1s^22p\ ^2P_{1/2}$	8.9353	8.9370	12.9738	0.42
f	$1s2p^2\ ^4P_{3/2}$ - $1s^22p\ ^2P_{3/2}$	8.9799	8.9812	12.9558	0.9
e	$1s2p^2\ ^4P_{5/2}$ - $1s^22p\ ^2P_{3/2}$	8.9918	8.9925	12.9672	39.9
k	$1s2p^2\ ^2D_{3/2}$ - $1s^22p\ ^2P_{1/2}$	9.0146	9.0149	13.0519	38.1
l	$1s2p^2\ ^2D_{3/2}$ - $1s^22p\ ^2P_{3/2}$	9.0146	9.0149	12.9896	8.88
j	$1s2p^2\ ^2D_{5/2}$ - $1s^22p\ ^2P_{3/2}$	9.0599	9.0576	13.0322	54.4

Table 2.6 displays the results obtained through extrapolation to zero electron beam current (Fig. 2.31), and the experimental resonance widths (Gaussian) in comparison with the two calculations. As the observed $1s2s^2$ and $1s2s2p$ configurations in good approximation consist of a single resonance each, the experimental width is understood to reflect the intrinsic electron energy spread. The third configuration ($1s2p^2$) is broader, due to several blended resonances it contains.

The absolute experimental resonance energies are consistently shifted by about

Table 2.6: Absolute KLL resonance energies of He-like Kr^{34+} in comparison with theoretical (NRMBPT) and $MCDF_M$ calculations, respectively. The numbers in brackets for the experimental data represent statistical and systematic uncertainties.

State	**Transition**	**Width** (eV)	**Experiment** (eV)	**MCDF$_M$** (eV)	**NRMBPT** (eV)
$1s2s^2$	p, o	36.8 (0.7)	8792.3 (1.1)	8823.1	8822.2
$1s2s2p$	r	36.1 (0.4)	8868.2 (1.1)	8900.8	8902.6
$1s2p^2$	t, s, q, f, e, a, k, l	55.1 (0.4)	8964.8 (1.4)	8997.9	8996.6

30 eV. The $1s2p^2$ would move to lower energies if the resonance $1s2s^22p$ (Li-like) nearby line would be taken into account. In fact, in Ref. [FBR 98] it was already shown that a weak Li-like peak overlaps with the He-like peak arising from the $1s2p^2$ states (see Fig. 2.30). The almost perfect linearity of the electron current-space charge shift in the range between 100 mA to 20 mA does not suggest a non-linearity of the ionic space charge compensation, which could explain the discrepancy. As of now, we have no consistent explanation for the observed discrepancy, which certainly will be subject of further investigations that have not been possible within the present work. However, differences up to 1.8 eV between the predictions of both calculations along with an experimental extrapolation uncertainty of only 1 eV strongly support the expectation that DR measurements in the EBIT might be able to reach an absolute precision sufficient to sensitively test predictions of state-of-the-art theories

The analysis of the differences between the resonance excitation energies obtained in the experiment allows, however, to accurately compare experimental and theoretical data. They are presented in Table 2.7 together with the calculated values (NRMBPT and $MCDF_M$), and were obtained by using different methods. First, this table displays the results extrapolated using the resonance position as a function of the electron beam current plot (Fig. 2.31) by fitting linear and parabolic functions, respectively. In some cases, the same slope was fitted simultaneously to the three data sets. The extrapolated resonance positions resulting from the parabolic fit agree with those obtained by the expected linear function; however, their error bars are substantially larger. The table also shows the results obtained by averaging the differences between the peak centroids at each electron beam current. Since the extrapolation uses an additional parameter, B (the slope), larger error bars are expected here in comparison to the direct method because of the increased number of degrees of freedom.

Table 2.7: Differences between resonance energies. B- and C-shared indicate that these parameters ($y = A + Bx + Cx^2$) were forced to be the same in the fits to the three data sets in Fig. 2.31. "I_e & averaged" indicates the method in which the differences are obtained at each electron beam current and later averaged.

Method	$1s2p^2 - 1s2s2p$ (eV)	$1s2s2p - 1s2s^2$ (eV)
Line B-free	96.6 (1.8)	75.9 (1.6)
Parabola B-, C-free	96.2 (5.6)	78.5 (5.1)
Line B-shared, $B = 1.13 \pm 0.02$	96.6 (2.3)	75.2 (2.1)
Parabola B-shared, $B = 0.89 \pm 0.13$	96.6 (6.3)	75.3 (5.4)
C-shared, $C = 0.002 \pm 0.001$		
	96.6 (1.3)	75.8 (1.2)
I_e & averaged	96.7 (0.7)	75.4 (0.6)
NRMBPT	94.0	80.4
$MCDF_M$	97.1	77.7

Given that the predictions of both theories display discrepancies of 2.7 and 3.1 eV for the two values, respectively, and our experimental data deviates at most by 0.1 and 0.5 eV for the same values respectively, these results clearly demonstrate the potential of DR measurements in an EBIT for precision spectroscopy of HCI.

Moreover, the similarity between the measurements shown here and those carried out at the Berlin EBIT [FBR 98] along the different ion charge states is striking (see Fig. 2.26). The resonance energy differences obtained in these measurements resulted in almost identical values to those presented here, although the experimental technique used there was a different one in which the scan velocity was much higher to reduce instantaneous changes in the charge balance to a minimum. This convincingly underlines the reproducibility of the photorecombination results obtained with different EBITs.

2.6.4 X-ray energy measurements

As mentioned above, the two-dimensional plot (Fig. 2.37) also allows one to project selected regions onto the x-ray energy axis at a particular electron energy. Thereby, the energy of the x-ray emitted in the radiative stabilization of the intermediate excited states during the DR process can be determined as well, even though the resolution of the germanium detector is substantially poorer. The left plot in Fig. 2.37

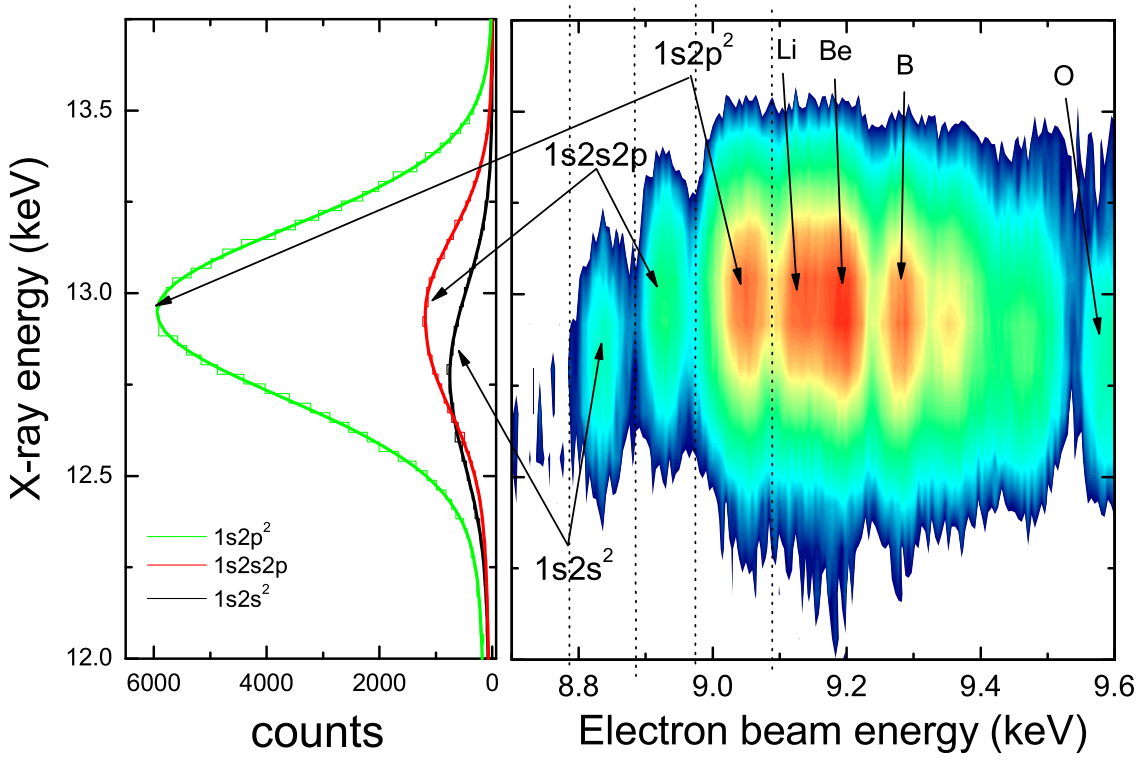

Figure 2.37: The left-hand part of the picture shows the projected electron energy regions (in between the vertical dotted lines in the right-hand picture) onto the x-ray energy axis for the He-like KLL DR resonances.

shows different projections (dashed lines in the right-hand side).

The resolution of the x-ray detector used in this experiment (FWHM $\approx 580 \pm 2$ eV at 14.4 keV) did not allow to resolve all the different decay paths of the doubly excited states formed in DR. Therefore, as it can be seen in Fig. 2.37, we observe only a single composite peak at each projected region.

The first projection corresponds to the $1s2s^2\ ^2S_{1/2}$ state, whose decay to the ground state is forbidden by the dipole selection rules ($\Delta l = 0$). However, this state can radiatively decay either through two-photon emission or, more predominantly, through the so-called two-electron-one-photon transition (TEOP), either to the $1s^22p\ ^2P_{1/2}$ or to the $1s^22p\ ^2P_{3/2}$ state. A detailed analysis of this type of transition in Ar^{16+} can be found in Ref. [ZCU03]). The other two peaks are due to the $1s2s2p$ and $1s2p^2$ configurations, which can decay to the ground state through different dipole-allowed channels (see Table 2.5).

Although the apparent energies of the DR resonances change with the electron beam current due to the space charge potential, the photon energies do not vary,

which was proved by determining their energies at different electron beam currents.

The calibration of the photon energy axis on the germanium detector was carried out with two radioactive sources, namely, ^{57}Co and ^{241}Am. These sources provide several calibration lines in the energy range from 4 to 25 keV. In particular, the cobalt source has a strong line at 14 keV, conveniently close to the observed krypton K_α lines. Table 2.8 summarizes their values. Figure 2.38 shows the calibration spectra. The line profiles were fitted with Gaussian functions, as well as with the two different non-symmetric distributions described in subsection 2.4.1 (see also Eqs. (2.31) and (2.32)), to determine their positions. The resulting data points were fitted to a linear function to obtain the conversion factor. The quality of this fit is extremely good, as apparent from the regression coefficient R^2.

Table 2.8: Cobalt and americium lines used for the Ge-detector calibration (see *e.g.* [Nuc05]).

^{57}Co (keV)	^{241}Am (keV)
4.508*	9.4423
6.398**	13.9441
14.4129	16.84
	17.7502
	26.3448
* Ge scape peak	
** Fe K_α	

Unfortunately, the calibration for the first set of data (Exp.1) was not carried out simultaneously with the experiment. An unquantifiable shift of the ADC gain occurred between measurement and calibration. Therefore, the results have a very large systematic error (for the absolute energy), while the x-ray energy differences are good to $\pm$ 2% of their value. This part of the experiment was repeated later (Exp.2), and calibrations were alternated with the data acquisition.

In Fig. 2.39, the results of the x-ray energies for the different transitions are displayed. The dotted vertical lines separate the three types of functions used for the fitting procedure, both for these lines and for the calibration lines. The scattering of the data points is consistent with the uncertainties of the fit functions. When the data is fitted with the function given in [Wid98] (Eq. (2.31)), smaller uncertainties are obtained. Larger error bars are observed when the data points are fitted with the function from Eq. (2.32) given in [CMH 01]. These are, most likely, due to

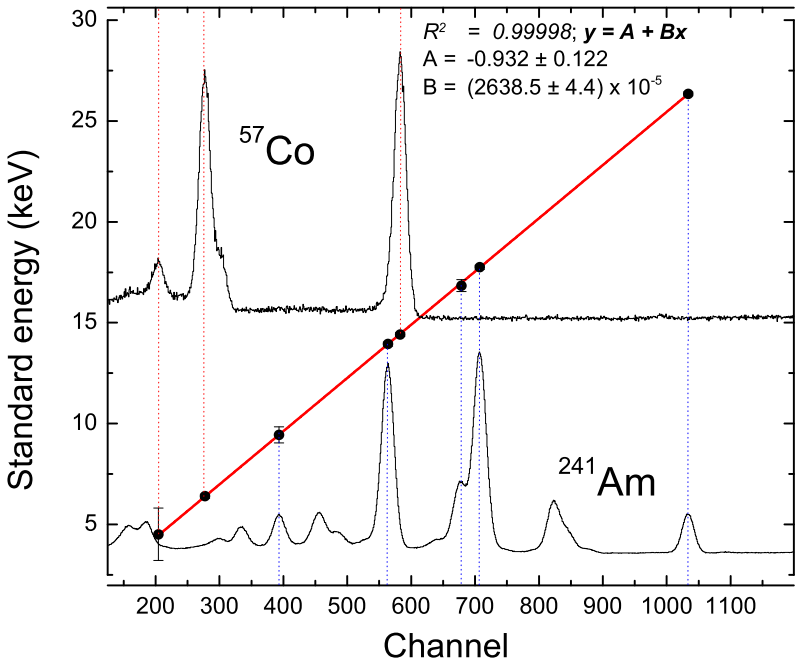

Figure 2.38: Calibration lines and fit used for the Ge-detector channel-energy conversion. The upper spectrum corresponds to a cobalt source (^{57}Co) and the lower to an americium source (^{241}Am).

the larger number of free parameters used. Finally, peaks fitted with a Gaussian function have also large error bars due to inappropriate fit area selection. Actually, the non-symmetric profile of the peaks, intrinsic to any solid state detector, does not allow to use a Gaussian profile over the whole peak distribution, but only (to a good approximation) around the symmetric high-energy parts of the peak.

A weighted average of these data points was obtained (Fig. 2.39). The measured widths of the x-ray peaks seem to be limited by the detector resolution itself. The two less intense peaks observed at lower x-ray energies ($1s2s^2$ and $1s2s2p$) have a Gaussian width of about 440 eV, while the peak at the highest energy has a slightly larger width of 460 eV due to the blend of a number of transitions. Table 2.9 summarizes the results.

The experimentally determined transition energies show consistently values which are too low by 70 to 80 eV in comparison with theory and earlier experimental data taken with crystal x-ray detectors. We infer that the radiative recombination photons from Li-, Be-, and B-like ions, which have slightly lower energies at a given acceleration voltage than the photons due to RR of He-like krypton ions, are the cause of this shift (see Fig. 2.40). As one can see in Fig. 2.28, the radiative

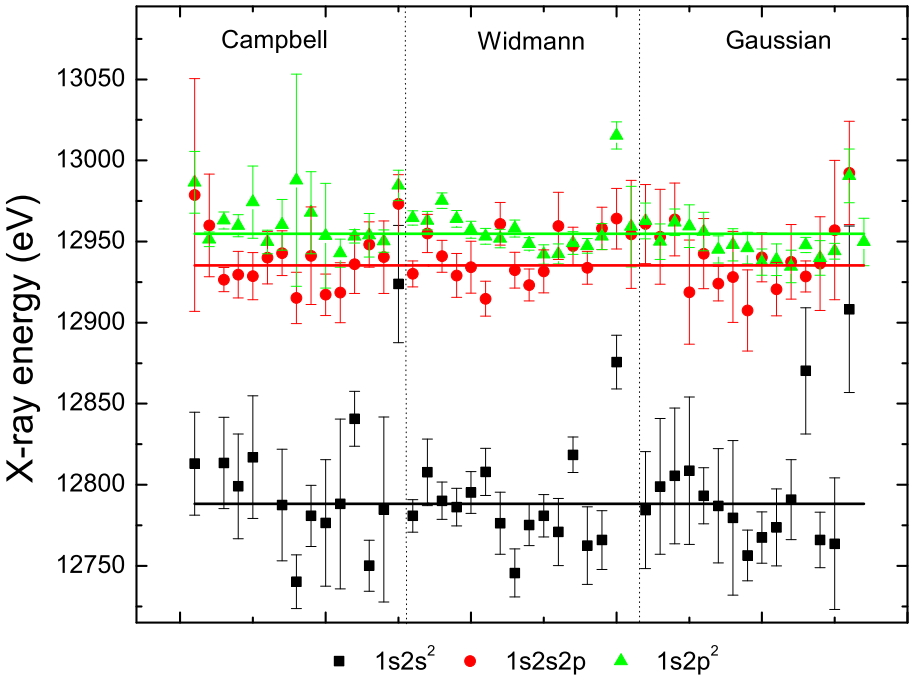

Figure 2.39: Plot of the results (Exp.1) for the x-ray transitions from the indicated doubly excited He-like krypton ions. The three sections indicate the type of function used for the fit (compare with Eqs. (2.31) and (2.32)).

Table 2.9: Experimental and calculated (NRMBPT) photon energies for the three He-like DR resonances. The third column shows the measured x-ray resonance width. The error margins displayed for Exp.1 are only the statistical. Exp.2 includes the systematic and statistical errors.

Configuration	**Transition**	**Width** (eV)	**Exp.1** (eV)	**Exp.2** (eV)	**NRMBPT** (eV)
$1s2s^2 \rightarrow 1s^2 2p$	p, o	444.7(4.1)	12788.2(2.9)	12771.3(3.3)	12839.6
$1s2s2p \rightarrow 1s^2 2s$	r	436.2(3.2)	12935.3(2.1)	12943.8(14.7)	13011.9
$1s2p^2 \rightarrow 1s^2 2p$	t, s, q, f, e, a, k, l	460(1)	12954.8(1.8)	12918.7(11.8)	13007.8

recombination at about 8.5 keV has a photon yield which is about half the size of the $1s2s^2$ DR resonance. Very similar data from Fuchs [FBR 98] indicate that the He-like ions are about 25% of the total population, Li-like 30%, Be-like 22% and B-like 14%. The correspoding ionization potentials are 136.4 eV, 376.5 eV and 530.9 eV, lower than the He-like one, respectively. Unfortunately, the detector resolution is not sufficient to resolve the blend of photon energies caused by RR of these various ions. The fit shows a shift of about 60 eV in the right direction under these conditions. As we will see later, with heavier ions, the x-ray energy resolution

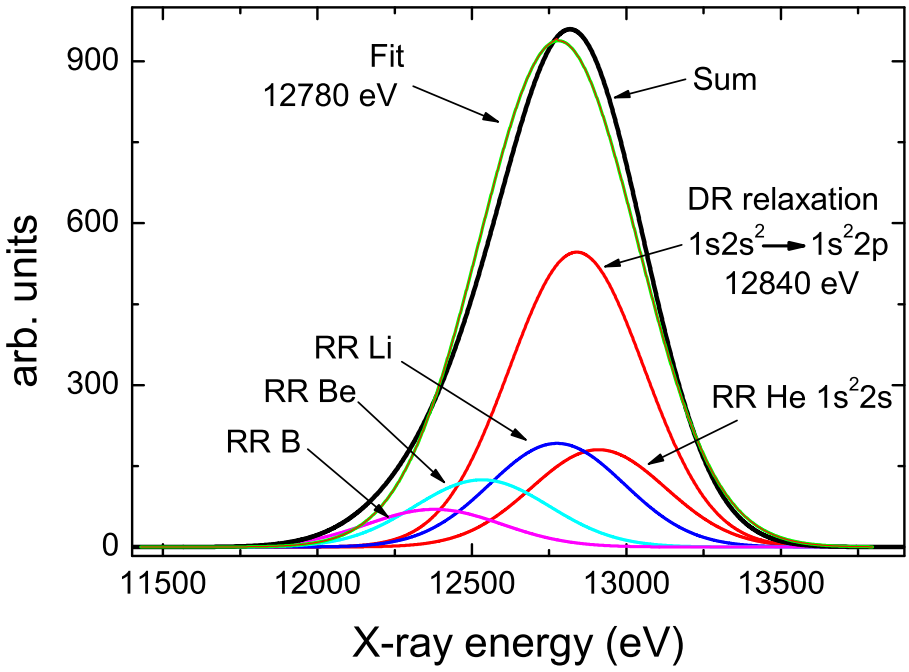

Figure 2.40: Deviation of the theoretical (NRMBPT) DR He-like $1s2s^2$ (red curve) peak centroid due to the presence of the radiative recombination lines of different charge states. The black curve shows the sum of all contributions and the green one the fit.

will be sufficient to separate the different higher charge states in the RR band, thus avoiding this problem.

Table 2.10 displays the differences between the measured x-ray energies, which allows direct comparison with the predictions. However, the influence of the RR bands also affects, if less, these results.

These data show that calibrations are needed more frequently and that the effect of RR has to be avoided by increasing the resolution to a level better than the ionization potential separation. With these caveats, DR measurements can provide qualitative data for the energetic x-ray transitions in the range beyond 10 keV, where crystal spectrometers have low efficiencies and resolution limitations.

Table 2.10: Differences for x-ray energies.

Peak labels	Exp.1 (eV)	Exp.2 (eV)	NRMBPT (eV)
$1s2p^2 \rightarrow 1s^22p$ - $1s2s2p \rightarrow 1s^22s$	19.5 (2.8)	-25.1 (18.9)	-4.1
$1s2s2p \rightarrow 1s^22s$ - $1s2s^2 \rightarrow 1s^22p$	147.1 (3.6)	172.5 (15.1)	172.3

Chapter 3

Results and discussion

This section describes the results of an experiment dedicated to the photorecombination of mercury ions from Hg^{78+} (He-like) to Hg^{75+} (B-like). Mercury ranks fourth among the heaviest stable elements. Its K_α transitions have energies of about 70 keV, quite close to the 100 keV of uranium. Other-Z dependent effects, such as the Lamb shift, are also close in magnitude to the uranium case. For these reasons, it was selected for the present work. The data presented here are the first state-selective measurements for deep lying KLL resonances of very highly-charged heavy ions.

3.1 Photorecombination of $Hg^{75+...78+}$ ions

In this experiment, the EBIT was used to measure the resonance energies and the level splittings of several (doubly) excited states, especially $2l2l'$ configurations, of few-electron mercury ions ($Hg^{78+...75+}$) formed through dielectronic resonances. As in the case of the krypton test experiments (see section 2.6), the energy of the photons emitted from the resonantly excited states has been determined as well, but with improved accuracy. In addition to the measurement of the exact resonance and photon energies, the interference between the two photorecombination processes, RR and DR, has been observed for the first time and precisely characterized for well defined states through the Fano parameters [GCB 05, KBC 95].

In order to inject mercury as an atomic beam into the EBIT, a few mercury drops were introduced in an evacuated glass vial which was connected to the needle valve in the gas injection system port. The evaporation of mercury at room temperatures (10^{-4} Torr) [Win03] delivered sufficient neutral mercury atoms through the differential pumping stages into the trap region.

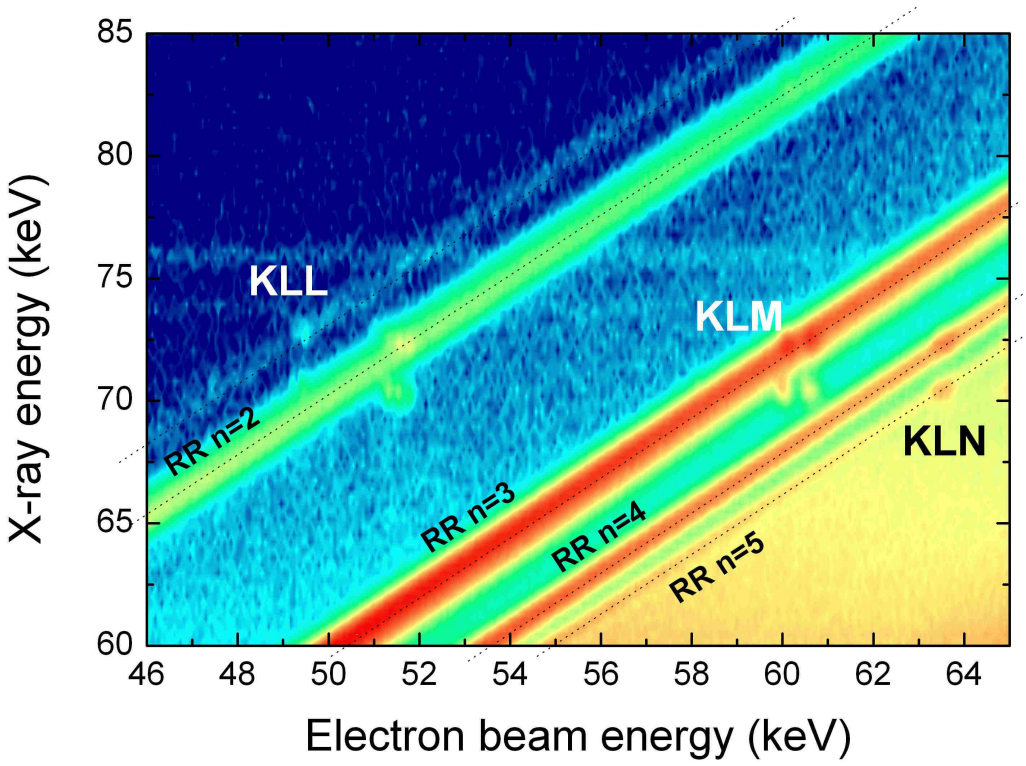

Figure 3.1: Logarithmic 2D contour-map of the photorecombination (x-ray intensities) of highly charged mercury ions. The diagonal lines correspond to RR processes into $n = 2$, 3, 4 and 5. The clusters containing a number of bright spots are due to DR resonances.

At first, the electron beam energy was scanned over a broad range from 45 to 70 keV in a saw-tooth profile as shown in Fig. 3.1 in order to gain an overview from below the resonances up to nearly the direct excitation region. We used a scan speed of roughly 100 V/s at a constant electron beam current of about 180 mA. Later, a smaller region was chosen and scanned in more detail and with better statistics. Here, the electron beam energy was scanned very slowly (37 V/s) across the KLL resonances in the energy range from 45 to 54 keV (see Fig. 3.2). This experiment was performed with an electron beam current of 160 mA. In contrast to the krypton test experiment, a higher magnetic field of 8 T was used. Since mercury was the heaviest element inside the trap and lighter impurity ions do not accumulate excessively due to their higher evaporation probability and in addition to the fact that ionization times become longer, a long dumping time of 5 min was set. The voltage applied to the drift tube electrodes next to the central drift (trapping) tube was set to + 2.5 kV. This high potential allowed to efficiently trap highly charge mercury ions, and use at the same time the lighter impurity ions for evaporative cooling. The vacuum pressure at the top of the superconducting magnet cryostat

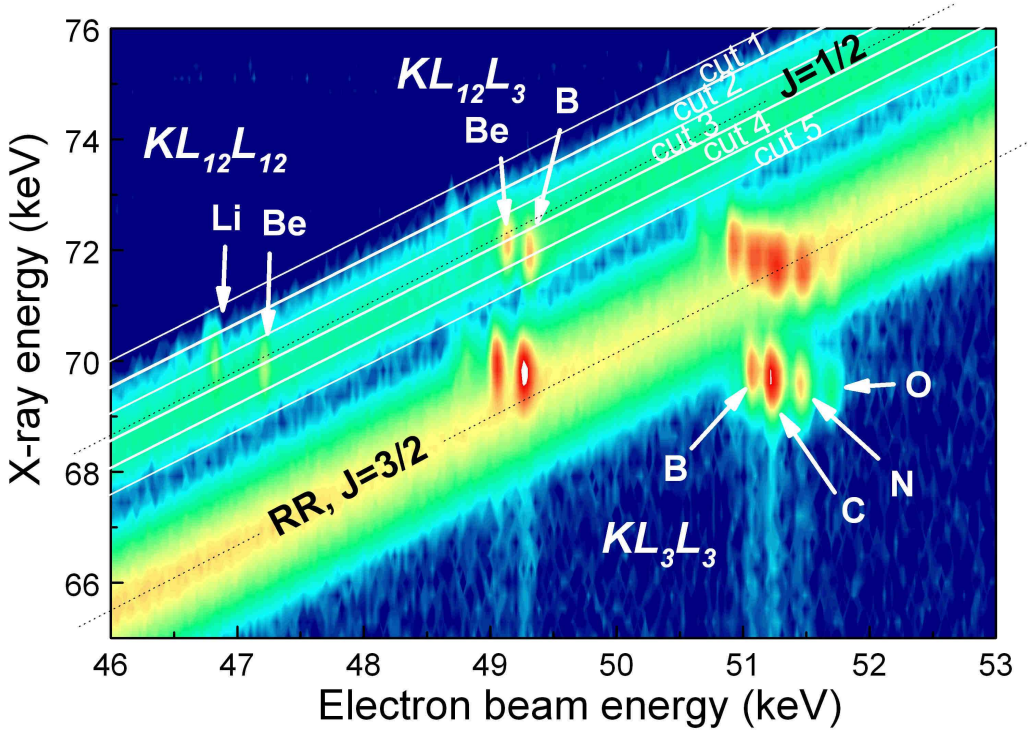

Figure 3.2: Logarithmic 2D contour-map of the photorecombination of highly charged mercury ions in the DR KLL region (accumulated for 100 hrs.). The two diagonal bands correspond to RR ($n = 2$) processes; the upper band into $J = 1/2$ ($2s_{1/2}$ and $2p_{1/2}$) and the lower into $J = 3/2$ ($2p_{3/2}$) states. The energy difference between these bands is larger than 2 keV. DR resonances are visible as bright spots. Here, the areas enclosed by white frames in the upper RR band ($J = 1/2$) are thin cuts whose projections are described below (for details see text). The count rates of x-rays due to RR processes into $n = 2$, $J = 3/2$ states was about 8 counts-per-second (cps) while those into states with $J = 1/2$ was 2 cps.

was about $2{\times}10^{-10}$ Torr during the experiment.

At first glance the KLL DR region in Fig. 3.1 might seem to be nearly structureless; however, a high resolution mapping clearly shows a series of pronounced structures in Fig. 3.2. Here, strong x-ray yields are concentrated on five clusters of horizontally aligned bright spots which are due to DR resonances of mercury ions with open L-shell. Using the nomenclature introduced in Ref. [KBC 95], they are labeled $KL_{12}L_{12}$ (left one), $KL_{12}L_3$ (two central clusters) and KL_3L_3 (two right clusters). Four of the clusters strongly overlap with the RR bands. For an initial He-like state they represent the DR into the final states $KL_{J=1/2}L_{J=1/2}$ ($1s2s^2$, $1s2s2p_{1/2}$, $1s2p_{1/2}2p_{1/2}$), $KL_{J=1/2}L_{J=3/2}$ ($1s2s2p_{3/2}$, $1s2p_{1/2}2p_{3/2}$) and $KL_{J=3/2}L_{J=3/2}$ ($1s2p_{3/2}2p_{3/2}$), respectively. These denominations are also used for other charge states in an analogous way. In fact, the grouping of the bright spots for a given clus-

ter at similar x-ray energies forming horizontal bands reflects similar deexcitation energies for different charge states. As indicate in the figure, lower charge states occur at higher electron beam energy, since the binding energy available through the recombination is smaller for those ions.

Some other x-ray features can be seen in Fig. 3.2. A few vertical lines with broad x-ray energy distribution at well defined electron energies "falling down" from some DR resonances are due two-photon decay channels [DVD69]. Those are very interesting by themselves, however, were not in the focus of the present work since there x-ray continua are hard to study due to the lack of sufficient counting statistics and also of precise theoretical predictions for many-electron ions [SDK 69, KAB93].

Furthermore, two feeble x-ray lines observed near 73 and 75 keV which are independent of the electron energy, thus forming bands in the 2D plot, are identified as the K_{α_1} and K_{α_2} transitions of lead, which are either excited by high-energy cosmic radiation and or by natural radioactivity in the lead block shielding of the Ge-detector. The data were corrected for these weak background sources without observing significant changes on the projections discussed below.

The following subsections contain a detailed description of the analysis of the resonance excitation and x-ray energies for charge states ranging from He-like (Hg^{78+}) to B-like (Hg^{75+}) mercury ions. The analysis is performed in an analogous way as in the krypton test experiment.

3.1.1 State selectivity and line shapes

Projections of narrow slices, cut out of the diagonal RR features (see Fig. 3.2) onto the electron beam energy axis allow one to study the resonances for ions in a specific charge state, because the photon energies on the different slices of each RR band correspond to different ion charge states according to their ionization potentials (see Table 3.1). Each slice is about 480 eV broad (in vertical direction). The central x-ray energy of these slices (see Fig. 3.3) is equal to $E_\gamma = E_{beam} + I_x$ and I_x is chosen to a value near the ionization potential I_p of a particular charge state. In some cases, the value I_x was shifted from the ionization potential to reduce the influence of strong resonances from neighboring charge states, at the cost of somewhat reduced statistics. For example, the upper slice of the RR $n = 2$, $J = 1/2$ band contains RR photons from the He-like ion charge state and also a fraction arising from Li-like ions (see Fig. 3.3, cut 1 and later Fig. 3.8a for a detailed description). In contrast, in cut 3 a strong Be-like peak with a very weak contribution from a Li-like resonance is observed (see Fig. 3.8b)). The lowest slice, cut 5 of this band, includes almost

exclusively photons from the B-like ions (projection on Fig. 3.9b). The plots shown in Figs. 3.3 and 3.4 correspond to cuts taken along the RR $n = 2$, $J = 1/2$ and $J = 3/2$ band, respectively.

Table 3.1: Ionization potentials of the highest charge states of mercury ions present in the trap [Sco03].

Charge state	**Configuration**	**Ionization potential** (keV)
77	$1s^2 2s$	23.5444
76	$1s^2 2s^2$	23.1807
75	$1s^2 2s^2 2p$	22.5826
74	$1s^2 2s^2 2p^2$	22.1659
73	$1s^2 2s^2 2p^3$	19.6669
72	$1s^2 2s^2 2p^4$	19.3036
71	$1s^2 2s^2 2p^5$	18.9413
70	$1s^2 2s^2 2p^6$	18.5553

All the observed resonances were fitted with the following asymmetric Fano profile [SKM 02] caused by the interference between DR and RR, as described in section 1.2.3:

$$F(E_e) = \frac{A}{Q^2\Gamma_d}\frac{2}{\pi}\left[\frac{(\epsilon+Q)^2}{\epsilon^2+1}-1\right], \quad \text{with} \quad \epsilon = \frac{2\cdot(E_e-E_r)}{\Gamma_d}. \tag{3.1}$$

Here, Q is the Fano factor, A defines the total peak area and Γ_d is the natural width of the resonance. E_e and E_r are the incoming electron and the resonance energy, respectively. For large values of Q the function in Eq. (3.1) converges to a Lorentzian, while small Q values indicate stronger asymmetry.

To account for the electron energy spread, the theoretical Fano profile is convoluted with a normalized Gaussian distribution. This convolution containing the experimental FWHM (ω_{exp}) results in

$$Y(E_e) = \frac{2\,A}{\omega_{exp}}\sqrt{\frac{\ln 2}{\pi}}\left[\left(1-\frac{1}{Q^2}\right)\mathbf{R}[\omega(z)] - \frac{2}{Q}\,\mathbf{Im}[\omega(z)]\right], \qquad (3.2)$$

$$z = \frac{\sqrt{\ln 2}}{\omega_{exp}}\left[2\,(E_r - E_e) + i\,\Gamma_d\right].$$

Equation (3.2), which was used for each electronic state, includes the real and imaginary parts of the so-called complex error function $\omega(z)$. These terms were obtained using an algorithm given by Humlicek [Hum78], who treated the convolution

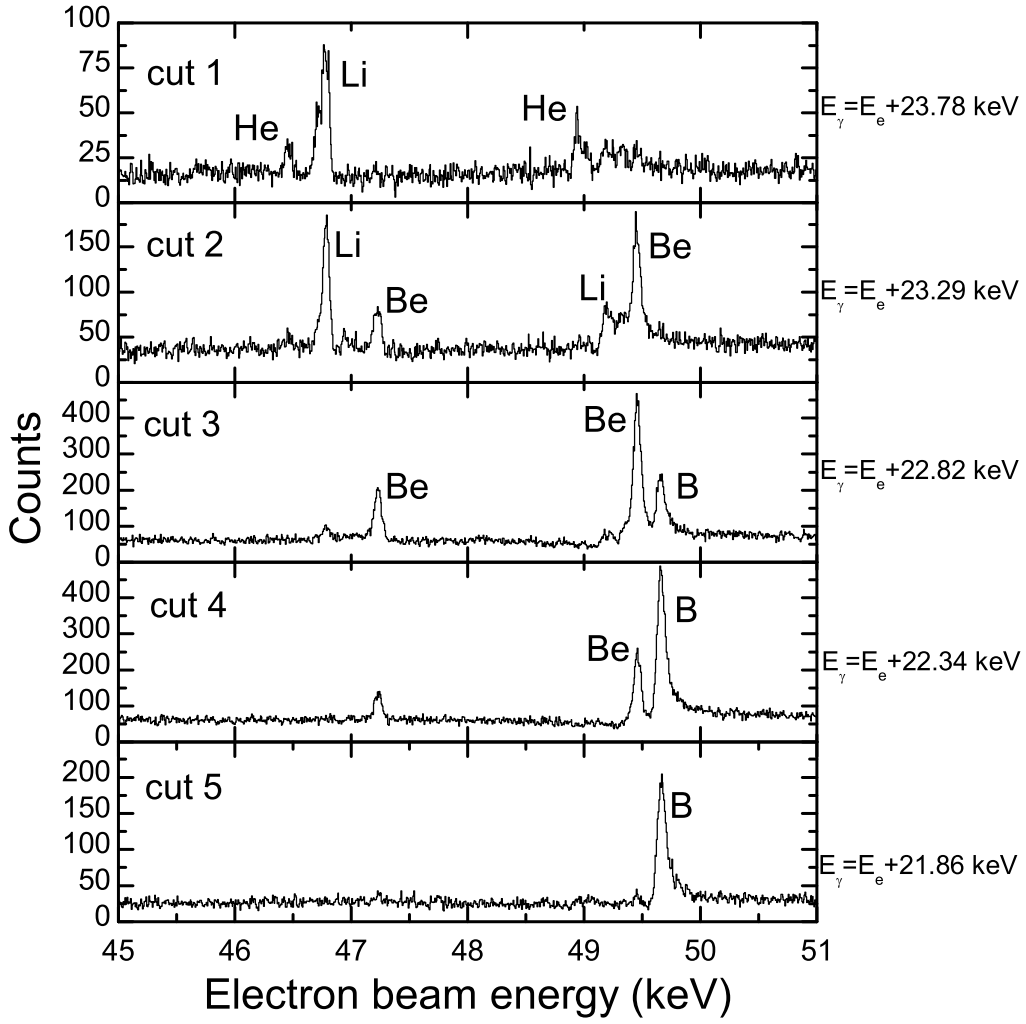

Figure 3.3: Projections of the slices along the RR $n = 2$, $J = 1/2$ band. E_γ and E_e are the photon and electron beam energies in keV, respectively. For assignment of the observed peaks, see Figs. 3.8 to 3.10.

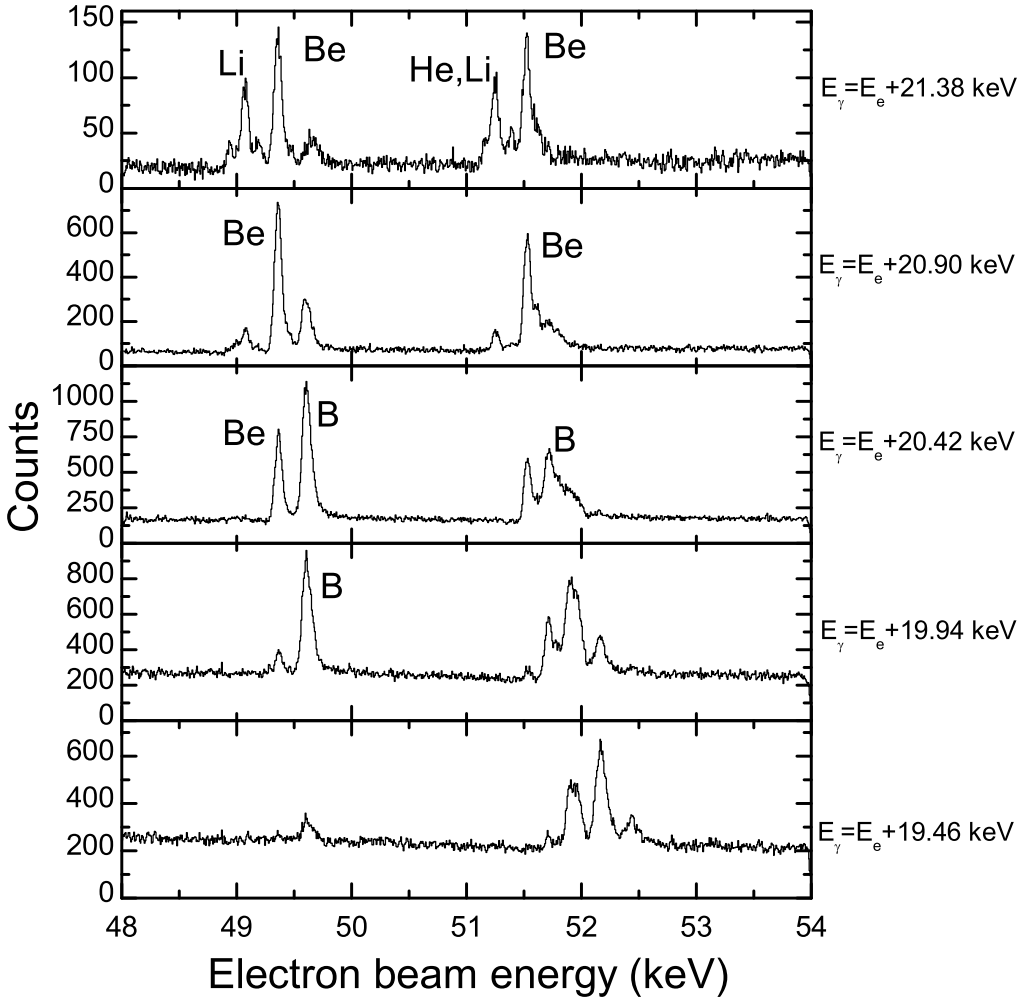

Figure 3.4: Projections of the slices along the RR $n = 2$, $J = 3/2$ band. E_γ and E_e are the photon and electron beam energies in keV, respectively.

of a Lorentzian type function with a Gaussian profile. The result of this type of convoluted profile is commonly known as a Voigt distribution. For very large Q values (symmetric profiles), $Y(E_e)$ approaches the Voigt shape. In a few cases, the resonance profiles could be fitted with Gaussian or Lorentzian distributions without loosing accuracy because of their high degree of symmetry. The positions of weak resonances are also fitted with Gaussian in order to speed up the fitting procedure, since the statistical error is larger than the shift of the centroid induced by the asymmetry, as for instance, in the Be-like resonance Be_1 (cut 4) shown in Fig. 3.5.

In the present fitting procedure, the natural width Γ_d is the only parameter taken from theory. That means that the resonance energy E_r, its area A, experimental

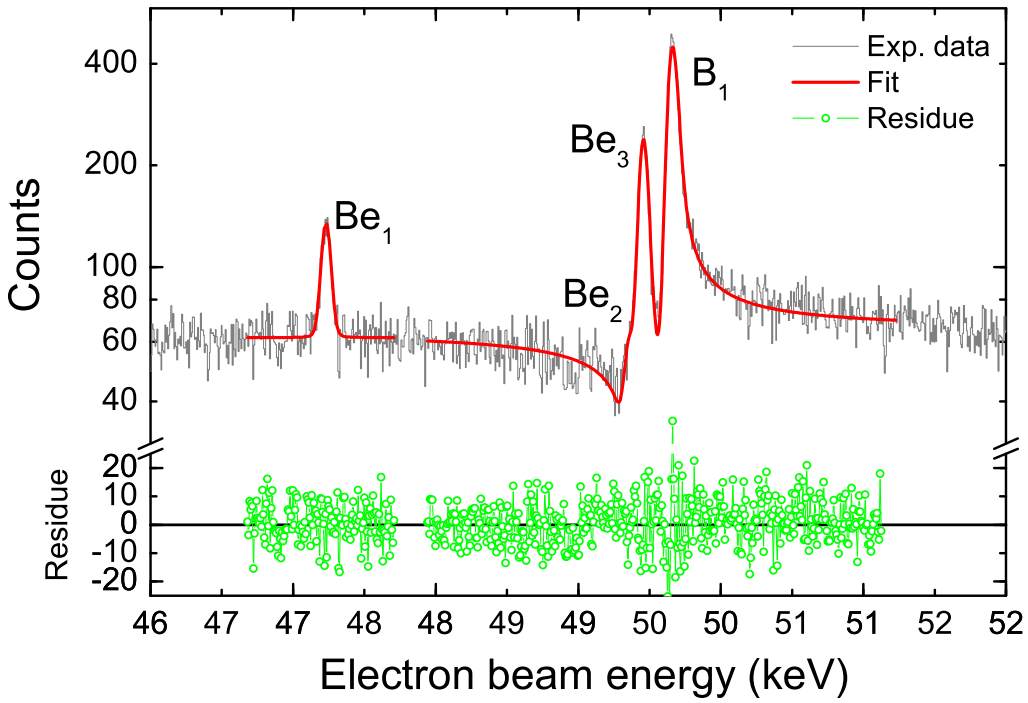

Figure 3.5: One of the slices (cut 4) along the RR $n = 2$, $J = 1/2$ band contains contributions from Be- and B-like ions (top part). The weak Be_1 resonance was best fitted with a symmetric type function, while the strong Be_3 and B_1 resonances at higher energies were fitted with the asymmetric function (3.2). For the labeling of the resonances see Tables 3.4 and 3.5.

width ω_{exp} and Fano factor Q are free parameters. The analysis results in an experimental Gaussian width of about 60 eV at 50 keV electron beam energy, corresponding to a relative resolution $\Delta E/E \approx 1/1000$. The fit quality was evaluated with the χ^2 over degrees-of-freedom (DoF) method. For instance, we obtained for the projection of the $KL_{12}L_3$, containing the B- and Be-like resonances (see Fig. 3.5) in the $J = 1/2$ band, from the Lorentzian fit a χ^2/DoF of 3.8 whereas a Fano fit resulted in a much better χ^2/DoF of 0.8 .

3.1.2 Excitation energies

In the present experiment the electron gun platform was negatively biased due to the required high electron beam energy. As described in detail before (see section 2.3.3), the voltage applied to this platform ($V_{Platform}$) was measured with the *platform* voltage divider and the high voltage on the drift tube rack (V_{DT}) by means of the *drift tube* voltage divider. The absolute resonance energies are determined by adding three more terms to Eq. (2.23) which account for the space charge potential due to

the electron beam, its compensation by the fraction f of positive ions (see section 2.3.2) and the electrodes work functions $\Phi = -2.65$ eV:

$$E_{resonance} = -V_{cathode} - V_{Platform} + V_{DT} + V_{sp}(1 - f) + \Phi\,, \tag{3.3}$$

where $V_{cathode}$ is the negative cathode voltage.

The negative space charge potential V_{sp} is estimated using the formula (Eq. (2.20)). At 160 mA electron current and 46 kV acceleration voltage, it reduces the beam energy by 142 eV. This number is obtained with an electron beam radius $r_e = 23$ μm. In order to evaluate the effect of the positive space charge compensation due to the trap ions, we have compared the present experiment with the krypton. The mercury injection pressure was lower, and the ion breeding times are longer. A smaller amount of trapped ions will result from such operation parameters, and the space charge compensation will be reduced. For krypton, a 38% of ion compensation was determined. Thus, we have conservativelly estimated the ion fraction to be $f = (30 \pm 10)\%$, which yields a total space charge potential of -99 ± 14 eV. A much more reliable result for the space charge compensation could have been extracted from a zero current extrapolation.

The space charge potential is a function of the electron density, and hence of the electron velocity, and thus, varies slightly over the scanned energy region. The amount determined for the $1s2s^2$ $KL_{12}L_{12}$ resonance (99 eV) was scaled with the electron energy as ${E_e}^{-1/2}$ since the electron beam current is constant. Then, on average, the $KL_{12}L_3$ resonances are shifted by 97 eV and the KL_3L_3 by 95 eV.

It is important to emphasize that the experimental absolute electron energy scale determined in this way has a systematic error of $\pm$ 14 eV. Comparing the result of 46.358 eV $\pm$ 4 eV (statistical) $\pm$ 14 eV (systematic) for the $1s2s^2$ state, which has a nearly symmetric shape, with the various theoretical excitation energies in Table 3.2 one finds it in excellent agreement with all predictions.

The total uncertainty of the energy scale can be further reduced down to $\pm$ 4 eV, by using the theoretical value of the He-like $1s2s^2$ excitation energy of 46.358 keV ($MCDF_S$, see below) as the reference. He-like calculations are supposed to be the most reliable ones, and show the smallest spread across the various models of less than 7 eV for all the resonances, and less than 3 eV for the $1s2s^2$ state (Table 3.2). Thus, using a single theoretical reference, a relative energy scale spanning more than 5 keV (at 50 keV), valid for all ionization stages discussed here can be established in addition to the absolute energy scale explained above.

Tables 3.2 to 3.5 show the comprehensive results obtained for the He- to B-like charge states in comparison with calculations carried out with four different methodes. In the following, some more detailed information concerning these predictions is provided.

Table 3.2: Measured and theoretical DR resonance energies for the singly and doubly excited states $|d\rangle$ of He-like mercury (Hg^{78+}) ions. The He_1 resonance is used as reference for the absolute energy scale by adjusting its value to the $MCDF_S$ prediction (see text). The state $(1s2s)_0 2p_{3/2}$, $J = 3/2$ has two allowed radiative decay channels which are designated with two different labels, He_3 and He_5.

$\|d\rangle$	**J**	**Label**	**Exp.** (keV)	**MCDF**$_S$ (keV)	**CI-DFS** (keV)	**QMB** (keV)	**MCDF**$_M$ (keV)
$\mathbf{1s2s^2}$	1/2	He_1	**46.358(4)**	46.358	46.361	46.359	46.361
$(1s2s)_0 2p_{1/2}$	1/2	He_2	**46.611(6)**	46.613	46.614	46.612	46.614
$(1s2s)_0 2p_{3/2}$	3/2	He_3	**48.844(6)**	48.844	48.842	48.840	48.842
$(1s2p_{1/2})_0 2p_{3/2}$	3/2	He_4	**48.918(9)**	48.923	48.926	48.922	48.928
$(1s2s)_0 2p_{3/2}$	3/2	He_5	**48.845(5)**	48.844	48.842	48.840	48.842
$1s(2p_{3/2})^2$	5/2	He_6	**51.064(6)**	51.065	51.063	51.058	51.063

a) The calculations based upon the Multi-Configuration Dirac-Fock method by Scofield ($MCDF_S$) [Sco03] are analogous to those previously carried out for uranium ions in [KBC 95, Sco89]. They include a multipole expansion for the emitted photon states. It has been found that only the electric dipole and quadrupole contributions are significant. Continuum states are also implemented into the code. There, the DR process is introduced by including the coupling between the continuum states and the doubly excited states. The code includes both the Coulomb and retarded Breit interactions. Admixtures of the doubly excited states to the continuum state are added to the lowest order. The matrix elements for the x-ray emission include both the purely continuum part and sums over the excited bound states. The asymmetry of the lines comes from the cross terms, when the matrix elements are squared to calculate the cross sections.

b) The second calculation (CI-DFS) was performed by Tupitsyn [Tup04] in the Dirac-Hartree-Fock (DF) basis for occupied states and Dirac-Fock-Sturm (DF-Sturm) basis for unoccupied states (see section 1.1.2). Here, the set of the different configurations was generated including all of the single, double and most parts of the triple electronic excitations from the main configuration.

The Breit electron-electron interaction in the Coulomb gauge, the nuclear size

Table 3.3: Measured and theoretical DR energies for the doubly excited states $|d\rangle$ of Li-like mercury (Hg^{77+}) ions.

$\|d\rangle$	**J**	**Label**	**Exp.** (keV)	**MCDF**$_S$ (keV)	**CI-DFS** (keV)	**QMB** (keV)	**MCDF**$_M$ (keV)
$1s2s^22p_{1/2}$	1	Li_1	**46.686(5)**	46.688	46.690	46.686	46.688
$((1s2s)_12p_{1/2})_{3/2}2p_{3/2}$	2	Li_2	**49.086(6)**	49.066	49.068	49.063	49.071
$((1s2s)_12p_{1/2})_{3/2}2p_{3/2}$	1	Li_3	**49.136(9)**	49.116	49.118	49.113	49.121
$((1s2s)_02p_{1/2})_{1/2}2p_{3/2}$	2	Li_4	**49.218(13)**	49.212	49.211	49.209	49.213
$((1s2s)_12p_{1/2})_{3/2}2p_{3/2}$	3	Li_5	**48.970(5)**	48.964	48.967	48.961	48.969
$(1s2s)_1(2p_{3/2})_2{}^2$	3	Li_6	**51.154(5)**	51.150	51.153	51.147	51.155

Table 3.4: Measured and theoretical DR energies for the doubly excited states $|d\rangle$ of Be-like mercury (Hg^{76+}) ions.

$\|d\rangle$	**J**	**Label**	**Exp.** (keV)	**MCDF**$_S$ (keV)	**QMB** (keV)	**MCDF**$_M$ (keV)
$1s2s^2(2p_{1/2})^2$	1/2	Be_1	**47.135(5)**	47.124	47.121	47.132
$(1s2s^22p_{1/2})_12p_{3/2}$	3/2	Be_2	**49.270(8)**	49.248		49.257
$(1s2s^22p_{1/2})_02p_{3/2}$	3/2	Be_3	**49.349(6)**	49.335	49.333	49.344
$(1s2s^22p_{1/2})_12p_{3/2}$	5/2	Be_4	**49.265(17)**	49.244	49.246	49.252
$1s2s^2(2p_{3/2})_2{}^2$	5/2	Be_5	**51.433(6)**	51.425	51.423	51.426

(field shift) and QED corrections were all included in the Hamiltonian, making it difficult to extract individual contributions. To give an idea about the magnitude of

Table 3.5: Measured and theoretical DR energies for the doubly excited states $|d\rangle$ of B-like mercury (Hg^{75+}) ions. The doubly excited state $1s2s^2(2p_{1/2})^22p_{3/2}$, $J = 1$ has two allowed radiative decay channels which are designated with two different labels, B_1 and B_3.

$\|d\rangle$	**J**	**Label**	**Exp.** (keV)	**MCDF**$_S$ (keV)	**QMB** (keV)	**MCDF**$_M$ (keV)
$1s2s^2(2p_{1/2})^22p_{3/2}$	1	B_1	**49.557(4)**	49.549	49.546	49.547
$1s2s^2(2p_{1/2})^22p_{3/2}$	2	B_2	**49.499(4)**	49.491	49.487	49.488
$1s2s^2(2p_{1/2})^22p_{3/2}$	1	B_3	**49.552(7)**	49.549	49.546	49.547
$(1s2s^22p_{1/2})_1(2p_{3/2})^2{}_2$	3	B_4	**51.603(8)**	51.601	51.593	51.598
B_1+B_3		B_{13}	**49.556(4)**	49.549	49.546	49.547

the different QED and nuclear shifts, an additional calculation was performed using perturbation theory (Table 3.6). This table shows how the experimental errors are already small enough to become sensitive to QED contributions to the $2p$ states, and to nuclear size effects of the $2s$ states.

Table 3.6: QED contributions and nuclear size effects per electron performed on the basis of CI-DFS calculations for mercury ions. The estimated uncertainties are indicated in parenthesis.

Effect	**1s**	**2s**	$\mathbf{2p_{1/2}}$	$\mathbf{2p_{3/2}}$
QED contribution	162.5 (2.0)	26.3 (1.0)	2.1 (0.2)	4.2 (0.2)
Nuclear size correction	54.2 (1.0)	8.9 (0.2)	0.5 -	0.2 -

c) The columns labeled QMB are predictions by Artemyev [ASS03]. In zero order approximation, the interelectronic interaction is neglected. In the first order of perturbation theory, QED diagrams of electron-electron one-photon exchange, one-electron self energy and one-electron vacuum polarization are taken into account (see section 1.1.3). In the next order, self energy-screening and vacuum polarization-screening largely cancel each other. The diagram of two-photon exchange is calculated using relativistic many body perturbation theory (RMBPT), because it has been shown that the results differ only in the order of 0.5 eV, compared with the full QED calculations [BMJ93]. For this method an accuracy of 5 eV for a particular energy level has been estimated. However, error bars are not given because a third order perturbation theory would be still needed to determine them properly.

d) The most recent calculations, also based on the Multi-Configuration Dirac-Fock technique (labeled MCDF_M) have been performed in the Theory Department of the Max-Planck-Institut für Kernphysik [HJK05a]. Here, the corrections due to the Breit interaction, finite nuclear size and nuclear mass effects (reduced mass and mass polarization) as well as approximate QED contributions are included. The DR resonance strengths are constructed from radiative transition rates and Auger rates. In the MCDF theory, there are two different possible methods of calculation: in the average level (AL) scheme, calculations yield the resonance energies and wave functions with the same average quality for all the many-electrons states. In the optimal level (OL) scheme, a certain state, which should be optimized, is selected; the rest of configurations will be used only to improve the chosen one, by accounting for correlation effects. Generally, the OL is more accurate, but requires more computer storage and processing time since it performs separate calculations for all the states of interest, and, usually, convergence is more difficult to reach.

Figure 3.6 shows the differences between the experimental resonance energies and

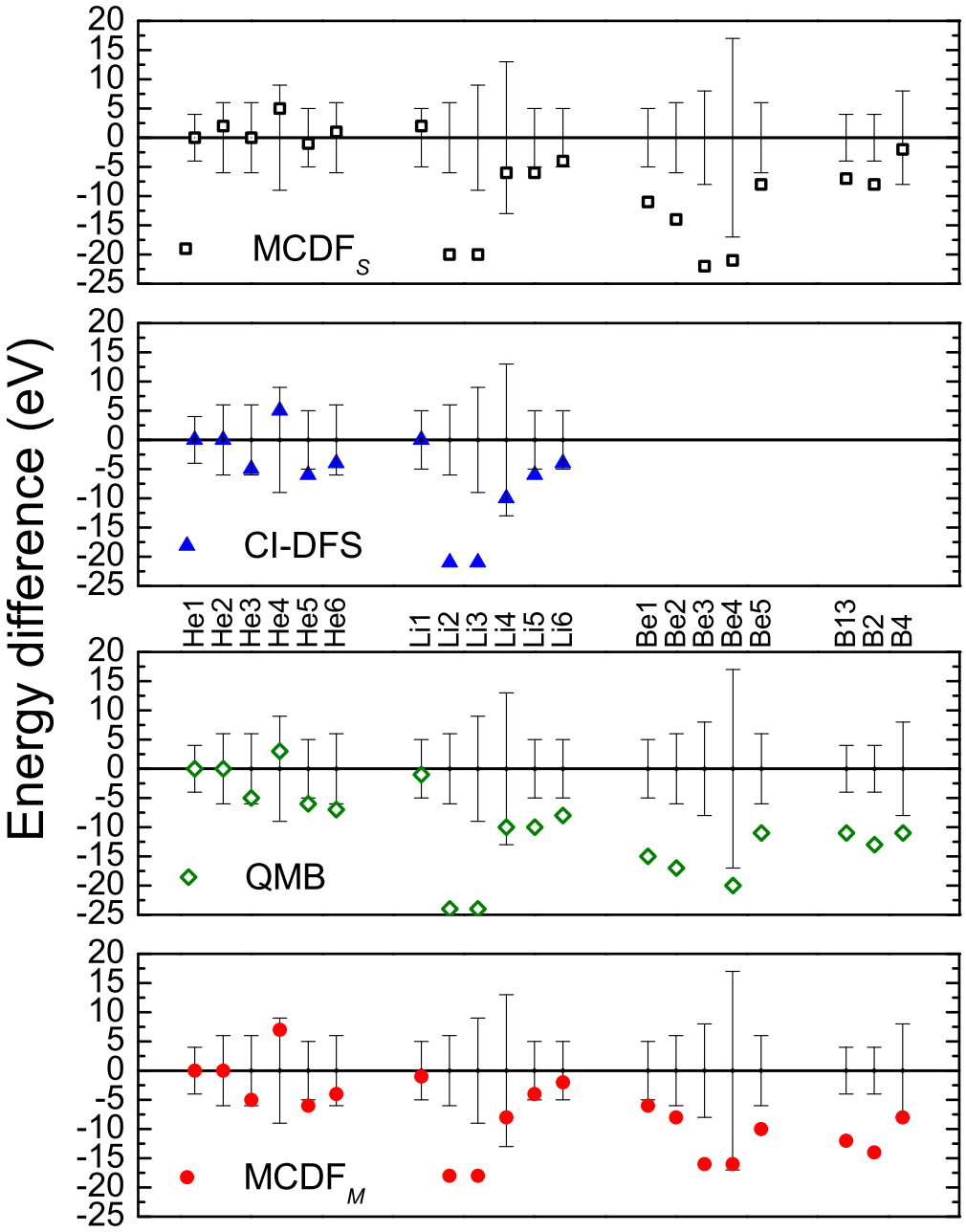

Figure 3.6: Differences (in eV) between experiment and theory (black open squares for MCDF$_S$, blue triangles for CI-DFS, green rhombus for QMB and red circles for MCDF$_M$) for all the measured resonance energies from He- to B-like mercury ions. In this plot the experimental energies use the theoretical value for the DR $(1s2s^2)_{1/2}$ state of He-like ions of each calculation as reference. The error bars shown in the plot are those of the experimental relative resonance energy determination (see Tables 3.2 to 3.5).

the calculations for the charge states ranging from He-like Hg^{78+} to B-like Hg^{75+} ions. The error bars given in this figure are those of the experimental data (see Tables 3.2 to 3.5).

An overall evaluation of the theory can be made by extracting separately for each charge state the average shift and standard deviation of the different models, as shown in Table 3.7. To account for the small differences of the $1s2s^2$ excitation energy among the various calculations, here, the energy scale uses as reference the $1s2s^2$ resonance energy value predicted by each particular model. The various normalization energy changes of -3 eV (CI-DFS), -1 eV (QMB) and -3 eV ($MCDF_M$), respectively, are consistent with the relative error bar of $\pm$ 4 eV.

Table 3.7: Theoretical shift to the experimental data $\overline{\Delta}$ and its standard deviation σ per each ion charge state and model in eV. ϵ represents the averaged experimental error bar for a given charge state. The bold numbers indicate the lowest theoretical discrepancies.

Charge state	**Figure**	**$MCDF_S$**	**CI-DFS**	**QMB**	**$MCDF_M$**
He $\epsilon = 6$	$\overline{\Delta}$	**1.2**	1.3	-1.5	1.7
He	σ	**2.1**	4.1	4	4.8
Li $\epsilon = 7.2$	$\overline{\Delta}$	-9	-7.3	-11.8	**-5.5**
Li	σ	9	8.9	9.3	**7.7**
Be $\epsilon = 8.4$	$\overline{\Delta}$	-15.2		-14.8	**-8.2**
Be	σ	6.1		3.4	**4.6**
B $\epsilon = 5.3$	$\overline{\Delta}$	**-6**		-10.7	-8.3
B	σ	**3.2**		1.2	3.1

The results of the calculations have similar tendencies, in that the discrepancies move into the same direction for a given charge state for all the theoretical models. We observe a very good agreement between all theoretical predictions and the experimental results for the He-like resonances, even when they are up to 5 keV away from the reference energy. The Li-like resonances are, in general, in less good agreement with theoretical predictions. Two of these resonances, Li_2 and Li_3 with the same electronic configuration $((1s2s)_1 2p_{1/2})_{3/2} 2p_{3/2}$ but different total angular momentum $J = 2$ and $J = 1$, respectively, show significantly larger systematic discrepancies than the others ($\approx$ 20 eV). For the $MCDF_M$ calculations where more levels have been taken into account, these differences are somewhat reduced to 17 eV. In addition, the Li_5 which has the same electronic configuration than Li_2 and Li_3 but $J = 3$, it agrees with $MCDF_M$ within 1 eV. The observed Be-like as well as B-like resonances disagree, in general, with all the theoretical predictions. In the case of the Be-like ions, these discrepancies may be due to the problematic theoretical

treatment of the screening of the Lamb shift, and to the admixture of the $(2p_j)^2$ configurations to the ground state $(2s^2)\ ^1S_0$, pointed out by Lindroth [Lin95].

Using the differences in resonance energies, the fine structure splitting can also be accurately extracted. This is expected to result in smaller experimental uncertainty, since the systematic errors originated from the absolute electron beam energy determination are canceled out.

The results are shown in Table 3.8, in comparison with different calculations; four of them have already been described, the fifth was carried out by Safronova in a Non-Relativistic Many Body Perturbation Theory (NRMBPT) but only for the He-like ions. Figure 3.7 displays the deviations graphically. The experimental errors can be as small as 3 eV. The experimental results are found to be in excellent agreement with all theoretical predictions except from the Li_6-Li_2 where the theoretical

Table 3.8: Fine structure splitting for different observed ion charge states.

States	**Experiment** (keV)	**MCDF**$_S$ (keV)	**MCDF**$_M$ (keV)	**QED** (keV)	**CI-DFS** (keV)	**NR-MBPT** (keV)
He_6-He_1	**4.706 (6)**	4.707	4.702	4.699	4.702	4.698
He_6-He_3	**2.220 (6)**	2.221	2.221	2.218	2.221	2.219
He_3-He_1	**2.486 (6)**	2.486	2.481	2.481	2.481	2.479
Li_6-Li_1	**4.468 (4)**	4.462	4.467	4.461	4.463	
Li_2-Li_3	**0.050(9)**	0.050	0.050	0.050	0.050	
Li_6-Li_2	**2.068 (6)**	2.084	2.084	2.084	2.085	
Li_6-Li_4	**1.936 (12)**	1.938	1.942	1.938	1.942	
Li_6-Li_5	**2.184 (4)**	2.186	2.186	2.186	2.186	
Li_5-Li_1	**2.284 (4)**	2.276	2.281	2.275	2.277	
Li_5-Li_4	**0.248(12)**	0.248	0.244	0.248	0.244	
Li_4-Li_1	**2.532(12)**	2.524	2.525	2.523	2.521	
Be_5-Be_1	**4.298 (5)**	4.301	4.294	4.302		
Be_5-Be_3	**2.084 (6)**	2.090	2.082	2.090		
Be_5-Be_4	**2.168 (17)**	2.181	2.174	2.177		
Be_3-Be_4	**0.084 (17)**	0.091	0.092	0.087		
Be_3-Be_1	**2.214 (5)**	2.211	2.212	2.212		
Be_4-Be_1	**2.130 (16)**	2.120	2.120	2.125		
B_4-B_{13}	**2.047 (7)**	2.052	2.051	2.047		
B_4-B_2	**2.104 (7)**	2.102	2.110	2.106		
B_{13}-B_2	**0.057 (3)**	0.058	0.059	0.059		

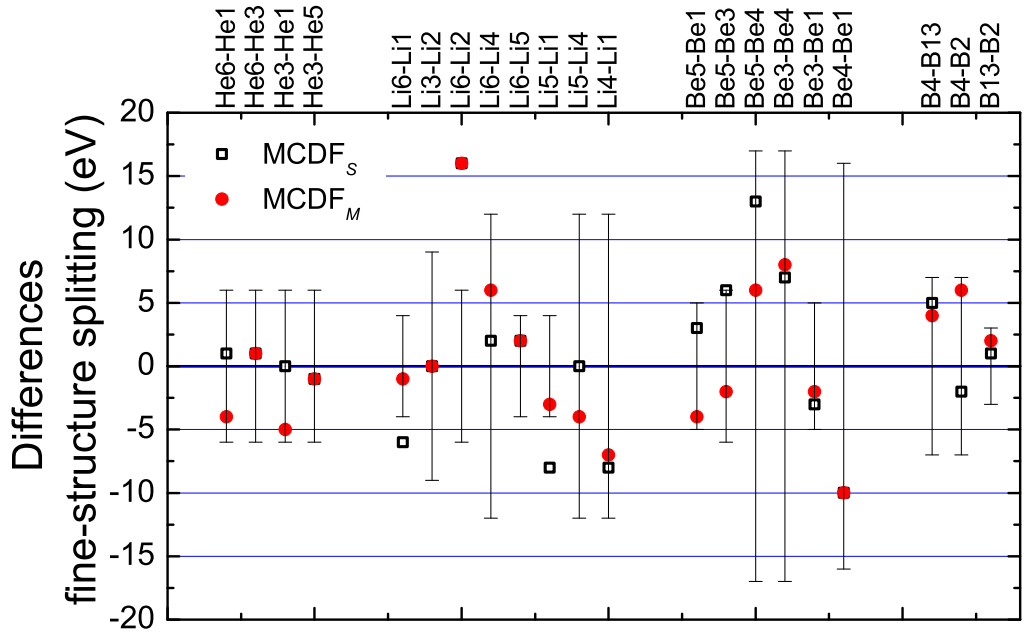

Figure 3.7: Differences (in eV) between the experimental results and the MCDF calculations for the fine structure splitting.

value is about 15 eV higher. In fact, differences which include either the Li_2 or Li_3 resonances, disagree with theory consistently with the discrepancy in the energy determination for the excitation energy of those states discussed above. However, their own difference Li_2-Li_3 agrees well with all the predictions.

Summarizing, QMB seems to neglect some electronic interaction contribution (in first order perturbation), leading in the case of the resonance energies to the poorest general agreement across the whole range of configurations. Some preliminary calculations using the optimized level MCDF$_M$ method, deviate in the case of the Be-like ions from the results by only half as much as other theories. In view of this improved agreement, it is planned to extend its application to the He-, Li- and B-like configurations.

The small discrepancies between theory and experiment for the resonance energy differences can lead to the conclusion that the largest theoretical uncertainty comes from the calculation of the binding energy of the K-shell vacancy, where noticeable disagreements were seen.

3.1.3 Asymmetry of resonance line shapes

By using the narrow cuts, as explained in section 3.1.1, and fitting the lines, the Fano parameter Q is obtained for individual states for the first time in highly charged ions [GCB 05].

The procedure used for the fits is the following: the initial Q factor of a given resonance was set to a very large value (completely symmetric, see Fig. 1.11 in section 1.2.3). Then, the fit was ran iteratively in order to optimize the χ^2/DoF. The asymmetries of the theoretical differential DR cross sections, at 90°, tend to be somewhat weaker when the calculated cross sections are convoluted (see blue and green curves in Figs. 3.8 to 3.10, respectively) with the experimental resolution ($\omega_{exp} \approx 70$ eV).

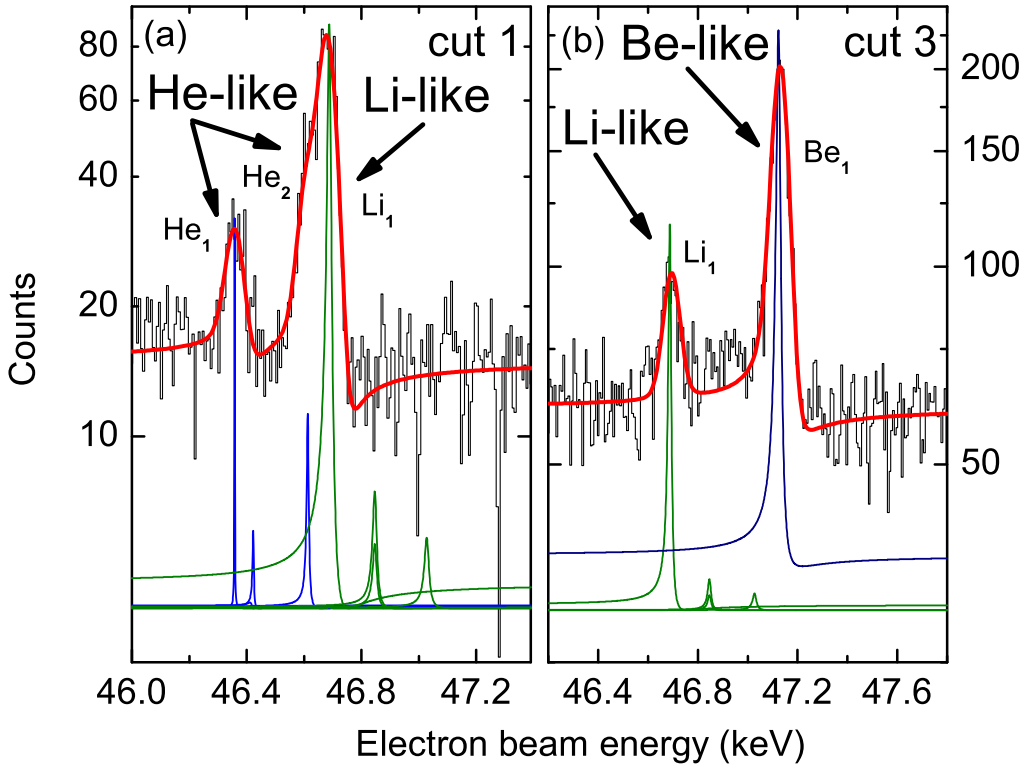

Figure 3.8: Experimental (black curve) and fitted (red curve) DR resonance profiles, for two different slices of the RR $n = 2$, $J = 1/2$ band in the $KL_{12}L_{12}$ region, together with the normalized (non-convoluted) theoretical cross sections (blue and green curves for He- and Li-like ions, respectively). Note that the Fano factors are negative for all states. (a) Projection of the upper slice (cut 1 in Fig. 3.2) with He-like and Li-like resonances. (b) Projection of an intermediate region (cut 3 in Fig. 3.2) with Be- and Li-like resonances.

Figure 3.8a shows the fit to the projection of the uppermost slice (cut 1) in the

RR $n = 2$, $J = 1/2$ band where the degree of asymmetry for the He_1 and Li_1 resonances was extracted. Even though there are six possible $KL_{12}L_{12}$ resonances when starting with He-like ions (see Tables A.1 to A.4 in the Appendix) which all lie within the displayed energy window, only two of them are visible experimentally in the figure (He_1 and He_2) since all the other ones are too small according to the calculations. The predicted position and relative cross section of a third He-like ion DR resonance at 46.423 keV, more than 3 times weaker and separated by about one linewidth from the He_1 resonance, is also displayed. The three further calculated resonances are such small that they are not visible on the linear scale.

According to Table A.2 (see Appendix) four Li-like resonances are predicted to lie in the energy window of Fig. 3.8a on the high energy side of the He-like resonances. Three of them are 20 times weaker than the main line, thus, they cannot be resolved in the experimental data. The strongly asymmetric Li_1 (Li-like) resonance dominates in the $KL_{12}L_{12}$ region (Fig 3.8a).

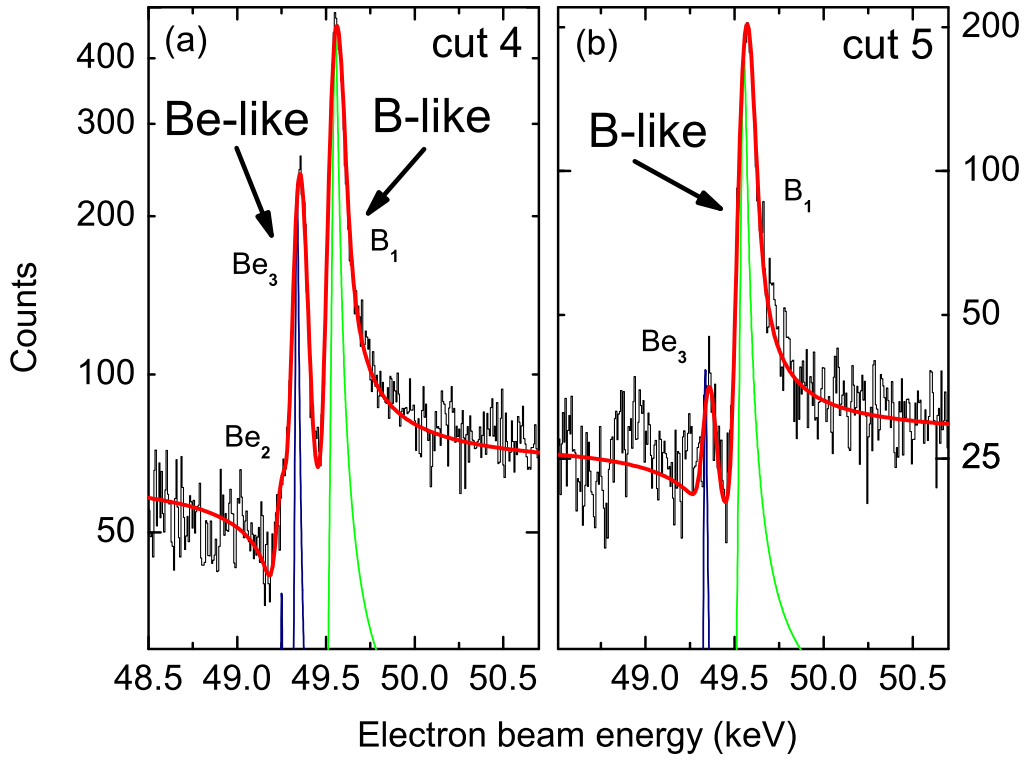

Figure 3.9: In comparison with the He- and Li-like resonances in the $KL_{12}L_{12}$ region (see Fig. 3.8), the $KL_{12}L_3$ Be- and B-like ones show opposite, *i.e.* positive Fano factors. The two cuts displayed here exemplify the method used to resolve resonances from specific charge states. The normalized (non-convoluted) theoretical cross section (blue and green curves) are also shown.

In addition to the above discussed Li-like resonances, which appear only very weakly in cut 3 (Fig. 3.8b), now a single strong Be-like resonance (Be_1) occurs at 47.135(5) keV in the experimental spectrum. Since the Li-like resonances at 46.847 and 47.028 keV are much weaker in this slice, they do not disturb the characterization of the resonance profile of the Be-like line.

Figure 3.9a shows the only two Be-like resonances (Be_2 and Be_3), out of a total of four in the $KL_{12}L_3$ region with a photon energy near the RR $n = 2$, $J = 1/2$ band, which have sizable intensities and were included in the fit. Since the theoretical strength and Fano parameter of the weaker Be_2 were kept fixed in the fit, only information on Be_3 could be extracted. At these x-ray energies ($\approx$ 71.6 keV), two B-like resonances are predicted in the $KL_{12}L_3$ region. The resonance labeled B_1 is about 600 times stronger than a second B-like resonance at 49.491 keV. In the next projection (cut 5), shown in Fig. 3.9b, B_1 is almost completely isolated from the neighboring Be_3 resonance, which now is in addition, very weak in intensity, such that the separated B_1 line shape and Fano factor can be determined with high precision. Nevertheless, the Be_3 resonance was included in the fit.

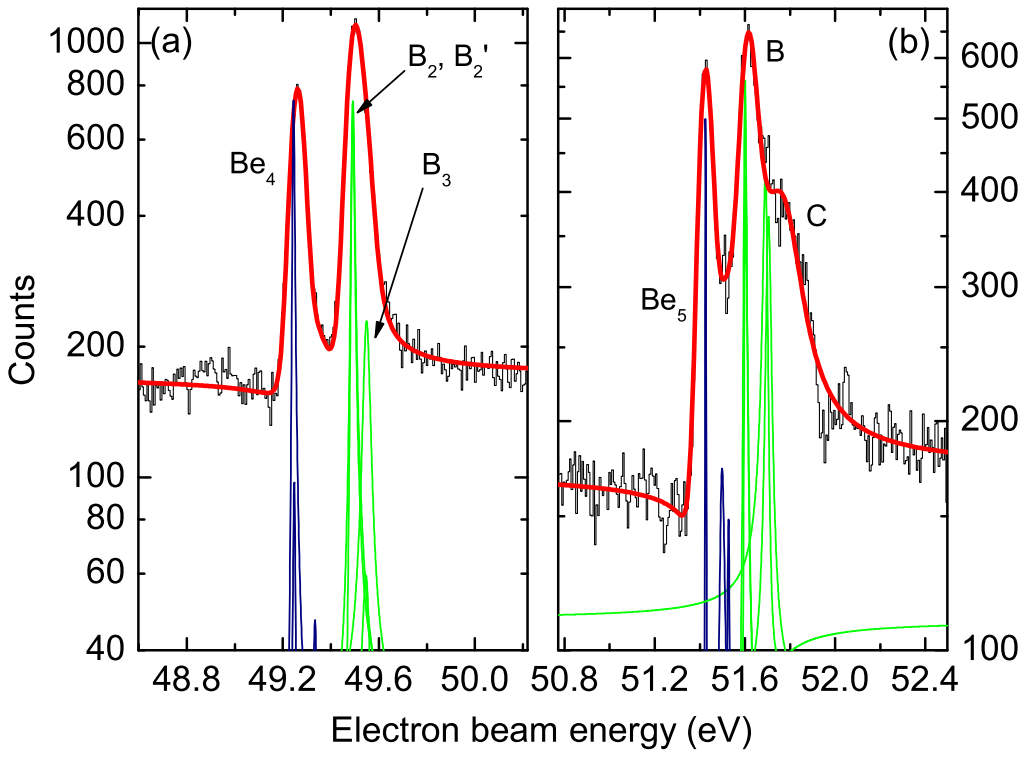

Figure 3.10: Projections onto the electron beam energy axis of two slices of the RR $n = 2$, $J = 3/2$ band, in the $KL_{12}L_3$ (a) and KL_3L_3 (b) regions, respectively.

In Fig. 3.10 some resonances with unresolved blends are shown. The Be_4 resonance in Fig. 3.10a overlaps with another Be resonance, which is 10 times weaker and was therefore neglected. A Be-like resonance at a slightly higher energy (49.335 keV) was taken into account in the fit. From these curves the Fano parameters of B_2 and B_3 were extracted with relatively larger error bars. B_2 partly overlaps with another resonance (B_2') at the same energy, but with half its strength, which is separated from B_3 by one linewidth. This partial blend is reflected in the 10% error bar of the measured Fano parameter. On the other hand, the free (position) fit of B_3 resulted in a symmetric resonance, as expected.

The worst case, shown in Fig. 3.10b, is the Be_5 resonance, which is nonetheless separated from the closest resonances by more than one experimental width. Moreover, these neighboring resonances are about 10 times weaker than the one for Be_5. The group of resonances (B and C) on the right side was not analyzed, because C-like resonances are also expected in this energy region. As a consequence, the error bar of Be_5 is correspondingly large.

We have analyzed the asymmetry factor of the DR resonances individually in the cases where they are reasonable well separated from other features. Table 3.9 summarizes the results of these experiments. As can be clearly seen in Table 3.9, the measured asymmetry Fano factors are in good agreement with theoretical results for all the charge states and different configurations. Only for two of them, Be_1 and Be_5, significant deviations between experiments and theory are observed, beyond

Table 3.9: Theoretical (q_{theo}; $MCDF_S$) and measured Fano factors (q_{meas}) for the strongest DR resonances. Resonances labeled "sym" were fitted with a symmetric profile or they resulted in a very large Fano factor. Γ_d are $MCDF_S$ predictions for the natural width of the resonances.

Label	$\|d\rangle$	**J**	Γ_d (eV)	Q_{theo}	Q_{meas}
He_1	$1s2s^2$	1/2	1	-140	**sym.**
Li_1	$1s2s^22p_{1/2}$	1	11	-12.2	**-14.2(2.2)**
Be_1	$1s2s^2(2p_{1/2})^2$	1/2	16	-12	**-9.3(0.9)**
Be_3	$(1s2s^22p_{1/2})_0 2p_{3/2}$	3/2	19	7.3	**6.7(0.6)**
Be_4	$(1s2s^22p_{1/2})_1 2p_{3/2}$	5/2	11	13	**18.2(6.6)**
Be_5	$1s2s^2(2p_{3/2})^2_2$	5/2	5	16.3	**11.1(2.0)**
B_1	$1s2s^2(2p_{1/2})^2\ 2p_{3/2}$	1	35	5.2	**5.1(0.3)**
B_2	$1s2s^2(2p_{1/2})^2\ 2p_{3/2}$	2	16	9	**10(1)**
B_3	$1s2s^2(2p_{1/2})^2\ 2p_{3/2}$	1	35	-441	**sym.**
B_4	$(1s2s^22p_{1/2})_1\ (2p_{3/2})^2_2$	3	16	-630	**sym.**

the experimental error bar.

In order to verify the accuracy of the experimentally determined Fano factors and demonstrate that the line asymmetry is not an experimental artifact, we analyzed the profiles of strong transitions not affected by interference using the same analyzing procedure. A cut in Fig. 3.2 was selected in parallel to the $J = 3/2$ band but shifted to lower x-ray energies, passing through a set of lines excited by DR resonances which do not overlap with the RR band, since the photon is emitted through a transition from a $J = 1/2$ level, whereas the foregoing recombination took place into a $J = 3/2$ vacancy. That means that these transitions are followed by a $n = 2$, $J = 3/2$ to $n = 2$, $J = 1/2$ transition for the final relaxation. In this projection, three strong peaks from C-, N- and O-like Hg ions are clearly visible. Here, no quantum interference is expected to occur, and the observed line profiles are indeed symmetrical as shown in Fig 3.11. This confirms that the observed asymmetry is not an artifact produced by our data acquisition system, other experimental peculiarities or by the data analysis, but appears only in the resonance profiles of those states where it was predicted. Indeed, this was already implied in the changing signs of the measured Fano factors, which also exclude an asymmetry caused by our apparatus or experimental procedure.

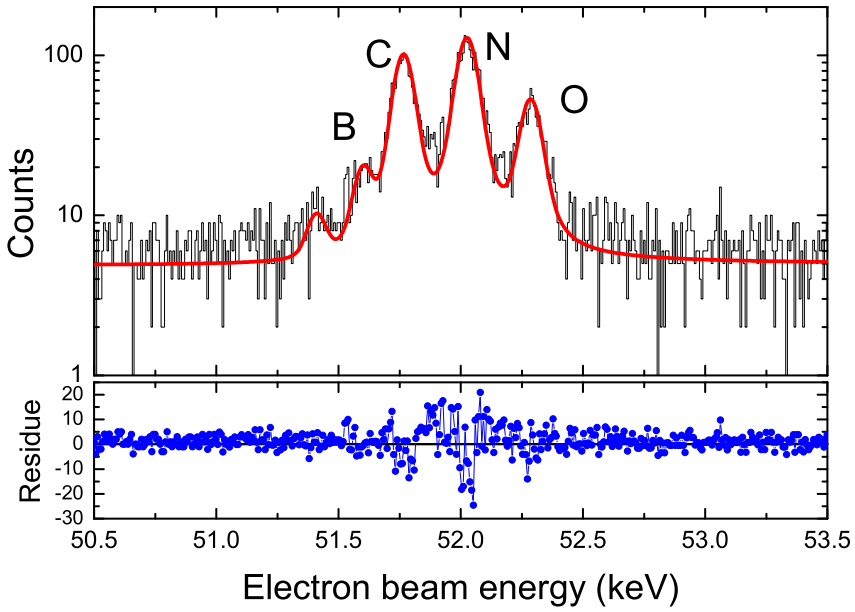

Figure 3.11: Projection of a slice taken below and parallel to the RR $n = 2$, $J = 3/2$ band. This cut shows clearly the symmetry of all the resonances ranging from B- to O-like Hg ions. The lower plot displays the residue of the fit.

3.1.4 Deexcitation X-ray transitions

During the experiment, the energy scale of the Ge-detector collecting the photons following recombination was calibrated about every four hours. The calibration lines used in this experiment were produced by irradiating thin foils of tungsten, tantalum and lead with 122 keV γ-rays of a ^{57}Co source from behind, exciting K_α and K_β lines from those targets. Two K_α lines, namely, the K_{α_1} transition from the $2p_{3/2}$ to the $1s$ states (also labeled as KL3) and the K_{α_2} corresponding to the $2p_{1/2}$ to $1s$ transition (KL2) can be seen for each element. The two K_β lines are detected for Ta and W targets, but those of Pb were very weak. The observed K_{β_3} peak from W is, in fact, a mixture of two transition lines, namely, KM2 and KM3. Their intensity ratio is known to be $I(KM2)/I(KM3) = 0.521$ [SPK73]. The next peak at higher energies (W $K_{\beta 1}$) contains a larger number of blended transitions, and could not be used. In Table 3.10 their energies are given [NIS04]. More details on the energy of these lines, their uncertainties and ratios can be found in Ref. [IBL98].

Table 3.10: Kα and Kβ transition energies of Ta, W and Pb which were used in the energy calibration of the germanium detector [NIS04, IBL98].

Transition	**Ta** (eV)	**W** (eV)	**Pb** (eV)
KL2 (K_{α_2})	56278.7(18)	57981.9(19)	72806.6(25)
KL3 (K_{α_1})	57533.9(17)	59318.8(17)	74970.2(24)
KM2 (K_{β_3})	64947.7(28)	66952.1(29)	
KM3 (K_{β_1})	65222.1(29)	67245.6(30)	

Figure 3.12 shows a calibration spectrum. Here, the right scale indicates the energies of the calibration lines, which fit in the energy-channel conversion shows a regression coefficient of $R = 1$ and an accuracy at 70 keV of about 20 eV for each individual calibration. Calibrations were carried out between the measurements (see below) allowing one to correct for any systematic drift. In contrast to the krypton test experiment, where both calibration and measured lines showed low energy tails, in the present experiment the line profiles are not visibly affected by such tails and, therefore, Gaussian distributions could be used for the fitting procedure without loss of accuracy.

Like in the demonstration of interference patterns, we have performed selective projections onto the x-ray energy axis of the 2D map for well defined windows in the electron energy (see Fig. 3.13). At an electron beam resonance energy, such

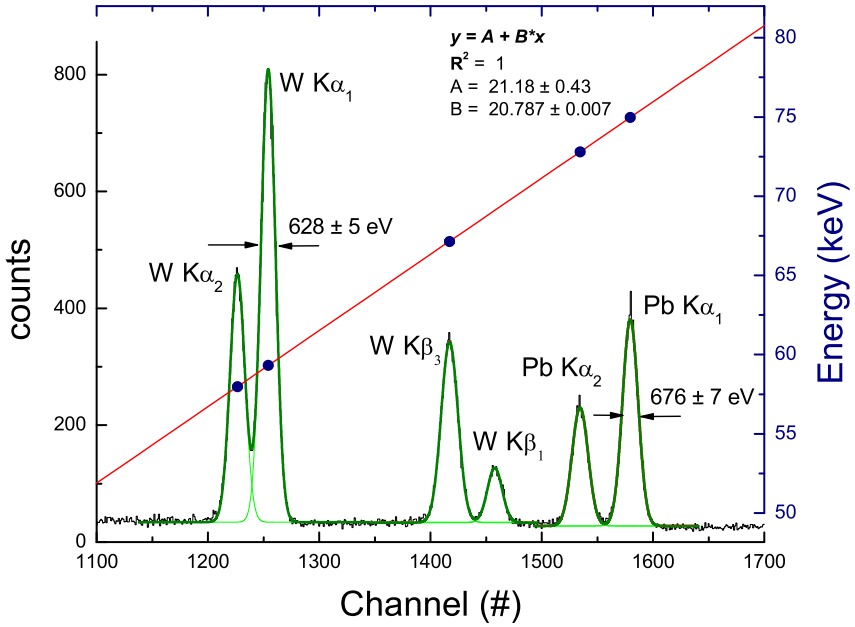

Figure 3.12: Kα (W and Pb) and Kβ (W) lines excited with the 122 keV emission line of ^{57}Co.

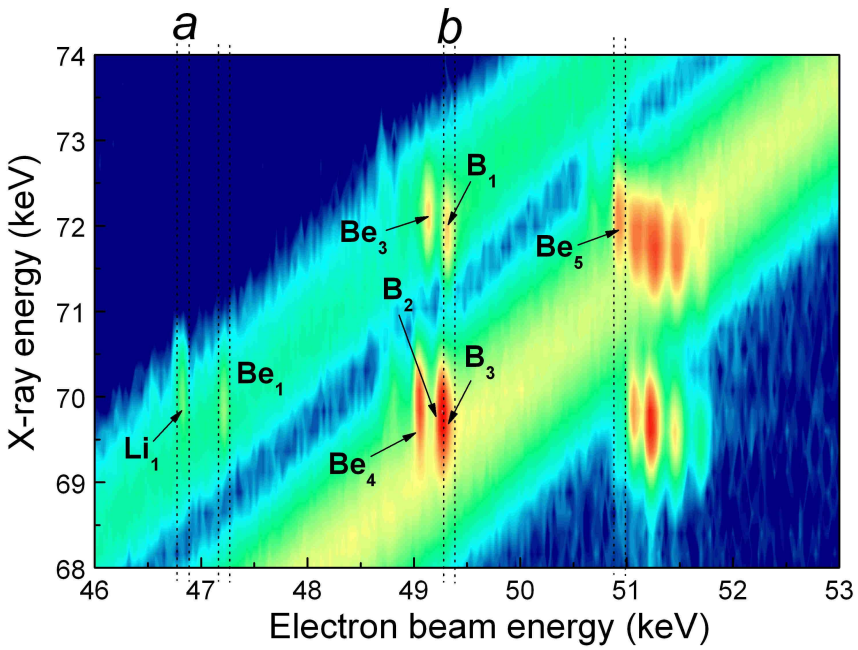

Figure 3.13: Logarithmic 2D contour-map of the photorecombination of highly charged mercury ions in the DR KLL region. The dotted lines represent a few of the thin cuts projected onto the x-ray energy axis (see Fig. 3.14 for the projections of the cuts labeled here as a and b).

projections contain x-ray photons from the resonances as well as from RR $n = 2$ (the two peaks; $J = 1/2$ and $J = 3/2$, respectively). The experimental data were grouped into two data sets (about two hours each), one taken before and another after a Ge-detector calibration took place. Sets of data acquired over 4 hours do not allow to distinguish the small He-like resonances clearly. Thus, the highest charge state analyzed here corresponds to Li-like ions.

As an example, Fig. 3.14 shows two different projections corresponding to the resonances of Li-like ions in the $KL_{12}L_{12}$ region (Li_1 in Fig. 3.14a) and the resonances of B-like ions labeled B_1 and B_3 in the $KL_{12}L_3$ region (Fig. 3.14b). The good quality of these fits is inferred from the χ^2/DoF value, which was 0.72 and 0.88 for the spectra containing the Li_1 and B_1 resonances, respectively.

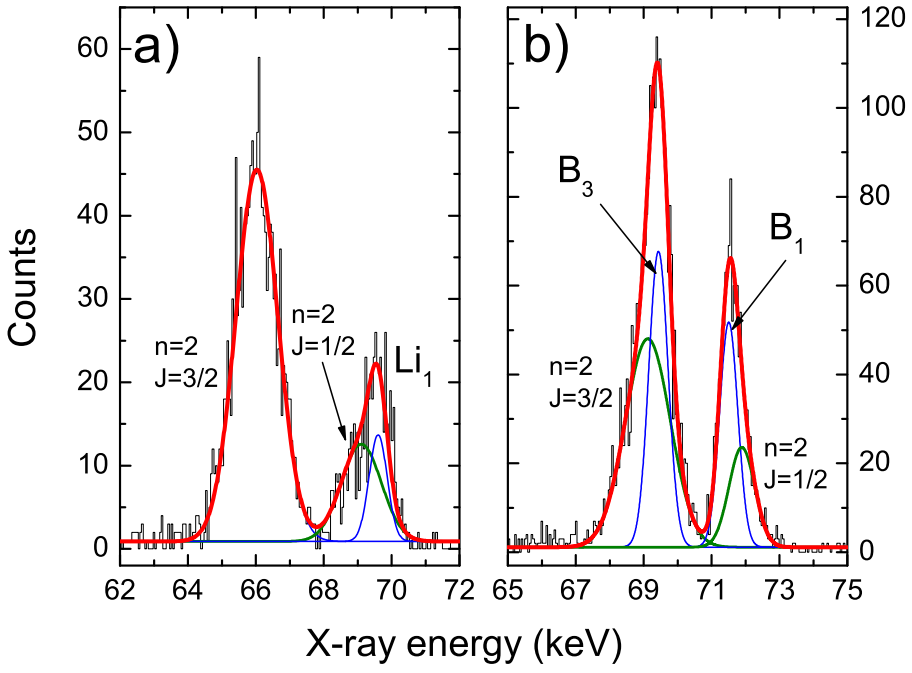

Figure 3.14: Two projections onto the x-ray axis of a single data set. The two peaks, which are always present in these type of projections correspond either to the RR $n = 2$, $J = 1/2$ and $J = 3/2$ bands, respectively outside of the resonance energy or to a superposition of RR and DR contributions for cuts including a resonance. a) Projection of the Li_1 resonance in the $KL_{12}L_{12}$ region for excitation energies E_e in the range $E_e = (46686 \pm 46)$ eV. b) Projection of the B_1 and B_3 resonances in the $KL_{12}L_3$ region $E_e = (49557 \pm 61)$ eV.

The results obtained for the x-ray spectra at resonance energies in the different sets of data with their separatedly calibrated runs were averaged according to their respective statistical weights. Table 3.11 shows the measured photon energies in comparison with $MCDF_S$ and $MCDF_M$ calculations. Some of the predictions marked

with a double subindex in the table have been obtained by averaging a few (two to four) single state values taking into account their theoretical strengths (see Tables A.1 to A.4 in the Appendix).

Table 3.11: Measured x-ray energies, compared with theoretical $MCDF_S$ and $MCDF_M$ calculations for Hg ions in different charge states [Sco03]. The primes accompanying some of the resonance labels indicate the existence of a second resonance, the x-ray energy of which, is near by the one under study. Some of the resonances are labeled with two subindeces if two or more single states contribute (see text). $|d\rangle_J$ and $|f\rangle_J$ indicate the intermediate and final state with their corresponding total angular momentum J.

Label	$\|d\rangle_J$	$\|f\rangle_J$	**Experiment**	**MCDF$_S$**	**MCDF$_M$**
Li_1	$[1s2s^22p_{1/2}]_1$	$[1s^22s^2]_0$	**69.841(65)**	69.866	69.869
Li_2	$[((1s2s)_1 2p_{1/2})_{3/2} 2p_{3/2}]_2$	$[1s^22s2p_{1/2}]_1$		72.006	72.015
Li_3	$[((1s2s)_1 2p_{1/2})_{3/2} 2p_{3/2}]_1$	$[1s^22s2p_{1/2}]_1$		72.057	72.065
Li_3'	$[((1s2s)_1 2p_{1/2})_{3/2} 2p_{3/2}]_1$	$[1s^22s2p_{1/2}]_0$		72.093	72.102
Li_{23}			**72.081(78)**	72.033	72.042
Li_5	$[((1s2s)_1 2p_{1/2})_{3/2} 2p_{3/2}]_3$	$[1s^22s2p_{3/2}]_2$	**69.805(60)**	69.826	69.833
Li_6	$[(1s2s)_1 (2p_{3/2})^2_2]_3$	$[1s^22s2p_{3/2}]_2$	**72.039(60)**	72.012	72.019
Be_1	$[1s2s^2(2p_{1/2})^2]_{1/2}$	$[1s^22s^22p_{1/2}]_{1/2}$	**69.657(32)**	69.703	
Be_2	$[(1s2s^22p_{1/2})_1 2p_{3/2}]_{3/2}$	$[1s^22s^22p_{1/2}]_{1/2}$		71.827	
Be_3	$[(1s2s^22p_{1/2})_0 2p_{3/2}]_{3/2}]$	$[1s^22s^22p_{1/2}]_{1/2}$		71.914	
Be_{23}			**71.879(14)**	71.907	
Be_4	$[(1s2s^22p_{1/2})_1 2p_{3/2}]_{5/2}$	$[1s^22s^22p_{3/2}]_{3/2}$		69.722	
Be_4'	$[(1s2s^22p_{1/2})_1 2p_{3/2}]_{3/2}$	$[1s^22s^22p_{3/2}]_{3/2}$		69.726	
Be_4			**69.702(15)**	69.722	
Be_5	$[1s2s^2(2p_{3/2})_2{}^2]_{5/2}$	$[1s^22s^22p_{3/2}]_{3/2}$	**71.880(16)**	71.904	
B_1	$[1s2s^2(2p_{1/2})^2 2p_{3/2}]_1$	$[1s^22s^2(2p_{1/2})^2]_0$	**71.674(17)**	71.666	71.671
B_5	$[(1s2s^22p_{1/2})_1 (2p_{3/2})^2_2]_3$	$[1s^22s^22p_{1/2}2p_{3/2}]_2$	**71.682(20)**	71.669	71.669
B_2	$[1s2s^2(2p_{1/2})^2 2p_{3/2}]_2$	$[1s^22s^22p_{1/2}2p_{3/2}]_2$		69.560	69.562
B_2'	$[1s2s^2(2p_{1/2})^2 2p_{3/2}]_2$	$[1s^22s^22p_{1/2}2p_{3/2}]_1$		69.578	69.580
B_3	$[1s2s^2(2p_{1/2})^2 2p_{3/2}]_1$	$[1s^22s^22p_{1/2}2p_{3/2}]_2$		69.618	69.620
B_3'	$[1s2s^2(2p_{1/2})^2 2p_{3/2}]_1$	$[1s^22s^22p_{1/2}2p_{3/2}]_1$		69.636	69.638
B_{23}			**69.551(17)**	69.585	69.586
B_4	$[(1s2s^22p_{1/2})_1 (2p_{3/2})^2_2]_3$	$[1s^22s^2(2p_{3/2})^2]_2$	**69.546(15)**	69.603	69.603

In Fig. 3.15 the differences between experimental results and the predictions ($MCDF_S$ and $MCDF_M$) for the measured transitions are plotted. The relatively large error bars ($\approx$ 60 eV at 72 keV) found in the Li-like ion resonances are due to the low number of counts. Within these uncertainties, a fair agreement with the theoretical predictions is observed. The measured Be-like ion resonance energies, instead, are significant smaller than theoretical predictions ($\approx$ 30 eV), well outside

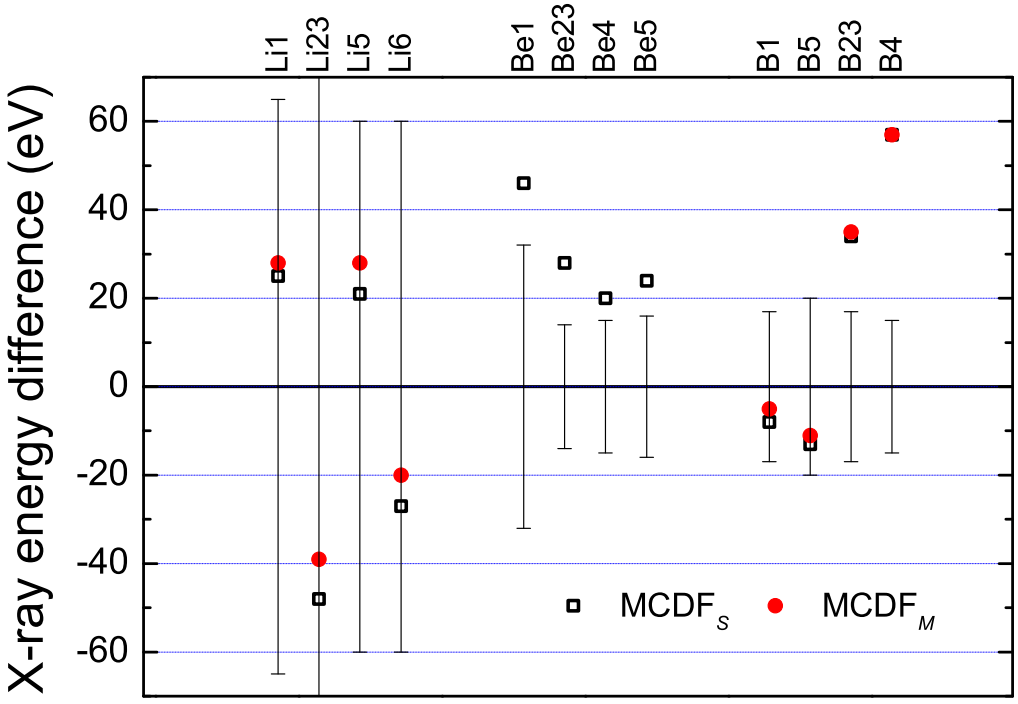

Figure 3.15: Differences between the observed x-ray energies and the MCDF$_S$ (black squares) and the MCDF$_M$ (red circles) calculations. The error bars shown are those of the measured x-ray energies (see Table 3.11).

the experimental error bars of only ± 14 eV. The somewhat larger error bar for the Be$_1$ resonance is partly due to its low number of counts, and, in addition, to its complete overlap with the RR $n = 2$, $J = 1/2$ band. Here, the B-like ion resonances found at the x-ray energy region around 71.7 keV, are found to be in a good agreement with the predictions, while the other two resonances at about 69.6 keV are consistently shifted towards lower energies compared to the calculations.

Fine structure in the x-ray energy spectra

The differences between the x-ray transition energies measured here provide again information on the fine structure splitting of the $n = 2$ levels with different J for ions in a particular charge state. Here we distinguish between the emission of photons from the $2p_{3/2}$, $2p_{1/2}$ and $2s_{1/2}$ states into lower states. Data in Fig. 3.16 are divided into two zones: the upper part corresponding to the differences between states $J = 1/2$ and $J = 3/2$, and the lower one to the differences of those states with the same J, which are, in first approximation, expected to be close to zero. The energy separation between the $J = 1/2$ and $J = 3/2$ bands is, on average, 2.15 keV

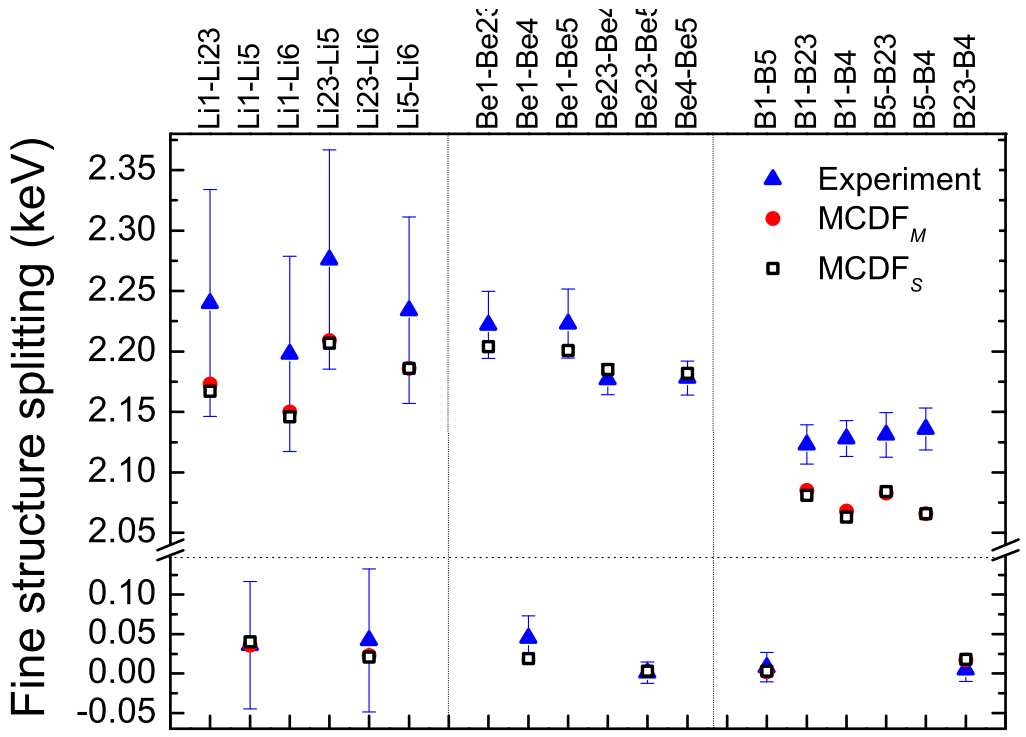

Figure 3.16: Fine structure splitting between states with $J = 3/2$ and $J = 1/2$ (upper part) and difference between states with the same J (lower part) for mercury ions with different charge states and configurations as indicated on the top of the figure. The experimental and theoretical ($MCDF_S$ and $MCDF_M$ calculations) data points are obtained from Table 3.11.

slightly decreasing with decreasing the ion charge.

The results are for Li- and Be-like ions agree within error bars with the theoretical predictions. Significant deviations between experimental results and theoretical predictions, well outside the experimental error bars are found for all B-like states. Although the experimental results for the lower zone (Fig. 3.16) transitions are in agreement with the expectations, this discrepancy, the reason of which is unclear, has to be taken seriously, nonetheless.

Conclusions

The aim of this work was to use the energy dependence of the photorecombination to study the electronic structure of HCI, and to investigate the related quantum interference effects. The experimental methods implemented at the Heidelberg EBIT have made it possible to achieve those ends.

In the present work, we have extensively reported on accurate measurements of DR resonance energies of highly charged $Hg^{75+...78+}$ ions. Their excitation energies, which are in the range of 50 keV, have been determined with a relative experimental uncertainty as small as ± 5 eV [GAC 05]. This has allowed us to benchmark the quality of the most advanced state-of-the-art calculations [HJK05b]. At the present level of accuracy, calculations of QED contributions to the binding energies of $1s$, $2s$ and $2p$ states, and nuclear size effects up to $n = 2$ can currently be compared with experimental values. Predictions and experimental results agree for the DR of He-like Hg^{78+} within ± 2 eV. However, agreement becomes poorer for lower charge states. In fact, discrepancies as high as 15 eV have been observed for the Be-like Hg^{76+} ions, which cannot be explained by the experimental uncertainties. Since the fine structure splitting, which was also measured, compares rather well with theory, these discrepancies are most likely due to an imprecise calculation of the binding energy of the DR initial state.

It is planned to extend both the experimental and the theoretical analysis to the lowest mercury charge states (also present in the experiment as shown, for instance, in Fig. 3.11), namely, C-, N- and O-like. For ions with almost filled L-shells, the number of possible resonances and transitions in the KLL region becomes again small, and therefore more appealing to theory. For instance, only two resonances, completely separated in the x-ray energy by about 2 keV, are predicted ($MCDF_S$) for the O-like mercury ions at 52.336 keV.

Although the x-ray detector resolution limited the accuracy of the x-ray energy measurements, the final results have nonetheless absolute error bars as small as ± 14 eV at 70 keV. Thus, they can compete with the most precise experiments in

many-electron high-Z ions, as the K_{α_1} transitions in U^{90+} ions at (100626 ± 35) eV [BCI 90] or in Bi^{81+}, (78825 ± 85) eV [SMG 92]. They are even within a factor of three in accuracy of the most recent result reported for the H-like U^{91+} Ly_α transition [GSB 05], whose averaged value has an error bar of ± 4.6 eV.

Perhaps the most original result of this thesis is the unambiguous observation of the quantum interference between dielectronic and radiative recombination processes for several resonances in highly charged mercury ions [GCB 05]. Our improved experimental resolution has made it possible to accurately characterize, for the first time, the degree of asymmetry in state-selected DR resonances, and indicates a deviation from theory in the case of two Be-like resonances. A full understanding of the implications of these discrepancies has not yet been achieved.

In summary, as for the resonance positions and the Fano factors, we find significantly large systematic differences between the experimental observations and all available theoretical predictions for the Be- as well as for two of the B-like states. Since the resonance energies, determined from the electron beam energy, the x-ray energies from the Ge detector, and the shape of the Fano profile represent three quite independent measurements that cannot be affected by the same systematic experimental error, these deviations, even though they are sometimes close to the size of the error bars, have to be taken seriously. Screening of the Lamb shift in Be-like ions, and configuration admixture could, in part, explain these findings [Lin95]. A set of improved calculations by Harman [HJK05a] seems to indicate that the agreement can be improved by increasing the number of states in the calculations, and a further expansion of the basis set of states is underway [HJK05b].

In order to become completely independent of any theoretical input, the presented measurements should be carried out in future by varying, in addition to the electron beam energy, the electron beam current. As we showed in the case of Kr^{34+} ions, the extrapolation to zero current can provide absolute resonance excitation energies with error bars on the order of 1 eV. It is planned to perform such experiments with highly charged uranium ions. The low uncertainties of the present results will be further improved by means of the thermally stabilized high-precision voltage divider developed here. In addition, the uncertainties of the measured x-ray energies will be reduced in forthcoming experiments by means of higher resolution detectors.

More generally, the difficulties appearing in the determination of x-ray energies in the 100 keV range could be avoided in part by developing electron beams with better defined properties in combination with photon detection. That goal could, in principle, also be pursued by introducing spectroscopic instrumentation to the new electron target at the TSR, with its excellent electron beam characterization, although problematic corrections of the Doppler shift may still be needed there. On

the other side, a large increase in resolution through a consequent application of the EBIT techniques utilized in the present work can already be foreseen for the immediate future. In this way, spectroscopy of trapped HCI will continue to deliver reliable data and remain an extremely valuable alternative tool for the study of QED effects in high-Z ions.

Appendix A

A.1 Mercury tables: theoretical parameters

In the following, four tables (He- to B-like) containing several theoretical parameters from the MCDF$_S$ calculations are given [Sco03]. These tables contain the config-

Table A.1: MCDF$_S$ calculation for the observed and nearby resonances of He-like mercury ions. The resonance and x-ray energies are given in keV. The strength is expressed in units of $b \cdot eV/sr$ (b = barn = 10^{-24} cm^2) and Γ_d is the natural width in eV.

$\|d\rangle$	**J**	**Label**	**Excitation**	$\mathbf{E}_\gamma$	**Strength**	Γ_d	Q
$1s2s^2$	1/2	He_1	46.358	67.678	2511.71	1.1	-140
$1s(2p_{1/2})^2$	1/2		46.681	70.000	13.07	15.6	-2.75
$(1s2s)_0 2p_{1/2}$	1/2	He_2	46.613	70.156	3956.1	6.9	-15.3
$(1s2s)_1 2p_{1/2}$	1/2		46.423	69.965	787	4.9	-8.1
$1s2s2p_{1/2}$	3/2		46.417	69.959	53.12	10.7	-1.1
$1s2s^2$	1/2		46.358	67.528	17.9	1.12	-5.1
$(1s2s)_0 2p_{3/2}$	3/2	He_3	48.844	72.386	3118.8	4.5	-11.9
$1s2s2p_{3/2}$	3/2		48.695	72.238	32.5	15.6	-1.37
$(1s2p_{1/2})_0 2p_{3/2}$	3/2	He_4	48.923	72.243	1574	18.8	6.95
$1s2p_{1/2}2p_{3/2}$	3/2		48.838	72.157	154.5	11.9	2.7
$(1s2p_{1/2})_1 2p_{3/2}$	5/2		48.834	70.003	2921.7	11.1	10.6
$(1s2s)_0 2p_{3/2}$	3/2	He_5	48.844				
$1s2p_{1/2}2p_{3/2}$	3/2		48.838	70.007	239	11.9	-9.4
$(1s2p_{1/2})_0 2p_{3/2}$	3/2		48.923	70.093	162.7	18.8	-6.2
$1s(2p_{3/2})^2$	5/2	He_6	51.065	72.234	1418.5	5.2	13.2
$1s(2p_{3/2})^2$	3/2		51.133	72.302	29.3	208.7	6
$1s(2p_{3/2})^2$	1/2		51.169	72.339	14.8	297.3	-6.2

uration of the doubly excited state $|d\rangle$ and total angular momentum J, the **label** for the observed states, **excitation** energy (keV), photon energy $\mathbf{E}_\gamma$ (keV), strength (barn·eV/sr), natural width Γ_d (eV) and the dimensionless Fano parameter Q.

Table A.2: MCDF$_S$ calculation for the observed and nearby resonances of Li-like mercury ions. The resonance and x-ray energies are given in keV. The strength is expressed in units of $b \cdot eV/sr$ (b = barn = 10^{-24} cm^2) and Γ_d is the natural width in eV.

$\|d\rangle$	**Label**	**J**	**Excitation**	$\mathbf{E}_\gamma$	Strength	Γ_d	Q
$1s2s^22p_{1/2}$	1	Li_1	46.688	69.865	2229	11.1	-12.2
$1s2s2p_{1/2}{}^2$	1		46.847	69.787	127.5	15.8	-10.9
$1s2s2p_{1/2}{}^2$	1		46.847	69.824	65.8	15.8	-12
$1s2s2p_{1/2}{}^2$	0		47.028	69.968	70.76	17.7	-12.2
$1s2s2p_{1/2}2p_{3/2}$	0		49.106	72.046	12.1	29.6	-4.4
$((1s2s)_1 2p_{1/2})_{3/2}2p_{3/2}$	2	Li_2	49.066	72.006	819.6	20.7	7.1
$((1s2s)_1 2p_{1/2})_{3/2}2p_{3/2}$	1	Li_3	49.116	72.056	216.4	26.9	5.3
$((1s2s)_1 2p_{1/2})_{3/2}2p_{3/2}$	1	Li_3	49.116	72.093	285.4	26.9	4.9
$((1s2s)_0 2p_{1/2})_{1/2}2p_{3/2}$	2	Li_4	49.212	72.152	573.4	14.5	9.6
$1s2s^22p_{3/2}$ M2-decay	2		48.879	72.056	232.9	0.1	257
$1s2s^22p_{3/2}$	1		48.938	72.115	166.8	19.5	-2.6
$1s2s2p_{1/2}2p_{3/2}$	2		48.951	71.892	15.6	6.5	1.7
$1s(2p_{1/2})^22p_{3/2}$	1		49.372	71.989	4	19.2	-3.2
$1s(2p_{1/2})^22p_{3/2}$	2		49.313	71.930	15.4	0.1	845
$((1s2s)_1 2p_{1/2})_{3/2}2p_{3/2}$	3	Li_5	48.964	69.825	1704.2	10.7	12.5
$((1s2s)_0 2p_{1/2})_{1/2}2p_{3/2}$	2		49.212	70.073	178.45	14.5	79
$((1s2s)_1 2p_{1/2})_{3/2}2p_{3/2}$	1		49.116	69.876	211.6	26.9	-14.3
$((1s2s)_0 2p_{1/2})_{1/2}2p_{3/2}$	2		49.212	69.972	378.8	14.5	7.8
$1s2s2p_{1/2}2p_{3/2}$	2		48.951	69.812	89.9	6.5	-125
$1s2s2p_{1/2}2p_{3/2}$	1		49.216	70.077	9	7.2	3.8
$1s2s2p_{1/2}2p_{3/2}$	1		49.039	69.900	30	26.7	4.24
$(1s2s)_1(2p_{3/2})_2{}^2$	3	Li_6	51.150	72.011	1177.8	5.4	15.7
$1s2s(2p_{3/2})^2$	2		51.264	72.125	220.8	23.5	7.6
$1s2s(2p_{3/2})^2$	1		51.303	72.164	194.8	14.9	-9.3

Table A.3: MCDF$_S$ calculation for the observed and nearby resonances of Be-like mercury ions. The resonance and x-ray energies are given in keV. The strength is expressed in units of $b \cdot eV/sr$ and Γ_d is the natural width in eV.

$\|d\rangle$	**Label**	**J**	**Excitation**	$\mathbf{E}_\gamma$	Strength	Γ_d	Q
$1s2s^2(2p_{1/2})^2$	1/2	Be_1	47.124	69.703	255.8	16.1	-12
$(1s2s^22p_{1/2})_12p_{3/2}$	3/2	Be_2	49.248	71.827	149.6	11.1	2.8
$(1s2s^22p_{1/2})_02p_{3/2}$	3/2	Be_3	49.335	71.914	1676.46	18.9	7.3
$(1s2s^22p_{1/2})_12p_{3/2}$	5/2		49.244	71.822	4.7	10.1	-1.9
$1s2s^22p_{1/2}2p_{3/2}$	1/2		49.284	71.862	57.6	30.1	-4.5
$(1s2s^22p_{1/2})_12p_{3/2}$	5/2	Be_4	49.244	69.721	3000	10.8	12.9
$(1s2s^22p_{1/2})_12p_{3/2}$	3/2		49.248	69.726	249.1	11.1	-11.3
$1s2s^22p_{1/2}2p_{3/2}$	1/2		49.284	69.761	32.2	30.1	2
$(1s2s^22p_{1/2})_02p_{3/2}$	3/2		49.335	69.813	184.1	18.9	-7.5
$1s2s^2(2p_{3/2})_2{}^2$	5/2	Be_5	51.425	71.903	1963.8	5.1	16.3
$1s2s^2(2p_{3/2})_2{}^2$	5/2		51.497	71.975	192.7	28.6	6.7
$1s2s^2(2p_{3/2})_2{}^2$	5/2		51.528	72.006	304	14.5	-9.2

Table A.4: MCDF$_S$ calculation for the observed and nearby resonances of B-like mercury ions. The resonance and x-ray energies are given in keV. The strength is expressed in units of $b \cdot eV/sr$ and Γ_d is the natural width in eV.

$\|d\rangle$	**Label**	**J**	**Excitation**	$\mathbf{E}_\gamma$	Strength	Γ_d	Q
$1s2s^2(2p_{1/2})^22p_{3/2}$	1	B_1	49.549	71.665	656.97	35	5.2
$1s2s^2(2p_{1/2})^22p_{3/2}$	2		49.491	71.607	1.3	15.9	-1.5
$1s2s^2(2p_{1/2})^22p_{3/2}$	2	B_2	49.491	69.578	748	15.9	8.9
$1s2s^2(2p_{1/2})^22p_{3/2}$	1	B_3	49.549	69.617	400.2	35	-441
$1s2s^2(2p_{1/2})^22p_{3/2}$	2		49.491	69.559	481	15.9	18.5
$1s2s^2(2p_{1/2})^22p_{3/2}$	1		49.549	69.636	73.1	35	-5.8
$(1s2s^22p_{1/2})_1(2p_{3/2})^2{}_2$	3		51.601	71.668	328.5	15.7	5
$(1s2s^22p_{1/2})_1(2p_{3/2})^2{}_2$	3	B_4	51.601	69.602	656.33	15.7	-630
$1s2s^22p_{1/2})(2p_{3/2})^2$	1		51.649	69.651	25.42	38.9	-877
$1s2s^22p_{1/2})(2p_{3/2})^2$	1		51.693	69.621	93.6	25	673

Bibliography

[ABC 90] Ali R., Bhalla C. P., Cocke C. L. and Stockli M.: *Phys. Rev. Lett.* **64**, 633 (1990).

[ABK90] Andersen L. H., Bolko J. and Kvistgaard P.: *Phys. Rev. Lett.* **64**, 729 (1990).

[APS92] Andersen L. H., Pan G. Y. and Schmidt H. T.: *J. Phys. B* **25**, 277 (1992).

[ASS 03] Artemyev A., Shabaev V. M., Sysak M. M., Yerokhin V. A., Beier T., Plunien G. and Soff G.: *Phys. Rev. A* **67**, 062506 (2003).

[BCA 84] Briand J. P., Charles P., Arianer J., Laurent H., Goldstein C., Dubau J. and Loulergue M.: *Phys. Rev. Lett.* **52**, 617 (1984).

[BCI 90] Briand J. P., Chevallier P., Indelicato P., Ziock K. P. and Dietrich D.: *Phys. Rev. Lett.* **65**, 2761 (1990).

[BFF 97] Biedermann C., Förster A., Fußmann G. and Radtke R.: *Phys. Scr. T* **73**, 360 (1997).

[BJO 04] Behar E., Jacobs V., Oreg J., Bar-Shalom A. and Haan S. L.: *Phys. Rev. A* **69**, 022704 (2004).

[BKM 03] Brandau C., Kozhuharov C., Müller A., Shi W., Schippers S., Bartsch T., Böhm S., Böhme C., Hoffknecht A., Knopp K., Grün N., Scheid W., Steih T., Bosch F., Franzke B., Mokler P. H., Nolden F., Stöhlker T. and Stachura Z.: *Phys. Rev. Lett.* **91**, 073202 (2003).

[BKR 90] Belkacem E. P., Kanter E. P., Rehm K. E., Bernstein E. M., Clark M. W., Ferguson S. M., Tanis J. A., Berkner K. H. and Schneider D.: *Phys. Rev. Lett.* **64**, 380 (1990).

[BLS59] Brown G. E., Langer J. S. and Schaefer G. W.: *Proc. Roy. Soc. A* **251**, 92 (1959).

[BMJ 93] Blundell S. A., Mohr P. J., Johnson W. R. and Sapirstein J.: *Phys. Rev. A* **48**, 2615 (1993).

[BMP 97] Beier T., Mohr P. J., Persson H., Plunien G., Greiner M. and Soff G.: *Phys. Lett. A* **236**, 329 (1997).

[Boh13] Bohr N.: *Philos. Mag.* **26**, 1 (1913).

[BOS 98] Beiersdorfer P., Osterheld A. L., Scofield J. H., Crespo López-Urrutia J. R. and Widmann K.: *Phys. Rev. Lett.* **80**, 3022 (1998).

[BP92] Badnell N. R. and Pindzola M. S.: *Phys. Rev. A* **45**, 2820 (1992).

[BRF02] Biedermann C., Radtke R. and Fournier K. B.: *Phys. Rev. E* **66**, 066404 (2002).

[Bri45] Brillouin L.: *Phys. Rev.* **67**, 260 (1945).

[BS57] Bethe H. A. and Salpeter E. E.: *Quantum Mechanics of One- and Two-Electron Systems.* Berlin : Springer (1957).

[Bur64] Burgess A.: *Astrophys. J.* **139**, 776 (1964).

[CAI 96] Currell F. J., Asada J., Ishii K., Minoh A., Motohashi K., Nakamura N., Nishizawa K., Ohtani S., Okazaki K., Sakurai M., Shiraishi H., Tsurubuchi S. and Watanabe H.: *J. Phys. Soc. Jpn.* **65**, 3186 (1996).

[CDM 99] Crespo López-Urrutia J. R., Dorn A., Moshammer R. and Ullrich J.: *Phys. Scr. T* **80**, 502 (1999).

[CG76] Cowan R. D. and Griffin D. C.: *J. Opt. Soc. Am.* **66**, 1010 (1976).

[Che86] Chen M. H.: *At. Data Nucl. Data Tables* **34**, 301 (1986).

[CMH 01] Campbell J. L., McDonald L., Hopman T. and Papp T.: *X-Ray Spectrom.* **30**, 230 (2001).

[Cow67] Cowan R. D.: *Phys. Rev.* **163**, 54 (1967).

[DDM 83] Dittner P. F., Datz S., Miller P. D., Moak C. D., Stelson P. H., Bottcher C., Dress W. B., Alton G. D., Neskovic N. and Fou C. M.: *Phys. Rev. Lett.* **51**, 31 (1983).

[DIA69] Donets E. D., Ilushchenko V. I. and Alpert V. A.: ICIS-1. Saclay, , 635 (1969).

[Dir28] Dirac P. A. M.: *Proc. Roy. Soc.* ***A*** **117**, 610 (1928).

[DKI 03] Deslattes R. D., Kessler E. G., Indelicato P., Billy L., Lindroth E. and Anton J.: *Rev. Mod. Phys.* **75**, 35 (2003).

[DMB 98] Delgago Martínez V., Mainardi R. T., Barrea R. A., Martínez Hidalgo C., Derosa P. A. and Marco Arboli M.: *X-Ray Spectrom.* **27**, 321 (1998).

[Don85] Donets E. D.: *Nuc. Instrum. Methods B* **9**, 522 (1985).

[DVD69] Drake G. W., Victor G. A. and Dalgrano A.: *Phys. Rev.* **180**, 25 (1969).

[Fan61] Fano U.: *Phys. Rev.* **124**, 1866 (1961).

[FBR 98] Fuchs T., Biedermann C., Radtke R., Behar E. and Doron R.: *Phys. Rev. A* **58**, 4518 (1998).

[FC65] Fano U. and Cooper J. W.: *Phys. Rev.* **137**, A1364 (1965).

[FRB 97] Fisher V. I., Ralchenko Y. V., Bernshtam V. A., Goldgirsh A., Maron Y., Vainshtein L. A., Bray I. and Golten H.: *Phys. Rev. A* **55**, 329 (1997).

[Fro72] Froese Fischer C.: *Comp. Phys. Commun.* **4**, 107 (1972).

[Fro77] Froese Fischer C.: *The Hartree-Fock Method for Atoms.* New York : Weley (1977).

[GAC 05] González Martínez A. J., Artemyev A., Crespo López-Urrutia J. R., Harman Z., Jentschura U. D., Keitel C. H., Scofield J., Tawara H., Tupitsyn I. and Ullrich J.: *to be published* (2005).

[GBB 90] Graham W. G., Berkner K. H., Bernstein E. M., Clark M. W., Feinberg B., McMahan M. A., Morgan T. J., Rathbun W., Schlachter A. S. and Tanis J. A.: *Phys. Rev. Lett.* **65**, 2773 (1990).

[GBS02] Gorczyca T. W., Badnell N. R. and Savin D. W.: *Phys. Rev. A* **65**, 062707 (2002).

[GCB 05] González Martínez A. J., Crespo López-Urrutia J. R., Braun J., Brenner G., Bruhns H., Lapierre A., Mironov V., Scofield J., Soria Orts R., Tawara H., Trinczek M. and Ullrich J.: *accepted in Phys. Rev. Lett.* (2005).

[GHB 00] Gwinner G., Hoffknecht A., Bartsch T., Beutelspacher M., Eklöw N., Glans P., Grieser M., Krohn S., Lindroth E., Müller A., Saghiri A. A., Schippers S., Schramm U., Schwalm D., Tokman M., Wissler G. and Wolf A.: *Phys. Rev. Lett.* **84**, 4822 (2000).

[Gil97] Gillaspy J. D.: *Phys. Scr. T* **71**, 99 (1997).

[Gil03] Gillaspy J.: *Trapping Highly Charged Ions: Fundamentals and Applications.* Huntington, New York : Nova Science Publishers, Inc. (2003).

[GR80] Gunnink R. and Ruther W. D.: Report UCRL52917, Lawrence Livermore National Laboratory. (1980).

[GSB 05] Gumberidze A., Stöhlker Th., Banaś D., Beckert K., Beller P., Beyer H.F., Bosch F., Hagmann S., Kozhuharov C., Liesen D., Nolden F., Ma X., Mokler P.H., Orsić-Muthig A., Steck M., Sierpowski D. and amd Y. Zou S. T.: *accepted to Phys. Rev. Lett.* (2005).

[Gun78] Gunnink R.: Report UCRL80297, Lawrence Livermore National Laboratory. (1978).

[Har05] Harman Z.: *Private communication* (2005).

[Her58] Herrmann G.: *J. Appl. Phys.* **29**, 127 (1958).

[HJ89] Haan S. L. and Jacobs V. L.: *Phys. Rev. A* **40**, 80 (1989).

[HJK05a] Harman Z., Jentschura U. D. and Keitel C. H.: *Internal report, Max-Planck-Institut für Kernphysik* (2005).

[HJK05b] Harman Z., Jentschura U. D. and Keitel C. H.: *to be published* (2005).

[Hum78] Humlicek J.: *J. Quant. Spectrosc. Radiat. Transfer* **21**, 309 (1978).

[IBL98] Indelicato P., Boucard S. and Lindroth E.: *Eur. Phys. J. D* **3**, 29 (1998).

[IS75] Ivanova E. P. and Safronova U. I.: *J. Phys. B* **8**, 1591 (1975).

[JCH87] Jacobs V. L., Cooper J. and Haan S. L.: *Phys. Rev. A* **36**, 1093 (1987).

[JPS84] Janev R. K., Presnyakov L. P. and Shevelko V. P.: *Physcis of Highly Charged Ions.* Berlin/Heidelberg/New York/Tokyo : Springer-Verlag (1984).

[JS86] Johnson W. R. and Sapirstein J.: *Phys. Rev. Lett.* **57**, 1126 (1986).

[KAB93] Krake G., Alber G. and Briggs J. S.: *J. Phys. B* **26**, L561 (1993).

[KBB 90] Kilgus G., Berger J., Blatt P., Grieser M., Habs D., Hochadel B., Jaeschke E., Krämer D., Neumann R., Neureither G., Ott W., Schwalm D., Steck M., Stokstad R., Szmola E., Wolf A., Schuch R., Müller A. and Wagner M.: *Phys. Rev. Lett.* **64**, 737 (1990).

[KBC 95] Knapp D. A., Beiersdorfer P., Chen M. H., Scofield J. H. and Schneider D.: *Phys. Rev. Lett.* **74**, 54 (1995).

[Kel66] Kelly H. P.: *Phys. Rev.* **144**, 39 (1966).

[KML 89] Knapp D. A., Marrs R. E., Levine M. A., Bennett C. L., Chen M. H., Henderson J. R., Scheneider M. B. and Scofield J. H.: *Phys. Rev. Lett.* **62**, 2104 (1989).

[KMS 93] Knapp D. A., Marrs R. E., Schneider M. B., Chen M. H. and Levine M. A.: *Phys. Rev. A* **47**, 2039 (1993).

[Kra23] Kramers H. A.: *Philos. Mag.* **46**, 836 (1923).

[Leo87] Leo W. R.: *Techniques for nuclear and particle physics experiments.* Berlin-Heidelberg : Springer-Verlag (1987).

[Lin95] Lindroth E.: *Nuc. Instrum. Methods B* **98**, 1 (1995).

[LMB 89] Levine M. A., Marrs R. E., Bardsley J. N., Beiersdorfer P., Bennett C. L., Chen M. H., Cowan T., Dietrich D., Henderson J. R., Knapp D. A., Osterheld A., Penetrante B. M., Schneider M. B. and Scofield J. H.: *Nucl. Instrum. Methods B* **43**, 431 (1989).

[LMH 88] Levine M. A., Marrs R. E., Henderson J. R., Knapp D. A. and Schneider M. B.: *Phys. Scr. T* **22**, 157 (1988).

[LPS 98] Lindgren I., Persson H., Salomonson S. and Sunnergren P.: *Phys. Lett. A* **58**, 1001 (1998).

[LR47] Lamb W. E. and Retherford R. C.: *Phys. Rev.* **72**, 339 (1947).

[LVS82] Litvin M., Vella M. and Sessler A.: *Nuc. Instrum. Methods* **198**, 189 (1982).

[MB42] Massey H. S. W. and Bates D. R.: *Rep. Prog. Phys.* **9**, 62 (1942).

[MEK94] Marrs R. E., Elliott S. R. and Knapp D. A.: *Phys. Rev. Lett.* **72**, 4082 (1994).

[MJ71] Mann J. B. and Johnson W. R.: *Phys. Rev. A* **4**, 41 (1971).

[MLK 88] Marrs R. E., Levine M. A., Knapp D. A. and Henderson J.: In: *Electronic and Atomic Collisions*. Elsevier, , 209 (1988).

[MNF 83] Mitchell J. B. A., Ng C. T., Forand J. L., Levac D.P., Mitchell R. E., Sen A., Miko D. B. and McGowan J. W.: *Phys. Rev. Lett.* **50**, 335 (1983).

[Moh73] Mohr P. J.: *Ann. Phys.* **88**, 26 (1973).

[MPS98] Mohr P., Plunien G. and Soff G.: *Phys. Rep.* **293**, 227 (1998).

[MS93] Mohr P. J. and Soff G.: *Phys. Rev. Lett.* **70**, 158 (1993).

[MS98] Mallampalli S. and Sapirstein J.: *Phys. Lett. A* **57**, 1548 (1998).

[MSW 91] Müller A., Schennach S., Wagner M., Haselbauer J., Uwira O., Spies W., Jennewein E., Becker R., Kleinod M., Pröbstel U., Angert N., Klabunde J., Mokler P. H., Spädtke P. and Wolf B.: *Phys. Scr. T* **37**, 62 (1991).

[MTW 03] Mironov V., Trinczek M., Werdich A., González Martínez A. J., Guo P., Zhang X., Braun J., Crespo López-Urrutia J. R. and Ullrich J.: *Nucl. Instr. Meth. B* **205**, 183 (2003).

[Mül95] Müller A.: *Nucl. Instrum. Methods B* **99**, 58 (1995).

[NIS04] *http://physics.nist.gov* (2004).

[NM95] Nerlo-Pomorska B. and Mach B.: *At. Data Nucl. Data Tables* **60**, 287 (1995).

[Nuc05] *http://nucleardata.nuclear.lu.se* (2005).

[OSL 05] Orlov D. A., Sprenger F., Lestinsky M., Weigel U., Terekhov A. S., Schwalm D. and Wolf A.: In: *Sixth International Conference on Dissociative Recombination*. Institute of Physics Publishing, , 290 (2005).

[PBD 91] Penetrante B. M., Bardsley J. N., DeWitt D., Clark M. and Schneider D.: *Phys. Rev. A* **43**, 4861 (1991).

[PBG92] Pindzola M. S., Badnell N. R. and Griffin D. C.: *Phys. Rev. A* **46**, 5725 (1992).

[Roh05] Rohr A.: *Experimentelle Untersuchung von nicht Maxwellischen Elektronendirecktеverteilungen in Hochtemperaturplasmen*, Ruprecht-Karls-Universität Heidelberg, (2005).

[Rut11] Rutherford E.: *Phil. Mag.* **21**, 699 (1911).

[Saf02] Safronova U. I.: *Private communication* (2002).

[SAY00] Shabaev V. M., Artemyev A. N. and Yerokhin V. A.: *Phys. Scr. T* **86**, 7 (2000).

[SBB 91] Schweppe J., Belkacem A., Blumentfeld L., Claytor N., Feinberg B., Gould H., Kostroun V. E., Levy L., Misawa S., Mowat J. R. and Prior M. H.: *Phys. Rev. Lett.* **66**, 1434 (1991).

[Sch26a] Schrödinger E.: *Ann. d. Physik* **79**, 361 (1926).

[Sch26b] Schrödinger E.: *Ann. d. Physik* **81**, 109 (1926).

[Sch00] Scholz M.: *Nucl. Instr. Meth. B* **161**, 76 (2000).

[Sco89] Scofield J. H.: *Phys. Rev. A* **40**, 3054 (1989).

[Sco03] Scofield J. H.: *Private communication* (2003).

[SDK 69] Schäffer H. W., Dunford R. W., Kanter E. P., Cheng S., Curtis L. J., Livingston A. E. and Mokler P. H.: *Phys. Rev. A* **59**, 245 (1969).

[Sil94] Silver J. D.: *Rev. Sci. Inst.* **65**, 1072 (1994).

[SKE 97] Stöhlker T., Krämer A., Elliot S. R., Marrs R. E. and Scofield J. H.: *Phys. Rev. A* **56**, 2819 (1997).

[SKM 02] Schippers S., Kieslich S., Müller A., Gwinner G., Schnell M., Wolf A., Covington A., Bannister M. E. and Zhao L. B.: *Phys. Rev. A* **65**, 042723 (2002).

[SMB 00] Stöhlker T., Mokler P. H., Bosch F., Dunford R. W., Klepper O., Kozhuharov C., Ludziejewski T., Nolden F., Reich H., Rymuza P, Stachura Z., Steck M., Swiat P. and Warczak A.: *Phys. Rev. Lett.* **85**, 3109 (2000).

[SMG 92] Stöhlker T., Mokler P., Geissel H., Moshammer R., Rymuza P., Berstein E. M., Cocke C. L., Kozhuharov C., Muzenberg G., Nickel F., Scheidenberger C., Stachura Z., Ullrich J. and Warczak A.: *Phys. Lett. A* **168**, 285 (1992).

[SPK73] Salem S. I., Panossian S. L. and Krause R. A.: *At. Data Nucl. Data Tables* **14**, 91 (1973).

[ST98] Shevelko V. P. and Tawara H.: *Atomic Multielectron Processes.* Berlin Heidelberg New York : Springer (1998).

[Sto30] Stobbe M.: *Ann. Phys., Lpz.* **7**, 661 (1930).

[SU26] Sommerfeld A. and Unsöld A.: *Zeits. f. Physik* **36**, 259 (1926).

[SU79] Safronova U. I. and Urnov A. M.: *J. Phys. B* **12**, 3171 (1979).

[Tup04] Tupitsyn I.: *Private communication* (2004).

[UMD 03] Ullrich J., Moshammer R., Dorn A., Dörner R., Schmidt L.Ph.H. and Schmidt-Böcking H.: Recoil-Ion and Electron Momentum Spectroscopy: Reaction-Microscopes. *Rep. Prog. Phys.* **66**, 1463 (2003).

[Uni05] University Stockholm: *Private communication* (2005).

[WAC 97] Wanatabe H., Asada J., Currell F. J., Fukami T., Hirayama T., Motohashi K., Nakamura N., Nojikawa E., Ohtani S., Okazaki K., Sakurai M., Shimizu H., Tada N. and Tsurubuchi S.: *J. Phys. Soc. Jpn.* **66**, 3795 (1997).

[WBD95] Widmann K., Beiersdorfer P. and Decaux V.: *Nucl. Instr. Meth. B* **98**, 45 (1995).

[WE47] Wigner E. P. and Eisenbud L.: *Phys. Rev.* **72**, 29 (1947).

[Wid98] Widmann K.: *High resolution spectroscopic diagnostics of very high-temperature plasmas in the hard x-ray regime*, Technische Universität Graz, (1998).

[Win03] Winter T. G.: *Am. J. Phys.* **71**, 783 (2003).

[WK56] Wichmann E. H. and Kroll N. M.: *Phys. Rev.* **101**, 843 (1956).

[YAB 03] Yerokhin V. A., Artemyev A. N., Beier T., Goidenko I. A., Labzowsky L. N., Nefiodov A. V., Plunien G., Shabaev V. M. and Soff G.: *X-Ray Spectrom.* **32**, 83 (2003).

[ZCG 04] Zhang X., Crespo López-Urrutia J. R., Guo P., Mironov V., Shi X., González Martínez A. J., Tawara H. and Ullrich J.: *J. Phys. B* **37**, 2277 (2004).

[ZCU03] Zou Y., Crespo López-Urrutia J. R. and Ullrich J.: *Phys. Rev. A* **67**, 042703 (2003).

[ZGS97] Zimmermann M., Grün N. and Scheid W.: *J. Phys. B* **30**, 5259 (1997).

Acknowledgments

The help, enthusiasm, companionship and other collective as well as personal abilities of those surrounding me along this time have allowed to perform this work. From these lines, I dedicate this thesis to all of them. In this sense, the list of acknowledgments is undoubtedly longer than what is written below.

I wish to thank Prof. Joachim Ullrich who, in particular, offered his great help at the beginning overcoming some administrative troubles taking place in the Physics Dekanat, thus, making possible to enjoy this group.

Going deeply, the EBIT team. It is, simply, a joined group commanded by José Ramón Crespo Lopez-Urrutia, who besides such an "entertainment" task, manages to teach (me) on our own Spanish culture as well as organize nice barbecues/dinners in company of his pleasant family.

In my first steps as a so-called experimentalist I have to thank enormously Panlin Guo and Xuemei Zhang who had the patience to share their whole knowledge in a "tirelessly" way. In the later times, I wish to thank the dubbed "Post-Prof." Hiro Tawara, who offers his encouraged help in every single experiment, test, posters, papers etc. In addition, his carefully analysis and search for mistakes in this thesis, finding errors, if small, even behind the figures, have made possible to fulfill this work. Thanks are also given to Zoltan Harman, who has been correcting as well as performing very fast and fresh calculations which were added to the present work in the last minutes.

The EBIT team has been growing smoothly becoming rather numerous. I strongly appreciate the help of those who have come and gone shortly. Especially thanks are given to the three B*s*; Johannes Braun, Günter Brenner and Hjalmar Bruhns, just being on board all this time. Short but intense was the friendship with Alain Lapierre, opened to any question anytime, even about how to cook Sushi.

Experimental data would be nonsense if it is not, at least in first approximation, compared with theoretical predictions. Thus, I am grateful for the theoretical support of A. Artemyev, J. H. Scofield and I. Tupitsyn.

> *A theory is something nobody believes, except the person who made it. An experiment is something everybody believes, except the person who made it.*
> ***A. Einstein***

Die Durchführung dieser experimentellen Arbeit wäre außerdem nicht ohne die Unterstützung und den täglichen Einsatz des technischen Personals möglich gewesen.

An dieser Stelle möchte ich mich bei Karl Bechberger und Norbert Müller für die akkurate Arbeit im EBIT Labor und bei Thomas Busch für den Aufbau und die Wartung unserer "Babies" (Spannungsteiler) bedanken.

Even reducing my writing space I dedicate some more words to another countless help in everything; from the quasi-complex (to me) GOOSY stuff to going down a hill with a pair of skis without breaking anything, thanks Daniel Fischer. In fact, I am still wondering why by typing both exactly the same commands in those programs, only they worked for him. Directly connected is unforgivable not to name Vitor Luiz Bastos de Jesus, for those times we have laughed all together.

The experience I have had along these years here has culminated the young dream of making "physics". Many children like to construct small devices at home, dismount toys or mix whatever liquids they find in a kitchen, I also did it. They are the next generation. For most of them, their dreams still to be defined in some direction, Why not on Physics ? Although the unavoidable competition in all types of research keeps a dynamic rate and fruitful results, in most of the cases, vanishes the beauty of this job.

I would also like to thank the reader, I hope you got to this last page being reading the whole stuff.

> *A hydrogen atom lost its electron and went to the police station to file a missing electron report. He was questioned by the police: "Haven't you just misplaced it somewhere? Are you sure that your electron is really lost?".*
> *"I'm positive." replied the atom.*

Los últimos siempre serán los primeros. El apoyo constante de Rosario, mi perla, ha sido y es incontable, e incluso incansable. Desde el día que cogimos las maletas, sólo a un mes de Fallas, y nos aventuramos en esta cruzada con ningún conocimiento de alemán y para que contar de nuestro spanglish, ha sido "la alegría de la casa". Sin ser una persona de grandes agradecimientos, aquí quedan los míos hacia ti, como diría mi madre, por aguantarme.

No podría acabar de agradecer gente si no lo hiciese a mis padres. A mi madre por su fascinación y "comprensión" de tener a su hijito en Alemania. A mi padre por la silenciosa confianza y como no, la clasificación casi semanal de la liga. A mi hermana Marivi por compartir siempre sus dudas conmigo.